

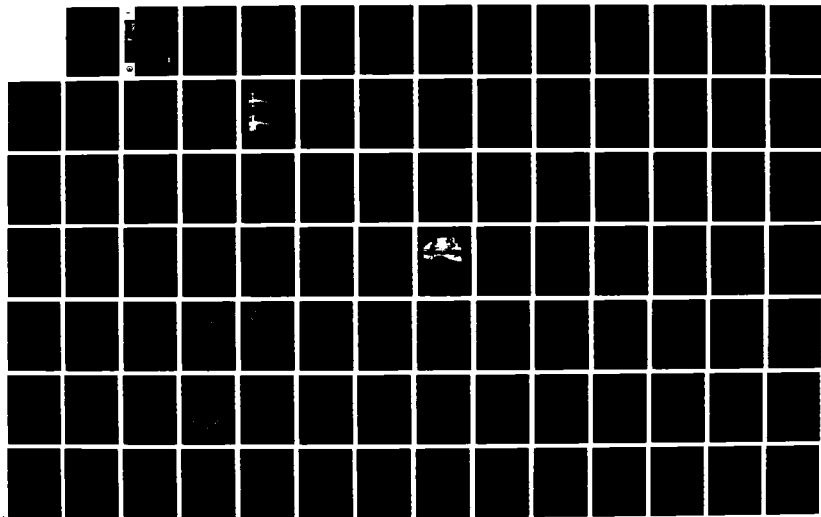
AD-A194 389

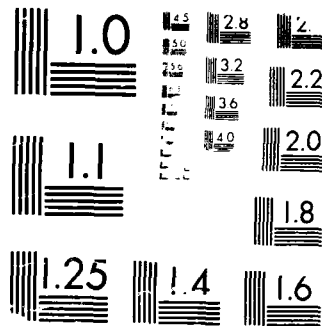
KINGS BAY COASTAL PROCESSES NUMERICAL MODEL(U) COASTAL 1/2  
ENGINEERING RESEARCH CENTER VICKSBURG MS  
S R VEHLAKONDA ET AL. APR 88 CERC-TR-88-3

UNCLASSIFIED

F/O 13/2

NL





MICROCOPY RESOLUTION TEST CHART  
100-2819-10

DTIC FILE COPY

4

TECHNICAL REPORT CER-88-3

# KINGS BAY COASTAL PROCESSES NUMERICAL MODEL

by

S. Rao Vemulakonda, Norman W. Scheffner  
Jeffrey A. Earickson, Lucia W. Chou

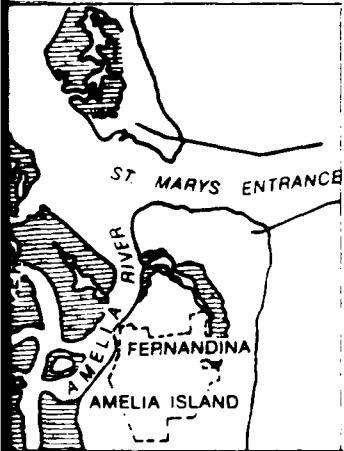
Coastal Engineering Research Center

DEPARTMENT OF THE ARMY  
Waterways Experiment Station, Corps of Engineers  
PO Box 631, Vicksburg, Mississippi 39180-0631



US Army Corps  
of Engineers

AD-A194 389



April 1988  
Final Report

Approved For Public Release; Distribution Unlimited

DTIC  
ELECTE  
MAY 18 1988  
S D  
CA  
E



Prepared for Officer In Charge of Construction  
TRIDENT  
DEPARTMENT OF THE NAVY  
Naval Facilities Engineering Command  
St. Marys, Georgia 31558-0768

073

Unclassified  
SECURITY CLASSIFICATION OF THIS PAGE

REPORT DOCUMENTATION PAGE				Form Approved OMB No 0704 0188 Exp Date Jun 30 1986	
1a REPORT SECURITY CLASSIFICATION <b>Unclassified</b>		1b RESTRICTIVE MARKINGS			
2a SECURITY CLASSIFICATION AUTHORITY		3 DISTRIBUTION/AVAILABILITY OF REPORT <b>Approved for public release; distribution unlimited.</b>			
2b DECLASSIFICATION/DOWNGRADING SCHEDULE					
4 PERFORMING ORGANIZATION REPORT NUMBER(S) <b>Technical Report CERC-88-3</b>		5 MONITORING ORGANIZATION REPORT NUMBER(S)			
6a NAME OF PERFORMING ORGANIZATION <b>USAEWES, Coastal Engineering Research Center</b>		6b OFFICE SYMBOL <i>(if applicable)</i>	7a NAME OF MONITORING ORGANIZATION		
6c ADDRESS (City, State, and ZIP Code) <b>Box 631 Vicksburg, MS 39180-0631</b>		7b ADDRESS (City, State, and ZIP Code)			
8a NAME OF FUNDING/SPONSORING ORGANIZATION <b>See reverse.</b>	8b OFFICE SYMBOL <i>(if applicable)</i>	9 PROCUREMENT INSTRUMENT IDENTIFICATION NUMBER			
8c ADDRESS (City, State, and ZIP Code) <b>St. Marys, GA 31558-0768</b>		10 SOURCE OF FUNDING NUMBERS			
		PROGRAM ELEMENT NO	PROJECT NO	TASK NO	WORK UNIT ACCESSION NO
11 TITLE (Include Security Classification) <b>Kings Bay Coastal Processes Numerical Model</b>					
12 PERSONAL AUTHOR(S) <b>Vemulakonda, S. Rao; Scheffner, Norman W.; Earickson, Jeffrey A.; Chou, Lucia W.</b>					
13a TYPE OF REPORT <b>Final report</b>		13b TIME COVERED FROM <b>Oct 83</b> TO <b>Dec 85</b>	14 DATE OF REPORT (Year, Month, Day) <b>April 1988</b>		15 PAGE COUNT <b>120</b>
16 SUPPLEMENTARY NOTATION <b>Available from National Technical Information Service, 5285 Port Royal Road, Springfield, VA 22161.</b>					
17 COSATI CODES			18 SUBJECT TERMS (Continue on reverse if necessary and identify by block number)		
FIELD	GROUP	SUB-GROUP			
			<b>See reverse.</b>		
19 ABSTRACT (Continue on reverse if necessary and identify by block number) <b>St. Marys Inlet is the main ocean entrance to the Naval Submarine Base, Kings Bay, Georgia. In order to accommodate Trident submarines at the base, it became necessary to modify the exterior navigation channel. This report describes details of a numerical modeling effort performed to study the effects of channel modifications on coastal processes near the inlet, especially channel shoaling rates.</b>  <b>A system of numerical models, which included models for tides, waves, wave-induced currents, and noncohesive sediment (sand) transport, was used in the study. The system, together with two computational grids, was called Model B. It was used to study existing (base) as well as planned conditions. Plan 1 is to widen the navigation channel by 100 ft, deepen the channel to -49 ft mlw (46-ft project depth plus 3-ft advance maintenance), and extend the channel on the ocean side with a 20-deg bend to the south. Model B considered the simultaneous sand-tightening of a 1,000-ft segment of the south jetty.</b>  <b>(Continued)</b>					
20 DISTRIBUTION/AVAILABILITY OF ABSTRACT <input checked="" type="checkbox"/> UNCLASSIFIED UNLIMITED <input type="checkbox"/> SAME AS RPT <input type="checkbox"/> DTIC USERS			21 ABSTRACT SECURITY CLASSIFICATION <b>Unclassified</b>		
22a NAME OF RESPONSIBLE INDIVIDUAL		22b TELEPHONE (Include Area Code)		22c OFFICE SYMBOL	

8a. NAME OF FUNDING/SPONSORING ORGANIZATION (Continued).

DEPARTMENT OF THE NAVY  
Naval Facilities Engineering Command

18. SUBJECT TERMS (Continued).

Advance maintenance	Navigation channels	St. Marys Inlet
Coastal processes	Numerical models	Tides
Hydrodynamics	Sediment transport	Waves
Inlets	Shoaling rates	Wave-induced currents
Kings Bay (Georgia)		

19. ABSTRACT (Continued).

The tidal model was verified using field data taken on 10 November 1982. The average year's wave climate for the study area was obtained from 20-year hindcast data. The dataset included normal storms (but not hurricanes and tropical storms). It was used in running the wave and wave-induced current models. The sediment transport model determined noncohesive sediment (sand) transport in the study area under the action of tides, waves and wave-induced currents. It considered a mean tide and the average year's wave climate. It was verified by comparing computed erosion/deposition rates in the navigation channel with those obtained from field surveys taken during 1980-81. There was good agreement both with respect to trends and magnitudes.

While all four models were run for base conditions, only the tidal model and the sediment transport model were run for Plan 1 conditions to meet the urgent need for model results. Based on the model results and available information, recommendations on advance maintenance dredging are made for various reaches of the navigation channel.

PREFACE

The study described herein was authorized by the Officer In Charge of Construction (OICC), TRIDENT, Naval Facilities Engineering Command, Department of the Navy, St. Marys, Georgia. All elements of the investigation were conducted at the US Army Engineer Waterways Experiment Station (CEWES) from October 1983 to December 1985. The Coastal Engineering Research Center (CERC) conducted this study as part of a larger CEWES modeling effort for Kings Bay coordinated by the Hydraulics Laboratory (HL), CEWES, with Messrs. William H. McAnally, Jr., and Mitch A. Granat, HL, serving as overall CEWES Project Managers. Contract monitoring for the study was provided by Messrs. George Carpenter, John Randall, and Brian Smith, OICC.

This report was prepared by Dr. S. Rao Vemulakonda, Project Manager, CERC. The study was performed by Drs. Vemulakonda and Norman W. Scheffner, Mr. Jeffrey A. Earickson, and Mrs. Lucia W. Chou, Coastal Processes Branch (CR-P), CERC. Work was done under direct supervision of Mr. H. Lee Butler, Chief, Research Division, and under general supervision of Dr. James R. Houston and Mr. Charles C. Calhoun, Jr., Chief and Assistant Chief, CERC, respectively.

The advice of Dr. Houston and Mr. Butler and the assistance of Mr. Bruce A. Ebersole, CR-P, and Ms. Mary A. Cialone (formerly of CERC) are acknowledged. Hindcast wave information was provided by Dr. Robert E. Jensen, Coastal Oceanography Branch, CERC. This report was edited by Ms. Shirley A. J. Hanshaw, Information Products Division, Information Technology Laboratory, CEWES.

During report publication COL Dwayne G. Lee, CE, was Commander and Director of CEWES. Dr. Robert W. Whalin was Technical Director.



<b>Accession For</b>	
NTIS GRA&I	<input checked="" type="checkbox"/>
DTIC TAB	<input type="checkbox"/>
Unannounced	<input type="checkbox"/>
Justification _____	
By _____	
Distribution/ _____	
<b>Availability Codes</b>	
Dist	Avail and/or Special
A-1	

## EXECUTIVE SUMMARY

St. Marys Inlet is a large jettied tidal inlet through the barrier island system of Georgia and Florida. It is located approximately 30 miles north of Jacksonville, Florida. The inlet is the main ocean entrance to the US Navy Submarine Base at Kings Bay, Georgia. As a part of upgrading the base to accommodate Trident submarines, it became necessary to improve the base facilities and modify the navigation channels to the interior and exterior of the inlet.

In 1983 the Officer In Charge of Construction (OICC), Trident, requested the US Army Engineer Waterways Experiment Station (CEWES) to determine, by modeling, the impact of these modifications on hydrodynamics and sedimentation. As a result, two studies were undertaken simultaneously. The first, performed by the Hydraulics Laboratory of CEWES, used a hybrid modeling approach to determine the impact of the interior modifications. A report by Granat, et al. (in preparation) describes the results of the investigation. The second study was a numerical modeling effort by the Coastal Engineering Research Center (CERC) of CEWES to determine the effect of modifications of the exterior channels on coastal processes near the inlet, especially channel shoaling rates. The report herein describes details of this second study.

To accomplish the objectives of the second study, CERC employed a system of numerical models called Coastal and Inlet Processes (CIP) Numerical Modeling System. The system included four separate numerical models for tides, waves, wave-induced currents, and noncohesive sediment (sand) transport. The system together with two computational grids--one for existing (base) conditions and the other for plan conditions--was called Model B in contrast to Model A, the hybrid model for the interior.

To substantiate the validity of the modeling approach and to improve accuracy of predicted results, Model B was first verified with available field data on tides and sediment transport. The tidal model was verified by using field data on tidal elevations and currents taken on 10 November 1982. Good verification was obtained by matching model results with observed tidal currents over one tidal cycle. The wave climate for an average year in 60-ft depth mean low water (mlw) at the project site was obtained from the CEWES Wave Information Study based on a 20-year hindcast. This information was discretized into 79 different monochromatic waves. These waves were propagated

to the shore using the wave model and wave conditions were determined everywhere over the study area. The wave-induced current model used the wave information to determine wave-induced currents over the study area. The sediment transport model used the results of the other three models to determine sediment transport. It was verified by comparing its predictions on navigation channel shoaling rates with shoaling rates computed from channel surveys taken during the period November 1980 to December 1981. There was good agreement with respect to both trends and magnitudes.

Model B was next used to determine base conditions corresponding to trapezoidal entrance and offshore channels with a bottom width of 400 ft, a project depth of 40 ft mlw and side slopes of 4H:1V. The sediment transport model results were obtained in terms of channel shoaling rates (ft/year) along the channel. The results were similar to those obtained during verification. In both cases, there was deposition outside the jetty tips. It changed to erosion inside the jetty tips because of circulation due to wave-induced currents. The heaviest deposition rates were predicted near the jetty tips. This is the area where the channel cuts through the offshore bar and where serious shoaling problems were encountered in the field for base conditions. On the basis of the numerical results, the yearly channel shoaling volume between sta -80+00 and sta 325+00 was predicted to be 475,000 cu yd/year. This value was comparable to within  $\pm 25$  percent of the yearly maintenance dredging volumes recorded by the US Army Engineer District, Jacksonville.

Model B tested only one plan condition which was called Plan 1. The plan was to (a) widen the navigation channel to 500 ft, with the widening taking place on the north side of the present entrance and offshore channels; (b) extend the channel on the ocean side, with the extension being at an angle of 20 deg south of the present channel center line at sta -97+76 approximately; and (c) deepen the channel to -49 ft mlw (46-ft project depth plus 3-ft advance maintenance). The channel was to have a trapezoidal cross section with side slopes of 3H:1V. At the request of OICC, TRIDENT, it was assumed during testing that the landward 1,000 ft of the south jetty would be made sand tight simultaneously.

In view of the urgent needs expressed by OICC for Plan 1 results from Model B for design of entrance and offshore channels, the wave and wave-induced current models were not rerun for Plan 1 as originally planned. Only the tidal and sediment transport models were rerun. The results of the tide

model showed the effects of Plan 1 to be mainly local and caused by sand-tightening of the south jetty. Tidal velocities at the end of the jetties and at Tide Gage 1 near the south jetty increased by approximately 10 percent. There were no significant changes in velocities at the throat of the inlet. The extension of the navigation channel at the seaward end produced almost no effect upon the tidal current patterns.

The results of the sediment transport model indicated an increase in both deposition rates and erosion rates from base to Plan 1 for the channel reach between sta -97+76 to sta 325+00. Model results for the reach between sta 325+00 and sta 399+74 for base and Plan 1 were suspect since quantitative field information on sedimentation was not available for this reach, the bathymetry used in Model B was not the latest, and the grain size of the sediment observed in this reach was much larger than that of the sediment everywhere else in the study area. For the channel reach between sta -80+00 and sta 325+00, the shoaling volume for Plan 1 was estimated from Model B results to be approximately 788,000 cu yd/year or an increase of approximately 66 percent from base. Finally, based on Model B results for Plan 1 and all other available information, recommendations on advance maintenance dredging were made for various reaches of the channel for use in channel design. Based on modeling limitations, the accuracy of Model B sediment transport results is estimated to be within  $\pm 25$  percent.

## CONTENTS

	<u>Page</u>
PREFACE . . . . .	1
EXECUTIVE SUMMARY . . . . .	2
CONVERSION FACTORS, NON-SI TO SI (METRIC)	
UNITS OF MEASUREMENT . . . . .	6
PART I:    INTRODUCTION . . . . .	7
Background . . . . .	7
Purpose . . . . .	7
PART II:    THE CIP NUMERICAL MODELING SYSTEM . . . . .	10
Numerical Modeling . . . . .	10
Computational Grids . . . . .	11
The Tidal Simulation Model, WIFM . . . . .	15
The Wave Model, RCPWAVE . . . . .	21
The Wave-Induced Current Model, CURRENT . . . . .	31
The Sediment Transport Model . . . . .	35
PART III:    VERIFICATION AND BASE CONDITION TESTS . . . . .	44
Tides . . . . .	44
Waves and Wave-Induced Currents . . . . .	50
Sediment Transport . . . . .	59
PART IV:    PLAN CONDITION TESTS . . . . .	68
Plan 1 . . . . .	68
Computational Grid . . . . .	68
Tides . . . . .	70
Sediment Transport . . . . .	71
PART V:    MODELING LIMITATIONS . . . . .	74
PART VI:    RECOMMENDATIONS . . . . .	77
Advance Maintenance Dredging . . . . .	77
Future Testing . . . . .	79
PART VII:    SUMMARY AND CONCLUSIONS . . . . .	80
REFERENCES . . . . .	82
BIBLIOGRAPHY . . . . .	85
TABLES 1-5	
PLATES 1-23	
APPENDIX A:    NOTATION . . . . .	A1
APPENDIX B:    ABBREVIATIONS AND ACRONYMS . . . . .	B1

CONVERSION FACTORS, NON-SI TO SI (METRIC)  
UNITS OF MEASUREMENT

Non-SI units of measurement used in this report can be converted to SI (metric) units as follows:

<u>Multiply</u>	<u>By</u>	<u>To Obtain</u>
cubic feet per second per foot	0.0929	cubic metres per second per metre
cubic yards per year	0.7646	cubic metres per year
feet	0.3048	metres
inches	0.0254	metres
miles (US nautical)	1,852	metres
miles (US statute)	1,609	metres
pounds (force) per foot	14.5932	newtons per metre
pounds per second	0.4536	kilograms per second
pounds (force) per square foot	47.88	pascals
slugs per cubic foot	515.4	kilograms per cubic metre

# KINGS BAY COASTAL PROCESSES NUMERICAL MODEL

## PART I: INTRODUCTION

### Background

1. St. Marys Inlet is a large jettied tidal inlet through the barrier island system of Georgia and Florida. It is the main entrance to Kings Bay Naval Submarine Base located at Kings Bay, Georgia. The inlet is located approximately 30 miles\* north of Jacksonville, Florida (Figure 1). The Georgia-Florida state line runs through the inlet. To the north of the inlet is Cumberland Island administered by the National Park Service, and to the south is Amelia Island. Fort Clinch State Park surrounding historic Fort Clinch is located on Amelia Island.

2. At present, Kings Bay is home to Poseidon-class submarines. The present entrance and offshore channels are trapezoidal in cross section with a bottom width of 400 ft, a project depth of 40 ft mean low water (mlw\*\*), and side slopes of 4H:1V. As a part of the upgrading of the submarine base to receive the larger Trident-class submarines, it became necessary to widen and deepen both the interior and exterior navigation channels. Simultaneously, it is proposed to sand-tighten a 1,500-ft segment of the south jetty. This study is mainly concerned with the exterior (entrance and offshore) channels. Hereafter the term "entrance channel" will be used to refer to the part of the exterior navigation channel between the jetties, and the term "offshore channel" will be used to denote the part of the navigation channel offshore of jetty tips. A companion study (Granat, et al., in preparation) considers the interior channels.

### Purpose

3. The purpose of this study is to determine the effect of the project on coastal processes near St. Marys Inlet. The processes studied include

---

\* A table of factors for converting non-SI to SI (metric) units is presented on page 6.

\*\* Abbreviations and acronyms are listed in Appendix B.

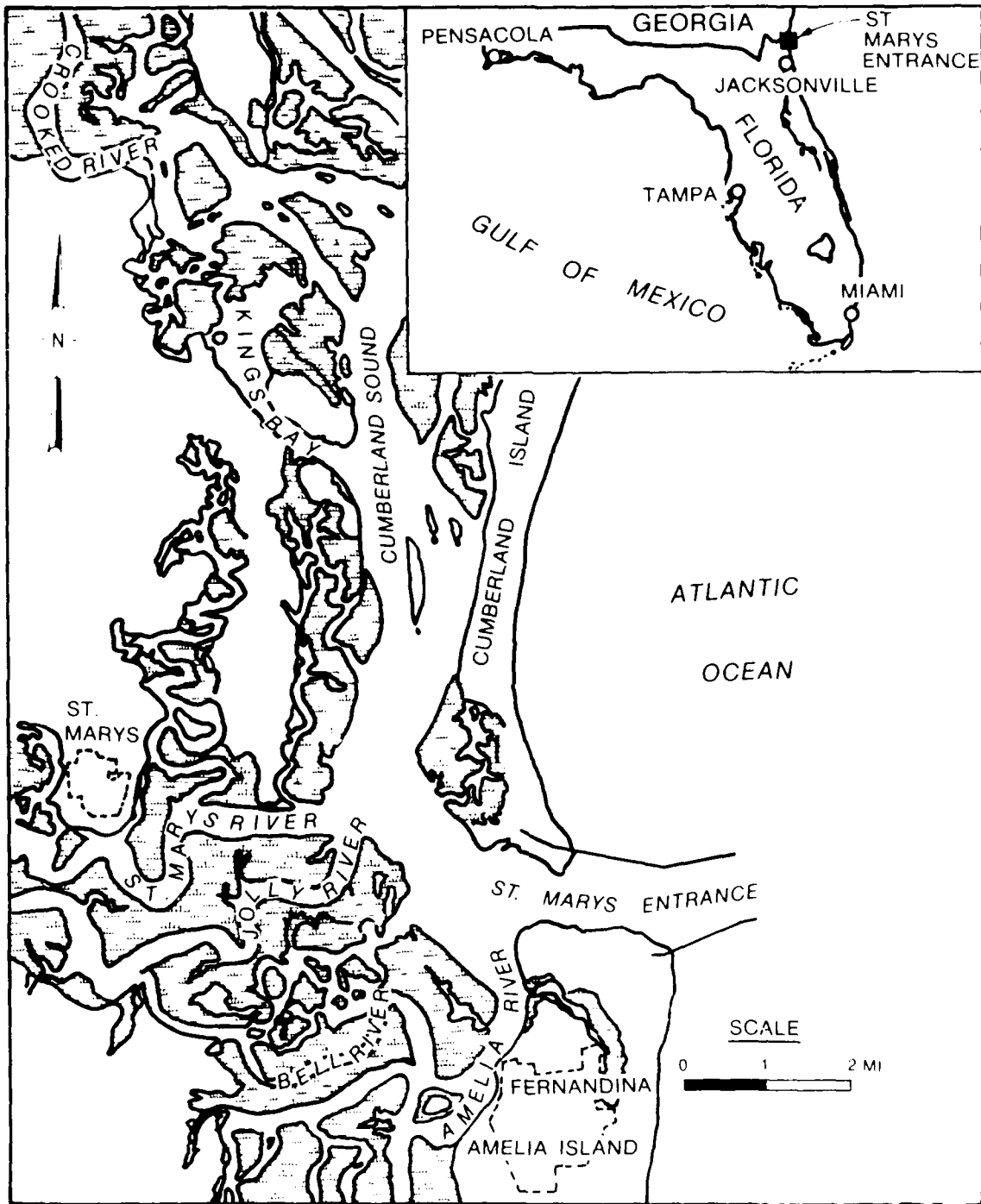


Figure 1. Location map

tides, waves, wave-induced currents, and sediment transport. Of special interest is the determination of shoaling rates in the navigation channel for existing (base) and plan conditions. Based on these shoaling rates, recommendations will be made to the project channel designers on the required yearly advance maintenance dredging for various reaches of the channel. To accomplish the objectives of the study, a system of numerical models called Coastal and Inlet Processes (CIP) Numerical Modeling System, which includes separate numerical models for the coastal processes mentioned above, will be employed. The system will take into account the effect of the two jetties on St. Marys Inlet. Models of the system will be calibrated and verified with available field data as far as possible and used to study existing conditions as well as planned conditions to determine the effect of the project on coastal processes.

## PART II: THE CIP NUMERICAL MODELING SYSTEM

### Numerical Modeling

4. Before details of the CIP modeling system are presented, a brief introduction to certain aspects of numerical models is in order. Generally, the physical variables of practical interest such as surface elevation, velocity, wave height, and sediment transport rate vary continuously in space and time. On the basis of the physics of the particular process, the variables are described by differential equations. In numerical modeling, the differential equations are replaced by difference equations involving finite differences in space and time. Thus, a numerical model considers values of the variables at discrete points in space and time and solves for the values of the variables by numerical techniques.

5. Numerical models are classified on the basis of variation of the dependent variables in space and time. If the dependent variable is a function only of one coordinate, then we have a one-dimensional model. For example, the average velocity in a river cross section may be a function only of distance along the river, and we can describe the flow using a one-dimensional model. If the dependent variable is a function of two coordinates, then we have a two-dimensional model. For instance, tidal elevations and currents in a shallow bay may be a function only of the two horizontal coordinates, and the tidal hydrodynamics can be described by a vertically averaged two-dimensional model. If the dependent variable is independent of time, a steady model is applicable; whereas if the variable varies with time, an unsteady model is needed.

6. It should be recognized that numerical models are only as good as the physics that goes into them and are in general approximations to physical reality. In recent years, numerical models have become standard tools to answer questions connected with engineering projects and have replaced traditional physical hydraulic models for studies involving tidal hydraulics, wave transformation, etc. They are the only feasible tools available for analyzing certain phenomena such as sediment transport under the combined action of tides and waves, wind-generated flows, etc. They have the following advantage. Once a numerical model has been calibrated and verified for a given project area for a given set of conditions, it can predict, within a

reasonable degree of reliability, the physical processes under a different set of conditions, provided the latter set is not radically different from the first. Thus the model is usually calibrated and verified for previous or existing conditions and used to predict future plan conditions.

7. In the study described herein, the coastal processes for St. Marys Inlet and the surrounding area of the Atlantic Ocean were modeled using the CIP numerical modeling system on two computational grids. The system includes the US Army Engineer Waterways Experiment Station (CEWES) Implicit Flooding Model (WIFM) for tides, the Regional Coastal Processes Wave Propagation Model (RCPWAVE) for waves, the model CURRENT for wave-induced currents, and a sediment transport model for transport of noncohesive sediments due to the combined action of tides, waves, and wave-induced currents. All four models generally used the same computational grid for a given set of conditions (base or plan). The following paragraphs highlight the important features of the computational grids and the four computer models used in this study. For convenience the numerical modeling system, together with the computational grids, was referred to as Model B in contrast to Model A, a hybrid model used for studying the region interior to the inlet.

#### Computational Grids

8. The models described in this report use the finite difference method for computations. In order to cover a large region but still maintain high resolution in desired areas, the models use a smoothly varying grid that allows cells to be small in certain areas (e.g., surf zone or inlet) and large in others (e.g., ocean or sound). A piecewise reversible transformation (analogous to that used by Wanstrath (1977)) is used independently in the x- and y-directions to map the variable grid into a uniform grid used in the computational space (Figure 2). The transformation has the following form:

$$x = a_p + b_p \alpha_1^c \quad (1)$$

$$y = a_q + b_q \alpha_2^c \quad (2)$$

where  $a_p$ ,  $b_p$ ,  $c_p$ ,  $a_q$ ,  $b_q$ , and  $c_q^*$  are arbitrary constants for regions  $p$  and  $q$  in the  $x$ - and  $y$ -directions, respectively, and  $\alpha_1$  and  $\alpha_2$  are coordinates in the computational space. This transformation allows all derivatives to be centered in the computational space. Many stability problems commonly occurring in variable grid schemes are eliminated when using this transformation since the grid in real space varies smoothly and the coordinates and their first derivatives are continuous at the boundaries between regions.

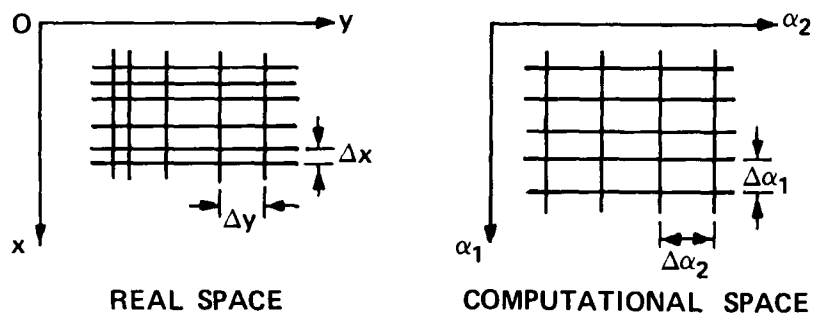


Figure 2. An example of variable grid

9. The partial differential equations governing the different processes are solved by finite difference integration on a grid of spatial points. A right-handed coordinate system is used with the  $x$ -coordinate increasing in the offshore direction and the  $y$ -coordinate increasing along the shoreline with the ocean to the right. The partial derivative of an arbitrary variable  $s$  in region  $p$  is

$$\frac{\partial s}{\partial x} = \frac{1}{\mu_x} \frac{\partial s}{\partial \alpha_1} \quad (3)$$

where

$$\mu_x = \frac{\partial x}{\partial \alpha_1} = b_p c_p \alpha_1^{c_p - 1} \quad (4)$$

\* For convenience, symbols and abbreviations are listed in the Notation (Appendix A).

Similarly

$$\frac{\partial s}{\partial y} = \frac{1}{\mu_y} \frac{\partial s}{\partial \alpha_2} \quad (5)$$

where

$$\mu_y = \frac{\partial y}{\partial \alpha_2} = b_q c_q \alpha_2^{c_q - 1} \quad (6)$$

If the grid in the x-, y-coordinate system is to have constant grid spacing, all values of  $\mu_x$  and  $\mu_y$  will be constant (1 if  $\Delta\alpha_1 = \Delta x$  and  $\Delta\alpha_2 = \Delta y$ ). The constants  $a_p$ ,  $b_p$ ,  $c_p$ ,  $a_q$ ,  $b_q$ , and  $c_q$  for all the regions and the values of  $\mu_x$  and  $\mu_y$  at grid cell faces and centers are determined using an interactive computer program called MAPIT. A plotting program called CMSGRID is used to plot the grids to a suitable scale for overlaying nautical charts such as those of the National Ocean Service (NOS).

10. Figures 3 and 4 show the two computational grids used to model St. Marys Inlet and surrounding areas. Both grids extend for 141,670 ft (23.3 nautical miles), in 90 grid cells, east-west and for 60,000 ft (9.9 nautical miles), in 50 cells, north-south. The grids are oriented so that one row of cells aligns with the navigation channel. The difference between the two grids lies in the mapping of 17 rows of cells in the area which covers St. Marys Inlet. Grid 1 (Figure 3) models the base condition of a 400-ft-wide navigation channel. The smallest cell, located near Ft. Clinch, has dimensions of 275 ft by 310 ft; while the largest cell, located at the eastern boundary of the grid, is 5,200 ft by 4,170 ft. The 25th cell row from the north edge of the grid overlays the channel. Grid 2 (Figure 4) models the plan condition of a 500-ft-wide channel. The smallest cell in Grid 2, also near Ft. Clinch, is 229 ft by 310 ft, while the largest cell size remains the same. The 17 rows of cells in the area of St. Marys Inlet have been remapped for Grid 2 so the 25th row again overlays the channel. This adjustment is accomplished by mapping slightly larger cells just north of the channel and slightly smaller cells just south of the channel. The mapping differences between Grids 1 and 2 are so minor that no bathymetric changes are required other than those in areas affected by dredging for the plan conditions.

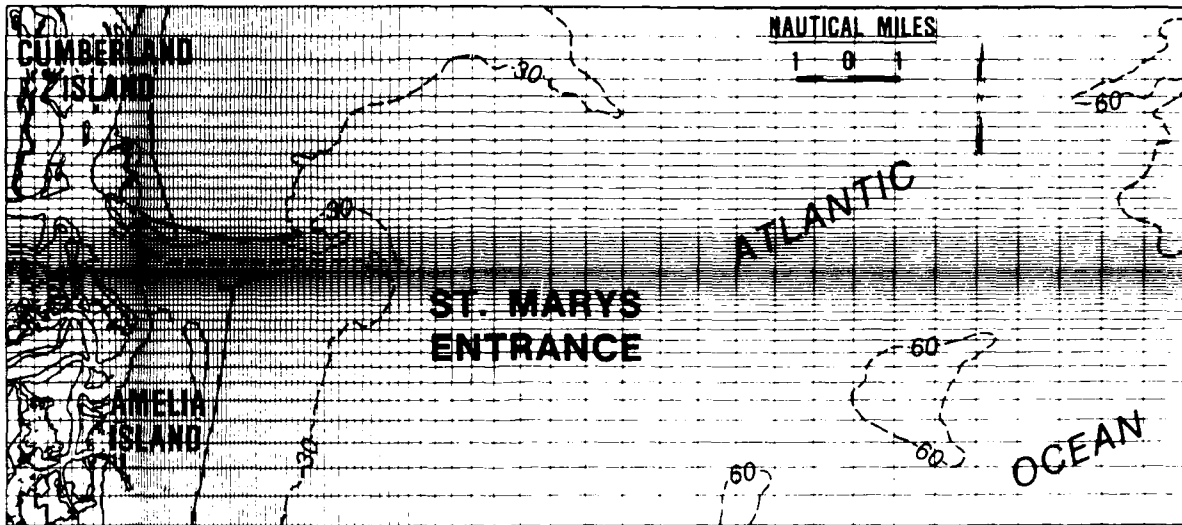


Figure 3. Computational grid for base condition

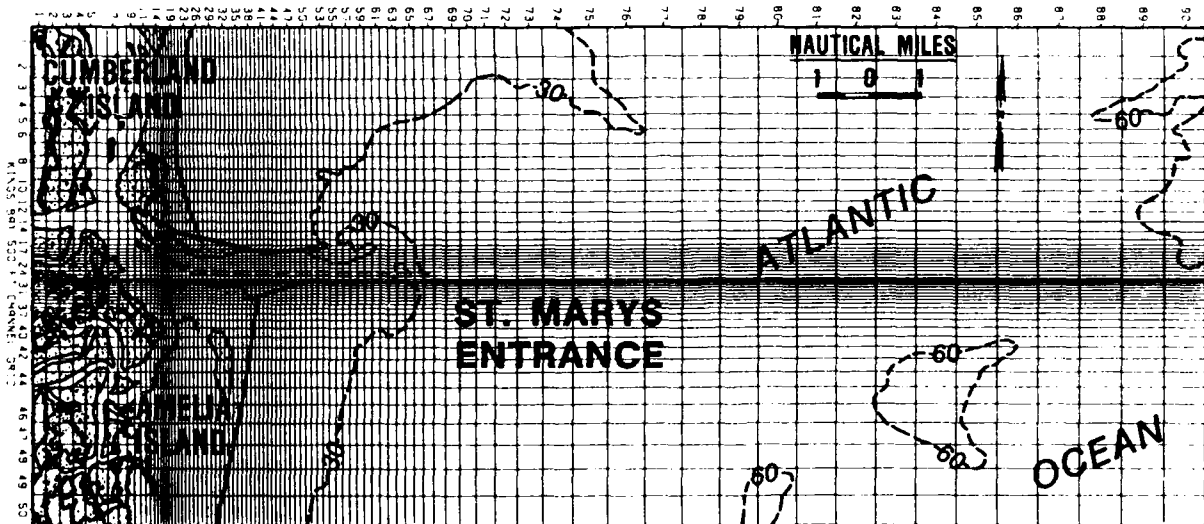


Figure 4. Computational grid for Plan 1 condition

11. Due to differences in required boundary conditions between the various models, and for reasons of economy, the first 17 columns of cells along the west side of the grids (the interior area) were not used in RCPWAVE, CURRENT, and the sediment transport model. This area is covered by Model A. WIFM required the additional cells in the interior area in order to use the prototype data available there for boundary conditions and to accurately simulate the complex tidal currents in the inlet.

#### The Tidal Simulation Model, WIFM

12. WIFM is a general long wave model which can be used for simulation of tides, storm surges, tsunamis, etc. It allows flooding and drying of land cells near the shoreline. It is a depth-averaged model so that variations in the vertical direction are averaged in the model. It is used in the present study to determine tidal elevations and velocities in the two horizontal coordinate directions. The following description of WIFM is extracted from a report by Leenknecht, Earickson, and Butler (1984).

#### Equations of motion

13. The hydrodynamics of the numerical model WIFM are derived from the Navier-Stokes equations in a Cartesian coordinate system (Figure 5). The long

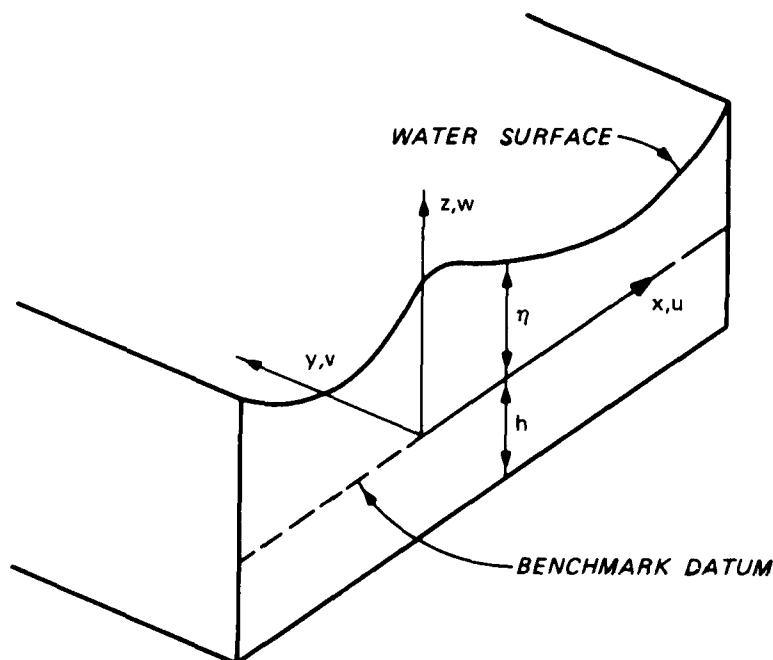


Figure 5. Coordinate system for WIFM

wave approximations of small vertical accelerations and a homogenous fluid yield the following vertically integrated (depth-averaged) two-dimensional equations of continuity and momentum:

Continuity

$$\frac{\partial \eta}{\partial t} + \frac{\partial}{\partial x} (ud) + \frac{\partial}{\partial y} (vd) = R \quad (7)$$

Momentum

$$\frac{\partial u}{\partial t} + u \frac{\partial u}{\partial x} + v \frac{\partial u}{\partial y} - fv + g \frac{\partial}{\partial x} (\eta - \eta_a) + \frac{gu}{C_z^2 d} (u^2 + v^2)^{1/2} - \epsilon \left( \frac{\partial^2 u}{\partial x^2} + \frac{\partial^2 u}{\partial y^2} \right) + F_x = 0 \quad (8)$$

$$\frac{\partial v}{\partial t} + u \frac{\partial v}{\partial x} + v \frac{\partial v}{\partial y} + fu + g \frac{\partial}{\partial y} (\eta - \eta_a) + \frac{gv}{C_z^2 d} (u^2 + v^2)^{1/2} - \epsilon \left( \frac{\partial^2 v}{\partial x^2} + \frac{\partial^2 v}{\partial y^2} \right) + F_y = 0 \quad (9)$$

where

$\eta$  = water surface elevation above datum

$t$  = time

$u, v$  = velocities in the x- and y-directions

$d = \eta + h$ , the total water depth

$h$  = local still-water depth

$R$  = rate of water volume change in the system due to rainfall or evaporation

$f$  = Coriolis parameter

$g$  = acceleration due to gravity

$C_z$  = Chezy coefficient for bottom friction

$\epsilon$  = eddy viscosity coefficient

The variable  $\eta_a$  accounts for hydrostatic water elevations due to atmospheric pressure differences, and  $F_x$  and  $F_y$  represent external forces such as wind stress.

Numerical method

14. The alternating-direction-implicit (ADI) method has been used by Leendertse (1970) and others to solve the two-dimensional equations of motion. When the advective terms are included in the momentum equations (Equations 8, 9) the ADI method has encountered stability problems. Weare (1976) indicates that the problems arise from approximating advective terms with one-sided differences in time and suggests the use of a centered scheme with three time-levels. WIFM employs a centered stabilizing-correction (SC) scheme which is second-order accurate in space and time, and boundary conditions can be formulated to the same order of accuracy. A brief development of the SC scheme is presented in the following paragraphs. Note that  $\eta$  and  $h$  are defined at the cell center and  $u$  and  $v$  at the cell faces.

15. The linearized equations of motion can be written in matrix form as:

$$U_t + AU_x + BU_y = 0 \tag{10}$$

where

$$U = \begin{bmatrix} \eta \\ u \\ v \end{bmatrix}$$

$$A = \begin{bmatrix} 0 & d & 0 \\ g & 0 & 0 \\ 0 & 0 & 0 \end{bmatrix}$$

$$B = \begin{bmatrix} 0 & 0 & d \\ 0 & 0 & 0 \\ g & 0 & 0 \end{bmatrix}$$

The SC scheme for solving Equation 10 is

$$(1 + \lambda_x) U^* = (1 - \lambda_x - 2\lambda_y) U^{k-1} \quad (11)$$

$$(1 + \lambda_y) U^{k+1} = U^* + \lambda_y U^{k-1} \quad (12)$$

where

$$\lambda_x = \frac{1}{2} \frac{\Delta t}{\Delta x} A \delta_x$$

$$\lambda_y = \frac{1}{2} \frac{\Delta t}{\Delta y} B \delta_y$$

The quantities  $\delta_x$  and  $\delta_y$  are centered difference operators, and the superscript  $k$  indicates time-level. The starred quantities can be considered intermediate values between the  $k$  and  $k+1$  time-levels.

16. The first step in the SC procedure computationally sweeps the grid in the  $x$ -direction, with the second step sweeping in the  $y$ -direction. Completing both sweeps constitutes a full time-step, advancing the solution from the  $k$  time-level to the  $k+1$  time-level. The form of the difference equations for the  $x$ -sweep is given by

$$\frac{1}{2\Delta t} (\eta^* - \eta^{k-1}) + \frac{1}{2\Delta x} \delta_x (u^* d + u^{k-1} d) + \frac{1}{\Delta y} \delta_y (v^{k-1} d) = 0 \quad (13)$$

$$\frac{1}{2\Delta t} (u^* - u^{k-1}) + \frac{g}{2\Delta x} \delta_x (\eta^* + \eta^{k-1}) = 0 \quad (14)$$

$$\frac{1}{2\Delta t} (v^* - v^{k-1}) + \frac{g}{\Delta y} \delta_y (\eta^{k-1}) = 0 \quad (15)$$

and the  $y$ -sweep by

$$\frac{1}{2\Delta t} (\eta^{k+1} - \eta^*) + \frac{1}{2\Delta y} \delta_y (v^{k+1} d - v^{k-1} d) = 0 \quad (16)$$

$$u^{k+1} = u^* \quad (17)$$

$$\frac{1}{2\Delta t} (v^{k+1} - v^*) + \frac{g}{2\Delta y} \delta_y (\eta^{k+1} - \eta^{k-1}) = 0 \quad (18)$$

17. Noting that  $v^*$  in Equation 15 is only a function of previously computed variables at the  $k-1$  time-level, its substitution into Equation 18 and the substitution of  $u^*$  (Equation 17) into Equations 13 and 14 yield the simplified forms

x-sweep

$$\frac{1}{2\Delta t} (\eta^* - \eta^{k-1}) + \frac{1}{2\Delta x} \delta_x (u^{k+1}_d + u^{k-1}_d) + \frac{1}{\Delta y} \delta_y (v^{k-1}_d) = 0 \quad (19)$$

$$\frac{1}{2\Delta t} (u^{k+1} - u^{k-1}) + \frac{g}{2\Delta x} \delta_x (\eta^* + \eta^{k-1}) = 0 \quad (20)$$

y-sweep

$$\frac{1}{2\Delta t} (\eta^{k+1} - \eta^*) + \frac{1}{2\Delta y} \delta_y (v^{k+1}_d - v^{k-1}_d) = 0 \quad (21)$$

$$\frac{1}{2\Delta t} (v^{k+1} - v^{k-1}) + \frac{g}{2\Delta y} \delta_y (\eta^{k+1} + \eta^{k-1}) = 0 \quad (22)$$

18. The details of applying the SC scheme to Equations 7-9 can be found in a report by Butler (in preparation). The diffusion terms of Equations 8 and 9 are also represented with time-centered approximations. The inclusion of diffusion terms contributes to the numerical stability of the scheme (Vreugdenhil 1973) and serves to somewhat account for turbulent momentum dissipation at the larger scales. While the resulting finite difference forms of Equations 7-9 appear cumbersome, they are efficient to solve. Application of the appropriate equation to one row or column of the grid (the "sweeping" process) results in a system of linear algebraic equations whose coefficient matrix is tridiagonal. Tridiagonal matrix problems can be solved directly, without the cost and effort of matrix inversion.

19. Apart from Courant number considerations, the computational time-step for the SC scheme in WIFM is largely governed by simple mass and momentum conservation principles. The maximum time-step for a problem is characterized by

$$\Delta t = \frac{n\Delta S}{V} \quad (23)$$

where  $V$  is the largest flow velocity to be encountered at a cell with its smallest side length  $\Delta S$ . The parameter  $n$  is of order 1. Therefore, the time-step is constrained by the smallest cell width which contains the highest flow velocity. In physical terms, Equation 23 requires that the flow cannot move substantially farther than one cell width in one time-step.

#### Boundary conditions

20. WIFM allows a variety of boundary conditions to be specified, which can be classified into three groups: open boundaries, land-water boundaries, and thin-wall barriers.

21. Open boundaries. When the edge of the computational grid is defined as water, such as a seaward boundary or a channel exiting the grid, either the water elevation or the flow velocities can be specified as an open boundary-condition. This information can be input to WIFM as tabular data, or constituent tides can be calculated within the model during the time-stepping process.

22. Land-water boundaries. WIFM allows land-water boundaries to be either fixed or variable to account for flooding in low-lying terrain. Fixed boundaries specify a no-flow condition at the cell face between land and water. The position of a variable boundary is determined by the relationship of the water elevation at a "wet" cell to the land elevation at a neighboring "dry" cell. Once a water elevation rises above the level of adjacent land height, water is initially moved onto the "dry" cell by using a broad-crested weir formula (Reid and Bodine 1968). When the water level on the dry cell exceeds some small value, the boundary face is treated as open, and computations for  $\eta$ ,  $u$ , and  $v$  are made at the now "wet" cell. Drying is the inverse process, and mass is conserved in these procedures.

23. Thin-wall barriers. These barriers are defined along cell faces and are of three types: exposed, submerged, and overtopping. Exposed barriers allow no flow across a cell face. Submerged barriers control flow across a cell face by using a time-dependent friction coefficient. Overtopping barriers are dynamic. They can be completely exposed, completely submerged, or they can act as broad-crested weirs. The barrier character is determined by its height and the water elevations in the two adjoining cells.

The Wave Model, RCPWAVE

24. The RCPWAVE model is a linear short-wave model which considers transformation of surface gravity waves in shallow water including the processes of shoaling, refraction, and diffraction due to bathymetry and allows for wave breaking and decay within the surf zone (the region shoreward of the breaker line). Unlike traditional wave-ray tracing methods, the model uses a rectilinear grid so that model output in the form of wave height, direction, and wave number is available at the centers of the grid cells. This availability is highly advantageous since the information can be used directly as input to the wave-induced current and sediment transport models, and the problem of caustics due to crossing of wave rays is avoided. The description of RCPWAVE that follows is extracted from a report by Ebersole, Cialone, and Prater (1986).

25. Berkhoff (1972 and 1976) derived an elliptic equation approximating the complete wave transformation process for linear waves over an arbitrary bathymetry constrained only to have mild bottom slopes (thus the designation mild slope equation (Smith and Sprinks 1975)). The mild slope equation can be expressed in the following form:

$$\frac{\partial}{\partial x} \left( c c_g \frac{\partial \phi}{\partial x} \right) + \frac{\partial}{\partial y} \left( c c_g \frac{\partial \phi}{\partial y} \right) + \sigma^2 \frac{c_g}{c} \phi = 0 \quad (24)$$

where

$\phi(x,y)$  = complex velocity potential

$\sigma$  = wave angular frequency =  $\frac{2\pi}{T}$

$T$  = wave period

$c(x,y)$  = wave celerity =  $\frac{\sigma}{k}$

$c_g(x,y)$  = group velocity =  $\frac{\partial \sigma}{\partial k}$

$k(x,y)$  = wave number given by the dispersion relation

$$\sigma^2 = gk \tanh(kh) \quad (25)$$

26. Numerical solution of this equation for the velocity potential field is an effective means for solving the complete wave propagation problem.

The equation can be solved using either finite element (for example, Berkhoff 1972, Houston 1981) or finite difference methods (for example, William, Darbyshire, and Holmes 1980). Since transmission and reflection boundary conditions are easily implemented into these solution schemes, this approach is a popular one for modeling tsunami propagation and for solving problems involving the response of harbors to short and long waves. This method becomes computationally infeasible for large scale, open coast, short-wave problems because of its great expense.

27. The model RCPWAVE is an alternative approach for solving the open coast wave propagation problem. It addresses the processes of refraction and diffraction and can be applied to a large region quite economically. The model also contains an algorithm which estimates wave conditions inside the surf zone. This wave breaking model is an extension of the work of Dally, Dean, and Dalrymple (1984) to two horizontal dimensions.

Wave transformation outside  
the surf zone: theoretical basis

28. The velocity potential function for linear, monochromatic, plane waves can be represented by the following expression:

$$\phi = a e^{is} \quad (26)$$

where

$$a(x,y) = \text{wave amplitude function equal to } \frac{g H(x,y)}{2\sigma}$$

$$H(x,y) = \text{wave height}$$

$$s(x,y) = \text{wave phase function}$$

Here the velocity potential function describes only the forward scattered wave field. No considerations are given to wave reflections. By substituting this expression for the velocity potential into Equation 24 and solving the real and imaginary parts separately, two equations can be derived (Berkhoff (1976)), namely,

$$\frac{1}{a} \left[ \frac{\partial^2 a}{\partial x^2} + \frac{\partial^2 a}{\partial y^2} + \frac{1}{cc_g} \left( \nabla a \cdot \nabla (cc_g) \right) \right] + k^2 - |\nabla s|^2 = 0 \quad (27)$$

$$\nabla \cdot (a^2 cc_g \nabla s) = 0 \quad (28)$$

where the symbol  $\nabla$  denotes the horizontal gradient operator.

29. Together, these equations describe the combined refraction and diffraction process. Diffraction is often erroneously described as the propagation of energy along wave crests which are defined to be perpendicular to the wave phase function gradient  $\nabla s$ . Equation 28 shows energy is still propagated in a direction perpendicular to the wave crest. Diffractive effects do change the phase function as a result of significant gradients and curvatures of the wave height. These changes cause the local wave direction to vary. If diffractive effects are neglected, Equations 27 and 28 reduce to those describing pure refraction in which the wave number represents the magnitude of the phase function gradient.

30. Linear wave theory assumes irrotationality of the wave phase function gradient. This property can be expressed mathematically as

$$\nabla \times (\nabla s) = 0 \quad (29)$$

The phase function gradient can be written in vector notation as

$$\nabla s = |\nabla s| \cos \theta \vec{i} + |\nabla s| \sin \theta \vec{j} \quad (30)$$

where  $\vec{i}$  and  $\vec{j}$  are unit vectors in the x- and y-directions, respectively, and  $\theta(x,y)$  is the local wave direction. Equations 29 and 30 can be combined to yield the following expression:

$$\frac{\partial}{\partial x} (|\nabla s| \sin \theta) - \frac{\partial}{\partial y} (|\nabla s| \cos \theta) = 0 \quad (31)$$

If the magnitude of the wave phase function is known, local wave angles can be calculated from Equation 31. Similarly, Equation 30 can be substituted into Equation 28 to yield

$$\frac{\partial}{\partial x} (a^2 c c_g |\nabla s| \cos \theta) + \frac{\partial}{\partial y} (a^2 c c_g |\nabla s| \sin \theta) = 0 \quad (32)$$

This form of the energy equation can be solved for the wave amplitude function  $a$  once the wave phase characteristics  $\nabla s$  and  $\theta$  are known. The wave

height can be determined and is proportional to the amplitude function since wave frequency is constant.

31. Equations 27, 31, and 32 along with the dispersion relation describe the combined refraction and diffraction process for linear plane waves subject to the restrictions that the bottom slopes are small, wave reflections are negligible, and any energy losses are very small and can be neglected. These equations are assumed to be valid outside the surf zone. The numerical solution scheme used to solve these equations is presented in the next section.

Wave transformation outside  
the surf zone: numerical solution

32. The three governing equations (27, 31, and 32) are solved using numerical methods. Partial derivatives within the equations are approximated using finite difference operators. Finite difference solution methods require the construction of a computational grid system or mesh. Solution accuracy is directly related to resolution within the grid system. Discussions throughout this section refer only to grid systems comprised of constant sized, rectangular cells. RCPWAVE is capable of computing solutions on variably sized, rectilinear grid systems.

33. Figure 6 shows nine rectangular cells which make up a small part of a larger mesh. Each cell has a length equal to  $\Delta x$  in the x-direction and  $\Delta y$  in the y-direction. The maximum values of  $i$  and  $j$  are  $M$  and  $N$ , respectively. All variables which vary as a function of space are defined at the cell centers (see Ebersole, Cialone, and Prater (1986) for details of the finite difference procedure used).

34. Model input includes values of the deepwater height  $H_0$ , direction  $\theta_0$ , and period  $T$  of waves to be simulated. It also includes specification of the bottom bathymetry throughout the grid. The wave number, which is related to the wave period and the local water depth through the dispersion relation, is computed at every cell. It is used as an initial guess for the magnitude of the wave phase function gradient. The wave celerity  $c$  and the group velocity  $c_g$  are functions of the wave period, wave number, and water depth. Therefore these variables can be calculated at each cell.

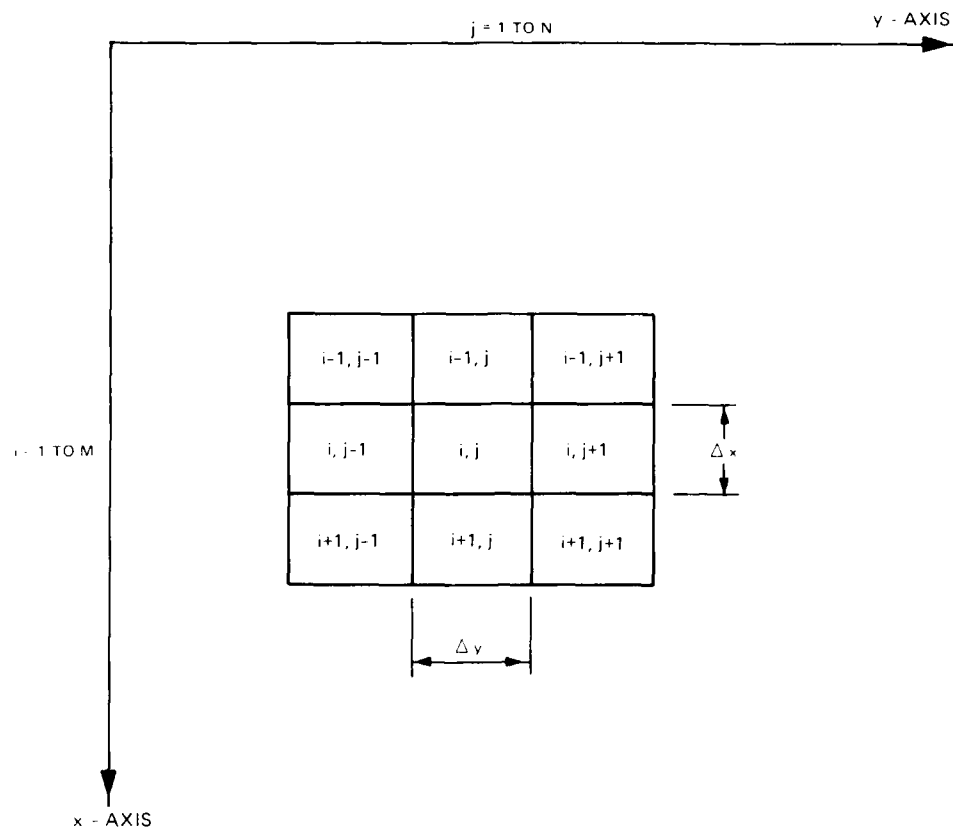


Figure 6. Definition of coordinate system and grid cell conventions used in RCPWAVE

35. From Snell's law,

$$\frac{\sin \theta}{c} = \frac{\sin \theta_o}{c_o} \quad (33)$$

where  $c_o$  is the deepwater wave celerity (defined to be  $\frac{gT}{2\pi}$ ), an estimate of the local wave angle is obtained everywhere. This estimate assumes that the bottom contours are parallel with the y-axis. If the bottom bathymetric contours make a known nonzero angle with the y-axis, a better first guess for the wave angles can be made. The new approximation is

$$\theta = \pi - \sin^{-1} \left( \frac{\sin(\theta_o - \theta_c)}{\frac{c_o}{c}} \right) + \theta_c \quad (34)$$

where  $\theta_c$  defines the "contour angle." The local wave angle, deepwater wave angle, and contour angle follow the angle convention shown in Figure 7. The contour angle is an input parameter for RCPWAVE.

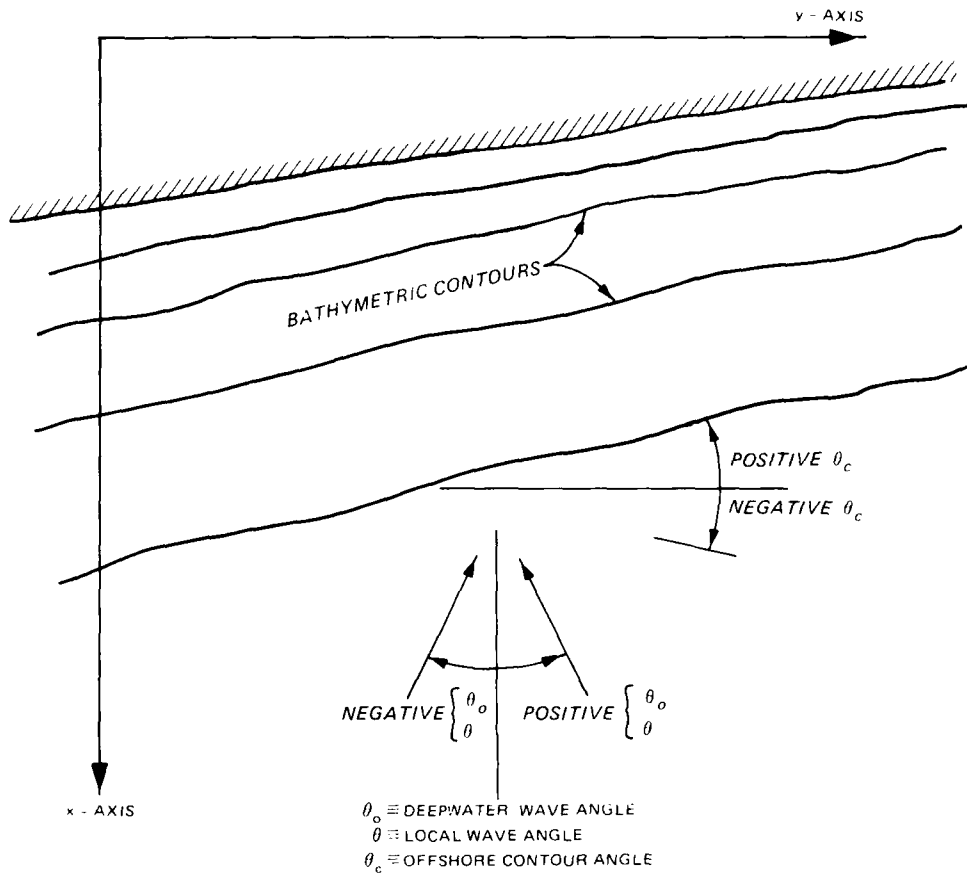


Figure 7. Definition of angle conventions used in RCPWAVE

36. Wave heights at each cell are estimated as the product of the deep-water wave height, a shoaling coefficient  $\kappa_s$ , and a refraction coefficient  $\kappa_r$ , thus

$$H = H_o \kappa_r \kappa_s \quad (35)$$

where

$$\kappa_r = \left( \frac{\cos \theta_o}{\cos \theta} \right)^{1/2} \quad (36)$$

and

$$\kappa_s = \left\{ \frac{1}{\left[ 1 + \frac{2kh}{\sinh(2kh)} \right] \tanh(kh)} \right\}^{1/2} \quad (37)$$

The dispersion relation, Snell's law, and this simple estimator of the wave height allow an initial guess to be made for the variables of interest throughout the grid system.

37. The solution scheme implements the following marching procedure once initial guesses for the variables of interest have been made. Starting at the offshore row designated by  $i=M-3$ , Equations 31 and 32 are used to compute wave angles and then heights along the entire row (from  $j=2$  to  $j=N-1$ ). Wave height is used interchangeably with amplitude function since one is directly proportional to the other.

38. Wave angles and heights along a given row are solved for iteratively because of the implicit differencing formulation used. Calculations of the wave angle (actually the sine of the wave angle) and the wave amplitude function are repeated until the average change (along a row) in each variable from one iteration to the next is less than some tolerance. These convergence criteria, 0.0005 for sines of the wave angles and 0.001 ft (or a metric equivalent) for wave heights, are suggested values for prototype applications.

39. This solution considers only refraction since the wave number  $k$  is used as an estimate of the magnitude of the phase function gradient. Equation 27 is then used to compute the true magnitude of the wave phase gradient. This "new wave number" accounts for the effects of diffraction. Backwards differences are used to approximate the x-derivatives because they only require information which has already been computed. Next, Equations 31 and 32 are again solved in order to compute the wave angles and heights using these new wave numbers. This procedure is repeated along the row under consideration until the change in new wave number, from one iteration to the next, is less than 0.5 percent of the newly computed value. This condition must be met at each cell along the row. As a row of new wave numbers is computed, the values are filtered in the y-direction using the method of Sheng, Segur, and Lewellen (1978). This filter removes cell-to-cell oscillations introduced as a result of the differencing scheme used to compute the new wave numbers. Row-by-row marching proceeds until solutions are computed along row  $i=2$ .

40. Lateral boundary conditions for a row are specified at the conclusion of calculations for that row. The value of all variables at cells  $j=N$  and  $j=1$  are set equal to their values at cells  $j=N-1$  and  $j=2$ , respectively. This boundary condition implies that the change in the variable in the y-direction is zero. The condition is most valid when the bathymetric contours are nearly straight and parallel to the y-axis. For this reason the grid is oriented so that the y-axis is nearly parallel to bottom contours along the lateral boundaries.

41. Boundary conditions along the offshore boundary of the grid are used to initiate the shoreward marching algorithm. They are computed from deepwater wave input supplied by the user along with the following assumption. Bottom contours extending from the offshore grid row ( $i=M$ ) out to deep water are assumed to be straight and parallel to a line making an angle of  $\theta_c$  with the y-axis. In other words, Snell's law is assumed to be valid from deep water to the outer boundary of the grid system. No inshore boundary conditions (along row  $i=1$ ) are required because of the forward marching solution scheme.

Wave transformation  
inside the surf zone

42. Waves approaching the very nearshore zone tend to steepen and eventually break because of decreasing water depths. Shoreward of this breaking point dissipative energy losses due to turbulence strongly influence the wave height. Linear theory does not allow for prediction of the breaker location nor for wave transformation across the surf zone. Instead, empirical and approximate methods must be used to describe the breaking process.

43. The first aspect to consider in surf zone transformation of waves is incipient wave breaking. RCPWAVE uses the following criterion of Weggel (1972):

$$H_b = \frac{\bar{b}h_b}{1 + \frac{\bar{b}a}{gT^2}} \quad (38)$$

where

$H_b$  = breaking wave height

$$\bar{b} = \frac{1.56}{(1 + e^{-19.5m})}$$

m = bottom slope

$h_b$  = water depth at breaking

$$\bar{a} = 43.75 (1 - e^{-19m})$$

because it accounts for bottom slope and wave period.

44. Once the incipient breaking point is defined, a mechanism is needed to transform the breaking wave across the surf zone. The transformation algorithm selected for use in RCPWAVE (Dally, Dean, and Dalrymple 1984) uses an energy flux basis. Through analogy with energy loss in a hydraulic jump in a channel, the following equation is postulated for one-dimensional transformation of waves advancing in the -x direction:

$$\frac{d(Ec_g)}{dx} = \frac{\kappa}{h} \left[ Ec_g - (Ec_g)_s \right] \quad (39)$$

where

$Ec_g$  = energy flux associated with the breaking wave

$\kappa$  = rate of energy dissipation coefficient (set equal to 0.2 in RCPWAVE)

$(Ec_g)_s$  = stable level of energy flux that the transformation process seeks to attain

The right side of Equation 39 is simply a dissipation term. The subscript s is used to denote the stable level of a variable. Substituting the linear wave theory estimate for E ( $E = 0.125 \rho g H^2$ ) into Equation 39 results in the following expression:

$$\frac{d(H^2c_g)}{dx} = \frac{\kappa}{h} \left[ H^2c_g - (H^2c_g)_s \right] \quad (40)$$

45. Various field (Thornton and Guza 1982) and laboratory (Horikawa and Kuo 1966) experiments have shown that, well into the surf zone, the wave height tends toward a stable value which is proportional to the local water depth. This relationship can be expressed as

$$H_s = \Gamma h \quad (41)$$

where

$H_s$  = stable wave height

$\Gamma$  = proportionality coefficient (set equal to 0.4 in RCPWAVE)

Equation 40 can now be rewritten as

$$\frac{d(H^2 c_g)}{dx} = \frac{\kappa}{h} \left[ H^2 c_g - (\Gamma^2 h^2 c_g)_s \right] = D \quad (42)$$

46. This surf zone wave transformation model, extended to two dimensions, can be incorporated into the conservation of wave energy equation (Equation 28) by simply adding a dissipation term  $D$  to the right side. The function  $D$  must now represent dissipation in the direction of wave propagation. Also for dimensional consistency, the term  $D$  must be multiplied by the wave celerity and the magnitude of the wave phase gradient, and the wave height must be replaced by the wave amplitude function. In vector notation, the energy equation becomes

$$\nabla \omega (a^2 c c_g \nabla s) = \frac{\kappa}{h} \left\{ a^2 c c_g |\nabla s| - \left[ \left( \frac{g}{2\sigma} \right)^2 \Gamma^2 h^2 c c_g |\nabla s| \right]_s \right\} \quad (43)$$

This equation can be thought of as being valid both inside and outside the surf zone. Outside, the coefficient  $\kappa$  is zero, and the equation reduces to Equation 28.

47. All discussion relating to wave transformation within the surf zone up to this point has addressed the problem of determining wave heights. The problem of wave phase must be addressed also. Diffraction effects are assumed to be negligible inside the surf zone. Therefore, the wave number  $\kappa$  is assumed to accurately represent the magnitude of the wave phase function gradient. The linear wave theory assumption that the waves are irrotational also will be assumed to remain valid inside the surf zone. Consequently, wave angles are computed in the same manner as outside the surf zone. Details concerning the numerical solution inside the surf zone can be found in Ebersole, Cialone, and Prater (1986).

## The Wave-Induced Current Model, CURRENT

48. When waves break and decay in the surf zone, in general they induce currents in the longshore and cross-shore directions and changes in the mean water level. These currents play a major role in the movement of sediment in the nearshore. They are computed using the model CURRENT.

### Equations of motion

49. The hydrodynamic equations used in the model for wave-induced currents may be derived from the Navier-Stokes equations (for details, see Phillips 1969 and Ebersole 1980). It is assumed in the derivation that the fluid is homogeneous and incompressible, and the vertical accelerations are negligible so that the pressure distribution is hydrostatic. By vertically integrating the three-dimensional form of the equations and applying appropriate boundary conditions, the depth-averaged two-dimensional form of the equations of motion and continuity are obtained. These equations are derived by time-averaging over a time interval corresponding to the period of the waves. Referring to a Cartesian coordinate scheme (Figure 8), these are:

### Momentum

$$\frac{\partial U}{\partial t} + U \frac{\partial U}{\partial x} + V \frac{\partial U}{\partial y} + g \frac{\partial \bar{\eta}}{\partial x} + \frac{1}{\rho d} \tau_{bx} + \frac{1}{\rho d} \left( \frac{\partial S_{xx}}{\partial x} + \frac{\partial S_{xy}}{\partial y} \right) - \frac{1}{\rho} \frac{\partial \tau_{xy}}{\partial y} = 0 \quad (44)$$

$$\frac{\partial V}{\partial t} + U \frac{\partial V}{\partial x} + V \frac{\partial V}{\partial y} + g \frac{\partial \bar{\eta}}{\partial y} + \frac{1}{\rho d} \tau_{by} + \frac{1}{\rho d} \left( \frac{\partial S_{xy}}{\partial x} + \frac{\partial S_{yy}}{\partial y} \right) - \frac{1}{\rho} \frac{\partial \tau_{xy}}{\partial x} = 0 \quad (45)$$

### Continuity

$$\frac{\partial \bar{\eta}}{\partial t} + \frac{\partial}{\partial x} (Ud) + \frac{\partial}{\partial y} (Vd) = 0 \quad (46)$$

where

U and V = depth-averaged horizontal velocity components at time t in the x- and y-directions, respectively, ft/sec

$\bar{\eta}$  = displacement of the mean free surface with respect to the still-water level, ft

$\rho$  = mass density of seawater, slugs/ft<sup>3</sup>



The condition  $\bar{\eta} > 0$  is known as setup, and  $\bar{\eta} < 0$  is called setdown.

50. Bottom friction. At present, the numerical model uses a linear formulation for friction (Longuet-Higgins 1970). Thus

$$\tau_{bx} = 2\rho c \langle |u_{orb}| \rangle U \quad (47)$$

$$\tau_{by} = \rho c \langle |u_{orb}| \rangle V \quad (48)$$

where  $c$  is a drag coefficient (of the order of 0.01) and  $\langle |u_{orb}| \rangle$  is the time average, over one wave period, of the absolute value of the wave orbital velocity at the bottom. From linear wave theory

$$\langle |u_{orb}| \rangle = \frac{2H}{T \sinh kh} \quad (49)$$

Equations 47 and 48 are based on the assumption that the velocity components  $U$  and  $V$  of the current are small compared with the wave orbital velocity,  $\langle |u_{orb}| \rangle$ .

51. Radiation stresses. The radiation stresses are of major importance since they furnish the main forces for creating wave-induced currents. Referring to Longuet-Higgins (1970), for monochromatic waves, they are defined in terms of the local wave climate as follows:

$$S_{xx} = E \left[ \left( 2n - \frac{1}{2} \right) \cos^2 \theta + \left( n - \frac{1}{2} \right) \sin^2 \theta \right] \quad (50)$$

$$S_{xy} = E n \cos \theta \sin \theta \quad (51)$$

$$S_{yy} = E \left[ \left( 2n - \frac{1}{2} \right) \sin^2 \theta + \left( n - \frac{1}{2} \right) \cos^2 \theta \right] \quad (52)$$

where

$$n = \frac{1}{2} \left( 1 + \frac{2kh}{\sinh 2kh} \right) \quad (53)$$

( $n$  is the ratio of wave group celerity to phase celerity),  $\theta$  is the local wave direction (defined as shown in Figure 8), and  $E$  is the wave energy density. The values of  $H$ ,  $k$ , and  $\theta$  are obtained from RCPWAVE.

52. Lateral shear. In the numerical model, the coordinate scheme is chosen such that  $x$  is positive in the offshore direction and  $y$  is approximately in the alongshore direction. An eddy viscosity formulation is chosen for the lateral shear. The eddy viscosity is assumed to be anisotropic. Denoting  $\epsilon_x$  and  $\epsilon_y$  as the eddy viscosities in  $x$ - and  $y$ -directions, respectively, in general,  $\epsilon_x$  is assumed to be a function of  $x$  and  $y$  and  $\epsilon_y$  a constant. Accordingly,

$$\tau_{xy} = \rho \left( \epsilon_y \frac{\partial U}{\partial y} + \epsilon_x \frac{\partial V}{\partial x} \right) \quad (54)$$

For field applications, the eddy viscosity  $\epsilon_x$  is chosen according to the following relation given by Jonsson, Skovgaard, and Jacobsen (1974):

$$\epsilon_x = \frac{H^2 g T}{4\pi^2 h} \cos^2 \theta \quad (55)$$

This represents twice the value used by Thornton (1970). The value of  $\epsilon_y$  was, in general, taken to be equal to the value of  $\epsilon_x$  at the deepest part (usually near the offshore boundary) of the numerical grid.

#### Method of solution

53. In view of the similarity among Equations 44-46 and the equations for long waves (Equations 7-9), CURRENT was developed by modifying WIFM. Thus CURRENT also is an implicit finite difference model and uses the SC scheme described previously. Details of the method of solution can be found in Vemulakonda (1984).

#### Initial and boundary conditions

54. In order to solve the problem under consideration, appropriate initial and boundary conditions must be specified. Usually an initial condition of rest is chosen so that  $\bar{\eta}$ ,  $U$ , and  $V$  are zero at the start of the calculations. To avoid shock, the radiation stress gradients are gradually built up to their full values over a number of time-steps. The numerical computation is stopped when a steady state is deemed to have been reached.

55. The numerical model permits various types of boundary conditions among which are the following:

- a. "No flow" (wall). This type of boundary condition is used at closed boundaries such as the still-water line on beaches and at impermeable structures. The normal velocity is set to zero in this case.
- b. Uniform flux. In this type of open boundary condition, the flux at a boundary cell is made equal to that at the next interior cell. Thus the condition assumes  $\partial(Ud)/\partial x = 0$  or  $\partial(Vd)/\partial y = 0$  at the boundary. This type of condition is used for the lateral boundaries since it is a passive condition.
- c. Radiation. This open boundary condition requires that any transients developed initially inside the numerical grid should propagate out of the grid as gravity waves. It is of the form  $\partial\eta/\partial t + c(\partial\eta/\partial x) = 0$  where  $c$  is the phase speed of a surface disturbance  $\eta(x,t)$ . It is often used by the wave-induced current model at the offshore boundary and is found preferable to a wall or constant elevation condition there. Both of the latter conditions are highly reflective, and, as a result, the transients tend to bounce back and forth between the offshore and nearshore boundaries and take a long time to damp out. On the other hand, the radiation condition seems to work quite well, allowing the transients to propagate out of the grid and permitting the setdown at the offshore boundary to assume an appropriate value.

56. The boundary conditions frequently used in the wave-induced current model are illustrated in Figure 9.

57. At present, the model allows for subgrid (thin-wall) barriers such as jetties, provided they are impermeable and nonovertopping. The program essentially sets to zero the velocity component normal to the appropriate cell face.

#### The Sediment Transport Model

58. The sediment transport model predicts the transport, deposition, and erosion of noncohesive sediments such as sands in open coast areas as well as in the vicinity of tidal inlets. It accounts for both tides and wave action by using for input the results of WIFM, RCPWAVE, and CURRENT in terms of tidal elevations and currents, wave climate information, wave-induced currents, and setups at the centers of grid cells. The model computes transport separately for straight open coast areas and areas in the vicinity of tidal inlets. In the case of the former, transports inside and outside the surf zone are treated separately.

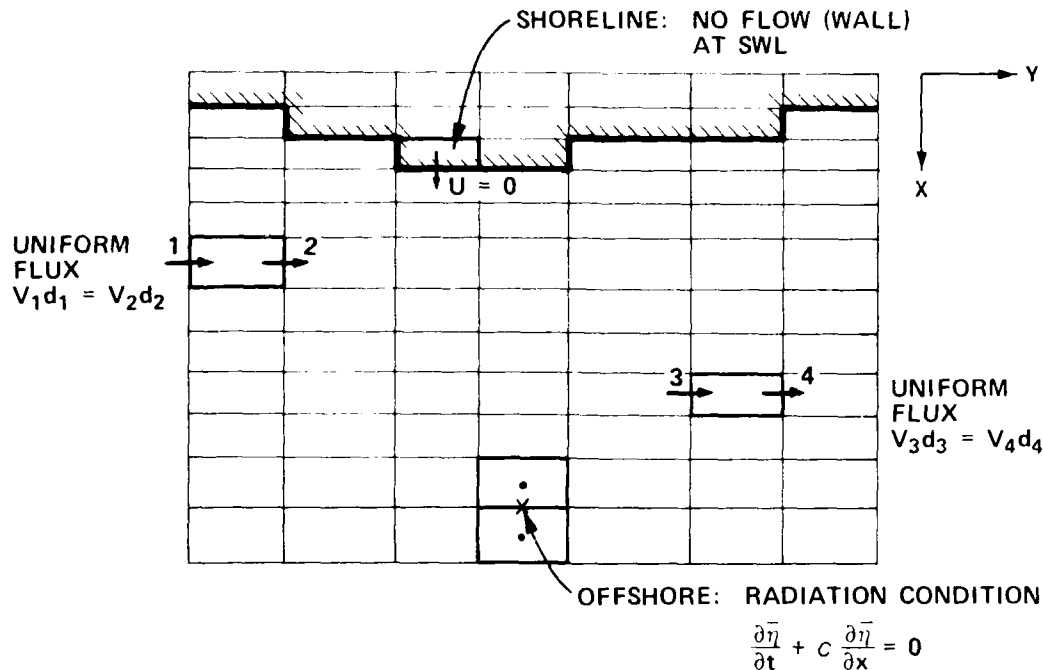


Figure 9. Boundary conditions used in numerical model CURRENT

#### Transport inside the surf zone

59. Inside the surf zone it is the wave breaking process that is primarily responsible for the transport of sediment. This process is quite complex and not well understood. There is even considerable disagreement on the primary mode (bed load or suspended load) of sediment transport in the surf zone (Komar 1978). Thus a model that determines transport in the surf zone must be empirical, to some degree, in its formulation.

60. The surf zone transport model used in this study is based upon an energetics concept developed by Bagnold (1963) who reasoned that the wave orbital motion provides a stress that moves sediment back and forth in an amount proportional to the local rate of energy dissipation. Although there is no net transport as a result of this motion, the sediment is in a dispersed and suspended state so that a steady current of arbitrary strength will transport the sediment. Thus breaking waves provide the power to support sand in a dispersed state (bed and suspended load), while a superimposed current (littoral, rip, tidal) produces net sand transport.

61. The total littoral transport rate  $I_l$  (vertically integrated and parallel to the shoreline) within the surf zone can be related to the wave conditions at the breaker line by

$$I_{\ell} = K(Ec_g)_b \sin \alpha_b \cos \alpha_b \quad (56)$$

where

$I_{\ell}$  = immersed weight sand transport rate (lb/sec)

K = empirical coefficient

$\alpha_b$  = breaker angle

and the subscript b is used to denote conditions at the breaker line.

62. Following Komar (1977), the local (vertically integrated) immersed weight longshore transport rate, per unit width in the cross-shore direction, may be written as

$$i_{\ell} = \frac{\pi k_1}{4} (0.5f) \rho g \gamma^2 h v_{\ell} \quad (57)$$

where

$k_1$  = coefficient to be determined

f = drag coefficient

$\gamma = \frac{H}{h}$  = breaker index

$v_{\ell}$  = local longshore velocity

63. By integrating  $i_{\ell}$  across the width of the surf zone  $x_b$ ,

$$I_{\ell} = \int_0^{x_b} i_{\ell} dx \quad (58)$$

or

$$I_{\ell} = \frac{\pi k_1}{4} (0.5f) \rho g \int_0^{x_b} \frac{H^2}{h} v_{\ell} dx \quad (59)$$

under the assumption that the coefficients  $k_1$  and f are constants for a particular field site. Since the values of H,  $v_{\ell}$ , and h are known, being input to the sediment model, the integral on the right side of Equation 59 may be determined numerically. For example, using the trapezoidal rule,

$$I_2 \equiv \int_0^{x_b} \frac{H^2}{h} v_\ell dx \approx \sum_{i=1}^{IMAX-1} \left[ \frac{\Delta x_i}{2} \left( \frac{H_i^2 v_i}{h_i} + \frac{H_{i+1}^2 v_{i+1}}{h_{i+1}} \right) \right] \quad (60)$$

where IMAX corresponds to the number of water cells within the surf zone. Equation 60 allows for a gradual variation in cell size  $\Delta x$ . The velocity  $v_\ell$  is taken as the magnitude of the resultant of the total velocity components  $u_T$  and  $v_T$  in the x- and y-directions. Thus

$$v_\ell = \sqrt{u_T^2 + v_T^2} \quad (61)$$

where

$$u_T = u + U \quad (62)$$

$$v_T = v + V \quad (63)$$

For each computational grid line from the shoreline to the breaker line for each time-step, the value of  $I_2$  is used to determine the unknown coefficient  $k_1$  from Equations 56 and 59:

$$k_1 = \frac{KH_b^2 c_{gb} \sin \alpha_b \cos \alpha_b}{\pi f I_2} \quad (64)$$

The value of  $K$  is taken to be 0.39 if significant wave heights are used as in this study (Shore Protection Manual (SPM) 1984).

64. Once  $k_1$  is known, the local transport rate  $i_\ell$  may be determined from Equation 57 and hence the local volumetric sediment transport rate  $q_\ell$ , as in the following equation:

$$q_\ell = \frac{\pi k_1 f \rho \gamma^2 h v_\ell}{8 (\rho_s - \rho) a'} \quad (65)$$

where

$\rho_s$  = mass density of solids  
 $\approx 2.65 \rho$  for sand

$a'$  = ratio of volume of solids to total volume of sediment  
 $= 0.6$  for sand

It is not necessary to know the value of  $f$  in order to solve for  $q_\ell$  in the above procedure. Once  $q_\ell$  is known, the local volumetric sediment transport rates  $q_x$  and  $q_y$  for the cell may be determined by multiplying  $q_\ell$  by  $u_T/v_\ell$  and  $v_T/v_\ell$ , respectively.

Transport beyond the surf zone

65. Beyond the surf zone, waves are not breaking. Currents (tidal, littoral, and rip) still transport sediment, but the sediment load is much smaller than the load in the surf zone. Waves still assist in providing power to support sand in a dispersed state. However, there is little turbulent energy dissipation, and frictional energy dissipated on the bottom represents most of the energy dissipation. Bed load is the primary mode of sediment transport beyond the surf zone according to Thornton (1972).

66. Since beyond the surf zone it is the tractive forces of currents (including wave orbital velocity currents) that produce sediment movement, a sediment transport by currents approach is taken. Again, since the complete physics of the problem is not completely understood, a semiempirical approach must be taken. In this model, the approach of Ackers and White (1973) is followed after appropriate modification for the influence of waves.

67. Ackers and White (1973) studied sediment transport due to currents. They used the results of 925 individual sediment transport experiments to establish various empirical coefficients. The approach considers both suspended load and bed load. It is assumed that the rate of suspended load transport is dependent upon the total shear on the bed. Therefore, the shear velocity  $v_*$  is the important velocity for suspended load transport. Bed load transport, however, is assumed to depend upon the actual shear stress on individual sediment grains. Ackers and White (1973) assume that this stress is comparable with the shear stress that would occur on a plane granular surface bed with the same mean stream velocity. Thus the mean velocity of flow  $v$  is the important velocity for bedload transport.

68. Considering only currents (not waves), Ackers and White (1973) derived sediment transport rate in a dimensionless form. For convenience in practical application, this may be written as

$$q = \frac{v}{(1-p)} D \left( \frac{v}{v_*} \right)^{n_1} \frac{C}{A^{m_1}} (F - A)^{m_1} \quad (66)$$

where

q = total volumetric sediment transport rate per unit width normal to the current (vertically integrated combined bed and suspended sediment load (ft<sup>3</sup>/sec/ft)

p = porosity of sediment = 1 - a'

D = sediment diameter which is exceeded in size by 65 percent (by weight) of the total sample

$$n_1 = 1.0 - 0.2432 \ln Y \quad (67)$$

$$Y = D \left[ \frac{g(s-1)}{v^2} \right]^{1/3} \quad (68)$$

s = specific gravity of sediment

v = kinematic viscosity of fluid

$$C = \exp \left[ 2.86 \ln Y - 0.4343 (\ln Y)^2 - 8.128 \right] \quad (69)$$

$$A = \frac{0.23}{Y^{1/2}} + 0.14 \quad (70)$$

$$m_1 = \frac{9.66}{Y} + 1.34 \quad (71)$$

$$F = \frac{v \left( \frac{v_*}{v} \right)^{n_1} \left( \sqrt{32} \log \frac{10 h}{D} \right)^{n_1-1}}{\left[ g(s-1)D \right]^{1/2}} \quad (72)$$

Equations 67, 69, 70, and 71 apply for  $1 < Y \leq 60$  (transition sediments).

For values of Y greater than 60 (coarse sediments), C,  $n_1$ ,  $m_1$ , and A have the values of 0.025, 0, 1.5 and 0.17, respectively.

69. Beyond the surf zone, both currents and nonbreaking waves exist. So the Ackers and White formulation derived originally for currents only must be modified for the presence of waves. The waves do not increase the level of turbulence since turbulence is confined to a narrow boundary layer by the oscillating wave orbital velocities. Since the shear velocity is dependent upon the intensity of turbulence and thus the total energy degradation rather than the net traction on individual sediment grains, the shear velocity is not changed by wave action. With the wave-induced turbulence confined to a narrow boundary layer and the waves propagating essentially without energy loss, the

effect of waves is to increase the traction on individual grains by increasing the mean velocity felt by the grains. Thus the mean velocity of flow must be increased, but the shear velocity must remain unchanged. The mean velocity of flow is increased by using the following equation developed by Bijker (1967) and modified by Swart (1974):

$$(v)_{\text{wave and current}} = (v)_{\text{current}} \left[ 1 + \frac{1}{2} \left( \xi_2 \frac{u_o}{v} \right)^2 \right]^{1/2} \quad (73)$$

where

$$\xi_2 = C_2 \left( \frac{fw_2}{2g} \right)^{1/2} \quad (74)$$

$$C_2 = 18 \log \left( \frac{10h}{D} \right) \quad (75)$$

$fw_2$  = Jonsson's (1966) friction factor with  $D$  as bed roughness

$u_o$  = wave orbital velocity

$$= \langle |u_{\text{orb}}| \rangle$$

Thus Equation 66 becomes

$$q = \frac{v}{1-p} D \left\{ \frac{v \left[ 1 + \frac{1}{2} \left( \xi_2 \frac{u_o}{v} \right)^2 \right]^{1/2}}{v_*} \right\}^{n_1} \frac{C}{A^{m_1}} (F - A)^{m_1} \quad (76)$$

with

$$F = \frac{\left\{ v \left[ 1 + \frac{1}{2} \left( \xi_2 \frac{u_o}{v} \right)^2 \right]^{1/2} \right\}^{1-n_1} v_*^{n_1} \left( \sqrt{32} \log \frac{10h}{D} \right)^{n_1-1}}{[g(s-1)D]^{1/2}} \quad (77)$$

Equations 76 and 77 are used for calculating sediment transport beyond the surf zone. In these equations,  $v$  is interpreted as the total velocity  $v_\ell$  due to currents  $=\sqrt{u_T^2 + v_T^2}$  and  $v_*$  is obtained from the relation

$$v_* = \sqrt{\frac{\tau_o}{\rho}} \approx \sqrt{\frac{g v_\ell^2}{C_z^2}} \quad (78)$$

where  $\tau_o$  is the bed shear stress and  $C_z$  is the Chezy coefficient. From  $q$ , the local transport rates  $q_x$  and  $q_y$  are obtained as before.

#### Transport in the vicinity of inlets

70. The flow and sediment transport in the vicinity of tidal inlets differ markedly from the flow and sediment transport in the surf zone for a straight open coast. The bathymetry in the inlet area is highly irregular with the presence of channels, bars, and shoals. The breaker line is generally shifted farther offshore and is irregular. Breaking and decay of waves and wave-induced currents are the major mechanisms for transport of sediment in the surf zone near straight coasts, with tidal currents being of secondary importance. Generally  $u_T$  is much less than  $v_T$ . In the vicinity of inlets, tidal currents are a major mechanism comparable to wave-induced currents. Moreover,  $u_T$  and  $v_T$  may be comparable. We are primarily interested in the transport and deposition of sediment in the navigation channel. There is no guidance in the open literature as to how sediment transport in this area should be handled. In view of the factors mentioned previously, the model uses the Ackers and White formulation modified for the presence of waves (Equations 76 and 77) in this area. From previous experience (Vemulakonda et al. 1985), this approach was found to yield satisfactory results.

#### Erosion and deposition

71. In the case of noncohesive sediments, once the transport rates of sediment  $q_x$  and  $q_y$  are known, changes in bed elevation can be determined from the continuity equation

$$\frac{\partial \zeta}{\partial t} + \frac{\partial q_x}{\partial x} + \frac{\partial q_y}{\partial y} = 0 \quad (79)$$

where  $\zeta$  is the bed elevation. Equation 79 indicates that if more material enters a cell than leaves it,  $\zeta$  will increase (there will be deposition), and if more material leaves than enters,  $\zeta$  will decrease (there will be erosion). Equation 79 is applied in a finite difference form to all the grid cells at the end of each time-step to determine erosion and deposition. Note that an increase in  $\zeta$  means a decrease in still-water depth  $h$  and vice versa. Therefore, the values of  $h$  are updated simultaneously.

## PART III: VERIFICATION AND BASE CONDITION TESTS

### Tides

72. Astronomical tides are the primary driving force for currents within St. Marys Inlet; they also contribute significantly to the ocean currents in the study area. WIFM is used to compute the currents for an average tide range in order to supply the sediment transport model with a time-series of depth-averaged horizontal velocity fields covering one tidal cycle (12.42 hr for the semidiurnal tide at Kings Bay).

#### Verification

73. Bathymetry. Most of the bathymetry and topography information used to define the grid cell elevations in Grid 1 (Figure 3) came from NOS nautical charts 11488, 11502, and 11503. Detailed soundings taken by the US Army Engineer District, Jacksonville (CESAJ), in June 1982 provided bathymetry for the navigation channels. All depths in the grid were referenced to mlw, and a datum difference of 3.0 ft between mlw and mean sea level (msl) was used. The maximum water depth in Grid 1 was 66 ft mlw.

74. Prototype data. The prototype tide data used to calibrate and verify WIFM in this study consisted of tidal elevations and currents. Figure 10 shows the locations of the tide and velocity gages deployed in the Kings Bay study area. Tide data were collected by the United States Geological Survey (USGS) and CEWES between September and December 1982. Currents were measured along ranges 1-4 (Figure 10) on 10 November 1982, and along ranges 5-7 on 12 November 1982. These surveys recorded approximately one tidal cycle. At each range, currents were measured at three stations: A, B, and C. At each station, velocities were measured at the surface, middepth, and close to the bottom. Only ranges 1-4 lay within the bounds of the computational grids, so ranges 5-7 were not used in this report. These current measurements were accurate and error-free, so they were used by WIFM in verification. The details of the prototype tide and current data collection effort are reported by Granat et al. (in preparation).

75. Plates 1-4 show the measured tides at Gages 1-4 of Figure 10 for November 1982. The mean long-term tide ranges, as given by the 1982 NOS Tide Tables, vary between 5.8 ft (St. Marys Entrance, north jetty) and 6.0 ft (Fernandina Beach, Amelia River). The measured tide data for the range survey

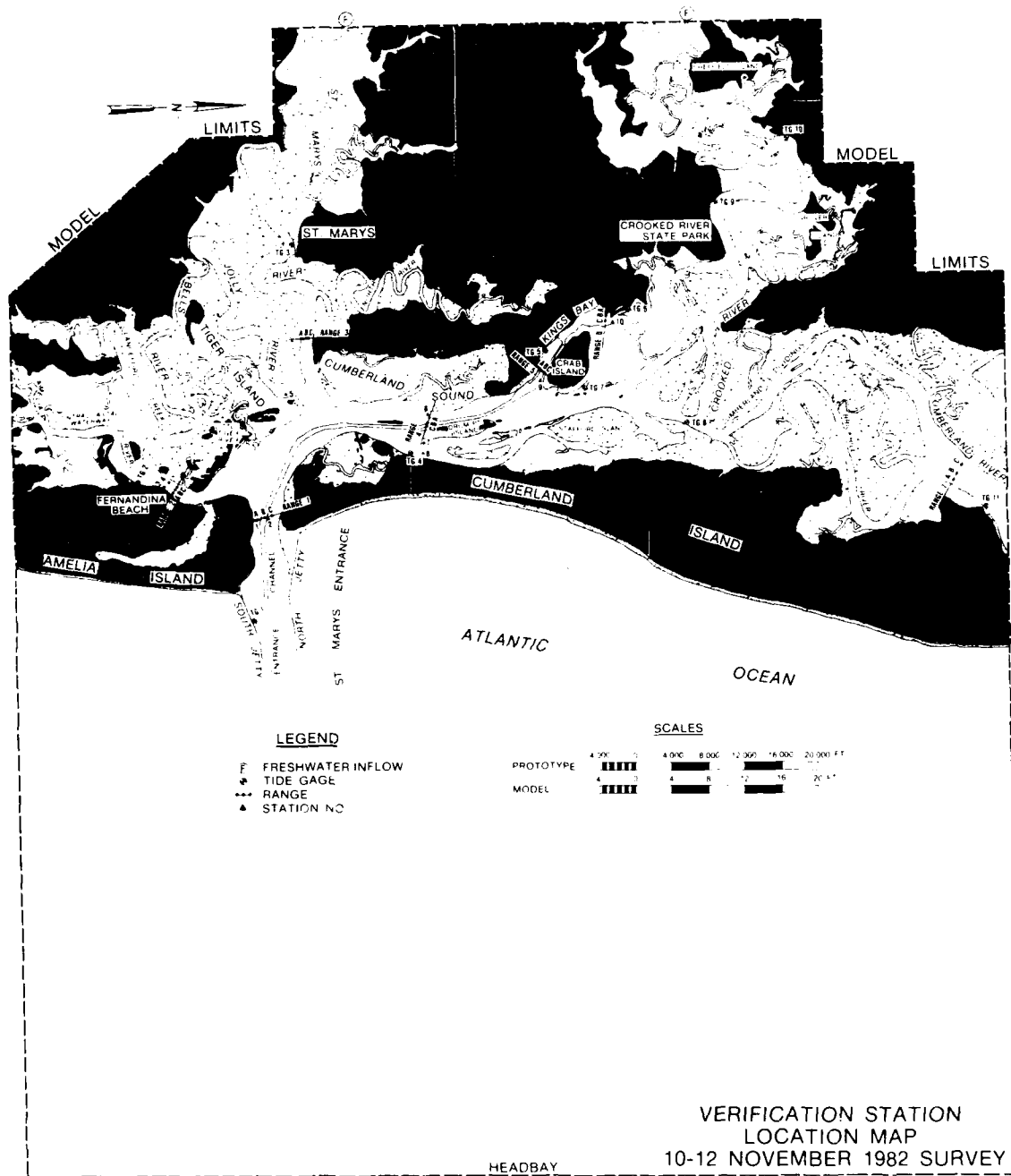


Figure 10. Locations of field gages

date of 10 November 1982 agreed with these mean ranges and so represented an average tide for the study area. Since the prototype tides measured on 10 November 1982 represented an average tide range, these tidal elevation signals were used as boundary conditions in WIFM. The prototype range current data were used to verify the velocity computations.

76. Plate 5 shows the prototype tide records for 10 November 1982. The sampling rate for the records was 5 min, and these data were spline filtered to remove high-frequency noise. Tides measured at Gages 2, 3, and 4 served as boundary conditions to the Amelia River, St. Marys River, and Cumberland Sound boundaries of the model. The signal from Gage 1, located at the south jetty of the inlet (Figure 10), was used as the boundary condition at the eastern edge of the computational grids. However, the travel time for a gravity wave between the eastern boundary and the actual location of Gage 1 is 25 min, so the boundary condition was phase shifted 25 min to account for this distance. The lateral ocean boundary conditions were interpolated between this offshore signal and the tide signal at the inlet (Gage 1). The boundary condition at St. Marys River (Gage 2) was also phase shifted 7 min to account for gravity wave travel time between the mouth of the river (the grid boundary) and the site of the prototype gage farther upstream.

77. The zero datum shown in Plate 5 represents the mean for each measured tide record rather than a geophysical datum such as the National Geodetic Vertical Datum (NGVD) of 1929. The elevations of the tide recorders used in this study were not referenced to a benchmark, so the relationships between the gage means are not known. The lack of a common datum caused numerous problems during calibration, since WIFM requires all elevations to be measured from a common datum. Since the tide gages were all fairly close to one another (less than 2 miles apart), even minor changes in elevations caused gradients great enough to change the flow patterns within the study area. These elevation adjustments were determined during the model calibration.

78. Permeability of jetties. Since both jetties at St. Marys Entrance are awash at high tide and known to be permeable, the tidal model has to properly simulate this effect on the velocity patterns. From field measurements taken by Florida Coastal Engineers in 1975, "it was estimated that up to 28 percent of the total [tidal] flood flow enters [the inlet] through the permeable jetties rather than at the ocean terminus of the structures." (Parchure 1982, p. 27). Since the widths of the jetties are small compared with grid

cell dimensions, they can be modeled in WIFM as flow barriers placed at grid cell faces. The hydrodynamics of flow over these barriers is computed by the broad-crested weir formula (Chow 1959). The parameters of barrier submergence (head across the weir) and Manning's  $n$  in the formula dictate the flow rate or "permeability" across a barrier in WIFM. The permeable jetties at St. Marys Entrance were therefore simulated with submerged barriers in the tidal current model.

79. An ad hoc method determined barrier "permeability" parameters for WIFM. Two initial assumptions were made to reduce the number of variables involved in parameter estimations. First, the crest of the submerged barriers used in WIFM was arbitrarily set to -4 ft msl. This depth ensured that the barriers would not become exposed during low tide. Second, it was assumed that the bottom friction in the study area, below -10 ft msl, could be approximated with a set Manning's  $n$  of 0.025. These assumptions reduce the variables affecting permeability to: (a) water velocity over the barrier, (b) water depth surrounding the barrier, and (c) the Manning's  $n$  of the barrier. The relationships between these variables were determined by a simple computational experiment.

80. A horizontal flume with length scales of the same magnitude as St. Marys Inlet was modeled by WIFM. The flume is 16,000 ft long and 2,400 ft wide, and it has a submerged barrier obstructing half the channel width at the center of the flume. Plate 6 illustrates the plan view of the layout, and the velocity pattern for a typical computation. WIFM was run for 128 different combinations of flow velocity (1, 2, 3, and 4 fps), water depth (10, 20, and 30 ft), and barrier Manning's  $n$  (varied from 0.025 to 0.050). Discharges per unit width were measured at the inflow and over the barrier for each run, and the permeability for the given conditions was computed as the percentage ratio of the latter to the former. It was determined that permeability was not a function of the flow velocity.

81. Figure 11 shows the family of curves plotted from this experiment. To set a desired permeability for a jetty barrier in the tidal current model, the water depth at the jetty section is noted, and the appropriate Manning's  $n$  is determined by interpolating between isobath curves in Figure 11. The Manning's  $n$  values needed to simulate a 28 percent jetty permeability were determined for each barrier segment in this fashion.

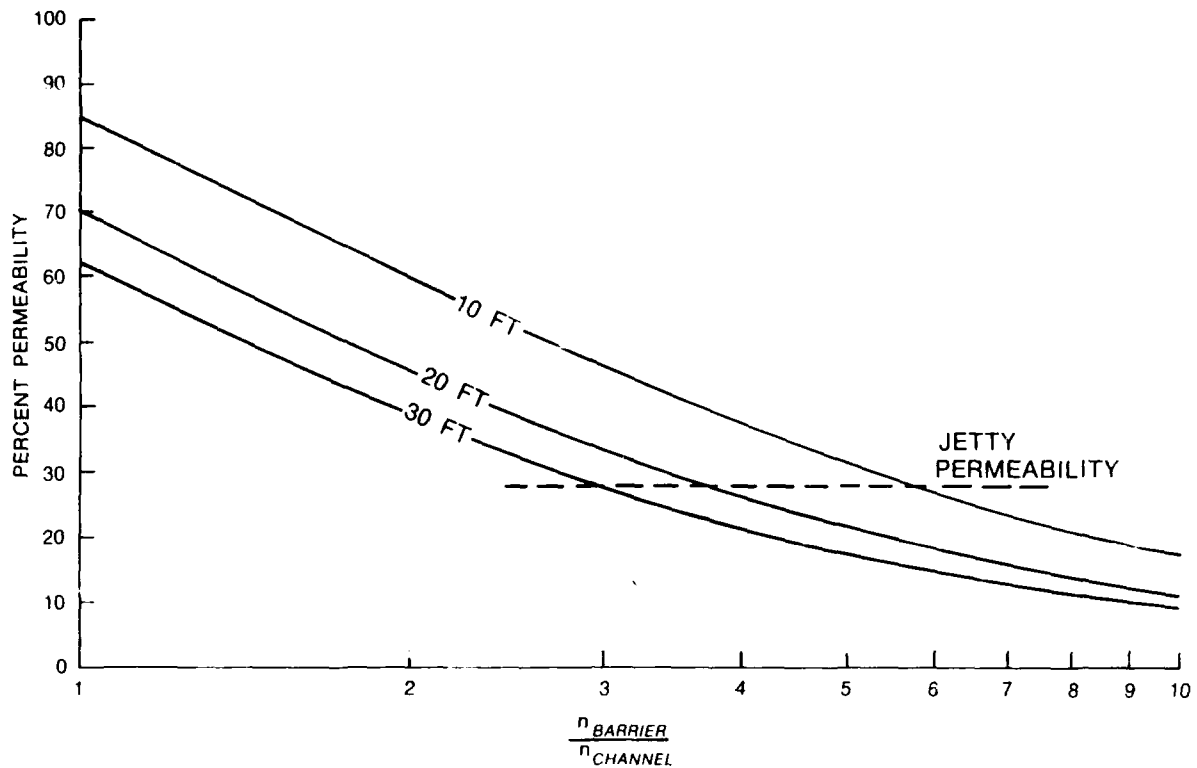


Figure 11. The relationship of barrier permeability to depth and Manning's  $n$

82. Calibration of the tidal model required the adjustment of WIFM boundary conditions until the computed elevations at tide Gage 1 matched the prototype data for 10 November 1982. The model was then verified for correctness by successfully reproducing the velocities measured at ranges 1, 3, and 4. The WIFM boundary conditions were adjusted during calibration by adjusting the datums for the prototype tide signals and accounting for the phase differences in the signals due to their placements in the grid as input conditions. All of the datum adjustments were less than 2 in. Note that WIFM used a time-step of 60 sec for all the computations.

83. Plate 7 shows where numerical gages were placed in Grids 1 and 2 in order to measure the computed velocities for the base and plane conditions in St. Marys Entrance. The gage sites in Plate 7 all correspond to either locations where prototype data were collected during the survey of 10 November 1982, or to important locations in the navigation channel. Table 1 equates the gage numbers in Plate 7 with the gage names used subsequently. The

missing numbers in the sequence correspond to gages outside the grid segment shown in Plate 7.

84. Plate 8 shows the match between the computed and prototype tide for 10 November 1982 at the four gage locations. The computed signals at Gages 2-4 are merely the prototype tide with the datum adjustments added, since these gages are boundary conditions in the model. Computations for tide Gage 1, in the inlet, match the prototype data.

85. Plates 9-13 compare the model computations of tidal currents to the prototype surface and middepth velocities at ranges 1, 3, and 4. (Solid curves represent numerical results and dashed curves prototype data.) Variations with time of both velocity magnitude and phase are shown over a tidal cycle. Since the numerical model is depth-averaged, in general its results would match the middepth measurements more closely. The agreement between the computations and the prototype data at the inlet (range 1) is excellent, both in magnitude and phase. The ability of the tidal current model to simulate the inlet velocities is crucial to the other aspects of this study, and the model performs this task well. In the case of ranges 3 and 4 (Plates 10-13) the numerical results represent the whole range. The computed and prototype velocities at range 4 (Cumberland Sound) also agree well. The velocity comparisons at range 3 (St. Marys River) agree in magnitude but differ slightly in phase. This phenomenon is probably due to the drainage characteristics of large marsh areas around St. Marys River which lie outside the boundaries of the tidal model.

86. Plates 14 and 15 show the computed velocity patterns in St. Marys Entrance for the peak flows of ebb and flood tide. The dashed portions of the barriers represent the permeable sections of the inlet jetties. The flow across the jetties can be seen on these Plates, and it appears that the flow is more pronounced across the south jetty.

87. In summary, the tide model used prototype gage elevation data for forcing boundary conditions. The measured tidal elevation at the south jetty of the inlet was reproduced in the numerical model. There was good agreement of numerical results with measured velocity data at range 1 in the inlet and satisfactory agreement at interior velocity ranges. Where the flows are influenced by other features in the region interior to the inlet, such as marshes which are not included in the tide model of Model B, close agreement is not expected. This lack of agreement should not cause concern since the

interior flows are studied by Model A and since the main purpose of Model B is to study coastal processes in the region mostly exterior to the inlet. Therefore, the calibration and verification of the tide model are complete and successful.

88. Since the channel bathymetry and geometry used in verification tests are close to existing (base) condition and the tide of 10 November 1982 is representative of the mean tide, the results of WIFM from verification tests were also taken to be those for base condition. They were used accordingly in the sediment transport model. The reader should note that the tidal conditions of 10 November 1982 were used in Model A also for base condition. The tide model generated a data file, consisting of tidal elevations and velocities, for each grid cell for each half hour of an approximated semi-diurnal period of 12.50 hr for later use in the sediment model.

#### Waves and Wave-Induced Currents

89. The hydrodynamic models RCPWAVE and CURRENT were extensively tested and compared with analytic solutions, laboratory data, and available field data during their development (Ebersole, Cialone, and Prater 1986 and Vemulakonda 1984). Considerable experience has been gained previously at WES in field application of these models (Vemulakonda et al. 1985). So reliance can be placed on the results of these models. The models do not require site-specific calibration. Because synoptic field data on waves and wave-induced currents were unavailable for the project area, no separate verification tests were performed for these models except indirectly through sediment model verification. The models were run for the base condition using the same bathymetry and channel geometry as in the tidal model. The results of the models were used in verification and base tests of the sediment transport model.

#### Wave climate

90. One of the primary objectives of the wave and wave-induced current model runs is to furnish input to the sediment transport model. In the case of the sediment transport model, the interest is in sediment transport and yearly shoaling rates in the navigation channel under an average year's wave climate, including normal storms but excluding extreme storms such as hurricanes and other tropical storms. So the wave climate for an average year at the project site was obtained from the WES Wave Information Study (WESWIS)

based on 20-year hindcast. This information was in the form of frequency of occurrence of waves in terms of predominant direction, significant wave height, and period bands in a depth of 60 ft mlw. Table 2 shows a sample of WESWIS data for St. Marys Inlet. The wave approach angle notation in this table is different from that used in the rest of this report. Angles in the table are measured with respect to the shoreline. Consider waves with an approach angle of 70.0 to 79.9 deg and significant wave heights in the band 0.0 to 0.49 m. They are distributed in period bands between 0.0 to 11.0 sec and greater. The total frequency of occurrence of these waves summed over all the period bands is 3.515 percent ( $3,515 \div 1,000$ ) or 0.03515. Similarly, WESWIS provides wave information in direction bands of 10 deg from 0 to 180 deg for all the wave height bands (0 to 5.00 m and greater).

91. In this study, these data were further consolidated into 79 different incident wave conditions (combinations of significant wave height, period, and direction) to run the wave and wave-induced current models. For convenience in running the sediment transport model, wave condition 80 was defined as a null wave condition when there was no significant wave activity. These combinations are listed in Table 3 which shows the percentage of occurrence of each condition. The directions represent angles in degrees measured from azimuth 87.5 deg (approximate shore normal direction). Negative angles signify waves coming from directions south of the normal; positive angles signify waves coming from directions north of the normal. The wave combinations shown in Table 3 are obtained from Table 2. Consider the example from Table 2 again. Since the wave approach angle is between 70.0 and 79.9 deg, the average value of 75.0 deg is taken. In terms of the notation of Table 3, the wave direction becomes -12.5 deg. Since the wave height band is from 0.0 to 0.49 m, the mean value of 0.25 m or 0.82 ft is taken for the significant wave height. As for period, on the basis of the distribution of Table 2, a mean period of 8.0 sec is taken. These are the values shown for wave 28 in Table 3.

#### Jetties

92. To account for diffraction of waves due to the two jetties of St. Marys Inlet, a special subroutine was developed. It used the diffraction solution of Penney and Price (1952). The wave model was first run without accounting for the presence of the jetties. The diffraction subroutine took the solution near the jetties as input and modified it to allow for

diffraction around the jetties. For this, the actual layout of the jetties is used. The procedure was somewhat similar to that of Perlin and Dean (1983). During the development of the subroutine and the procedure, several tests were performed including comparison of its results to the laboratory data of Hales (1980) for a single structure case, and to two physical hydraulic model tests conducted at CEWES for the two jetty case. In each case, the results of the subroutine compared favorably with laboratory data. In the grid for CURRENT, the jetties were represented in a stair-step fashion similar to that in WIFM. CURRENT treated them as thin-walled nonovertopping impermeable barriers.

93. Because of the highly variable nature of the computational grid, the wave model was run on a uniform grid with 500-ft by 500-ft cells, and its results were interpolated to the variable grid. The wave and wave-induced current models were run for each of the 79 wave conditions. There are no waves or wave-induced currents corresponding to wave 80. Each of the wave conditions represented the offshore boundary condition for the wave model. The model was run for the condition, and its results were stored in the form of wave height, direction, and wave number at each grid cell. They were next used as input to CURRENT which computed and stored on a file the setup  $\bar{\eta}$  and the two velocity components  $U$  and  $V$  for each grid cell for each wave. For convenience the corresponding wave information for each cell was also stored on the same file. Note that in general CURRENT used a time-step of 50 sec and in each run calculations were continued until an approximate steady-state condition was reached by the current field.

#### Results

94. For convenience, results for only three typical cases out of the 79 listed in Table 3 will be presented here. They have been selected so that they represent waves coming from south and north of the shore-normal direction and approximately along the shore-normal direction. It is convenient to present the results from the wave and wave-induced current models in terms of the uniform grid in the computational plane rather than the variable grid (Figure 3). One advantage of this type of display is that the results for the entire grid can be shown on an 8-1/2-in. by 11-in. sheet of paper. However, there is a disadvantage in that cell centers are not at the proper distances relative to each other. Thus, boundary cells appear much closer to the center than they really are. Moreover, the cell dimensions are distorted. Cells close to the inlet, the barrier islands, and the navigation channel appear to

be relatively larger; and as one moves away from this region (for example, closer to the lateral and offshore boundaries) the cells appear to be relatively smaller than they really are. In what follows, for convenience, the results will be shown on the uniform grid.

95. Figure 12 shows the region covered by the 50- by 73-cell uniform grid in the computational plane. The grid is 50 cells wide in the alongshore

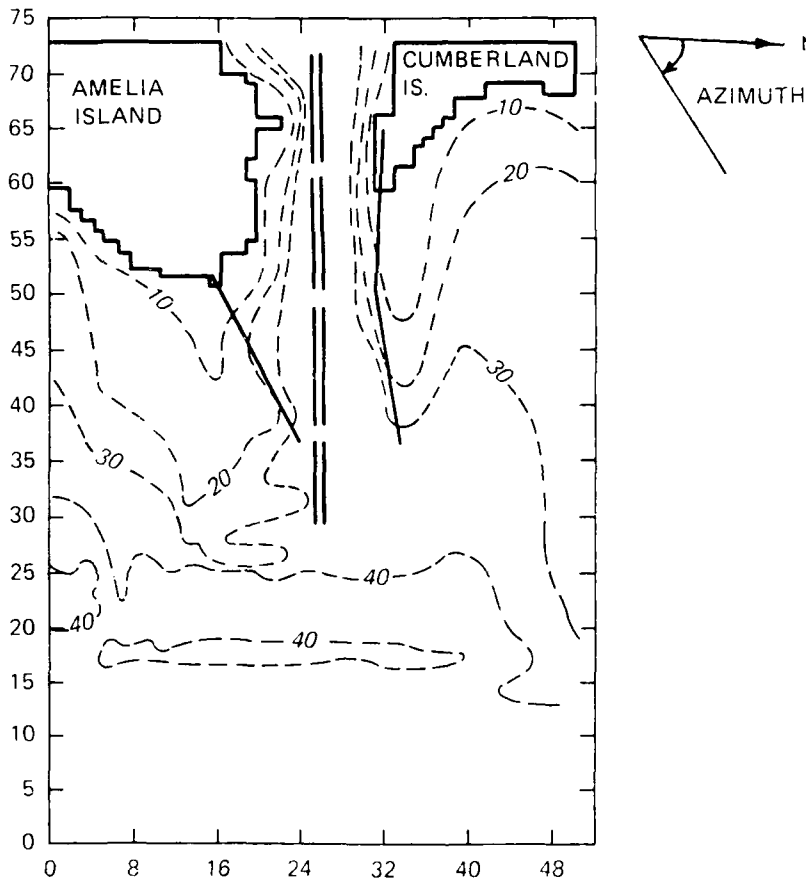


Figure 12. Uniform grid and bathymetry in computational plane

direction and 73 cells long in the onshore/offshore direction. The figure shows Amelia and Cumberland Islands, the navigation channel, the locations of the two jetties on St. Marys Inlet (the jetties are stair-stepped for the CURRENT model), and bathymetric contours with elevations referenced to msl (mlw plus 3 ft). The offshore boundary of the grid is at an approximate depth of 63 ft msl. Note the shoals offshore, south of the south jetty, and north of the north jetty. For convenience, these will be referred to hereafter as the offshore, south, and north shoals, respectively.

96. Figures 13, 15, and 17 display the results of the wave model, at cell centers, corresponding to waves coming from three different directions. These are waves 22, 45, and 59 from Table 3. These three conditions will be referred to as cases A, B, and C, respectively. For all three cases, the significant wave height in 63-ft depth of water msl is identical and equal to 7.4 ft. The period is roughly the same. The wave directions are quite different. In each of the figures, the length of an arrow (vector) is proportional to the wave height (a scale is shown), and the direction of the arrow indicates the direction in which the waves are progressing. For clarity, only vectors for alternate cells in each coordinate direction are plotted.

97. Figures 14, 16, and 18 present the wave-induced currents at grid cell centers corresponding to cases A, B, and C. In these figures, the length of an arrow is proportional to the magnitude of the current (a scale is shown), and the direction of the arrow indicates the direction of the current. The currents are depth-averaged. For convenience and clarity, only vectors in alternate cells in each coordinate direction are plotted.

98. Figure 13 corresponds to a wave of period 7.2 sec coming from azimuth 120 deg in 63-ft depth msl (Case A). The waves respond to the off-shore shoal. The wave height increases, and the wave direction changes as the waves go over the shoal. The wave height decreases, and the waves resume their original direction once the waves pass the shoal. The waves converge on the south shoal due to refraction, move parallel to the jetty, and break on the shoal. Because of the sheltering effect of the south jetty, very little of the incident wave energy goes past the jetty tips into the inlet. Note also the sheltering effect behind the north jetty resulting in very little wave action there. The waves converge on the north shoal, and the wave energy spreads out (diverges) due to a "bay" effect as the waves reach the shoreline of Cumberland Island. Near the approximately straight shorelines of both barrier islands, the wave height decreases because of wave breaking and decay.

99. Figure 14 shows the wave-induced currents corresponding to Case A. Near the straight part of the shorelines of Amelia and Cumberland Islands, the currents are mainly parallel to the shore and move to the north. However, near the south shoal, because of wave refraction and breaking, the currents tend to move in a westerly direction. The net result is the counterclockwise circulation we see over the shoal. The currents are the largest in this

Figure 13. Wave heights and directions for Case A,  
 $H = 7.4$  ft,  $T = 7.2$  sec,  
 Azimuth = 120 deg

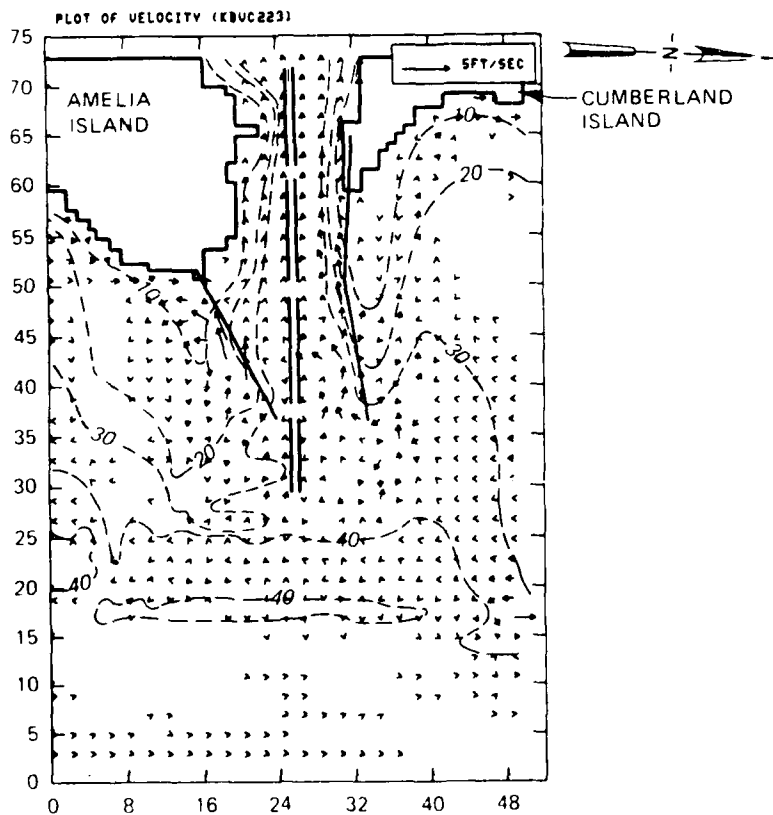
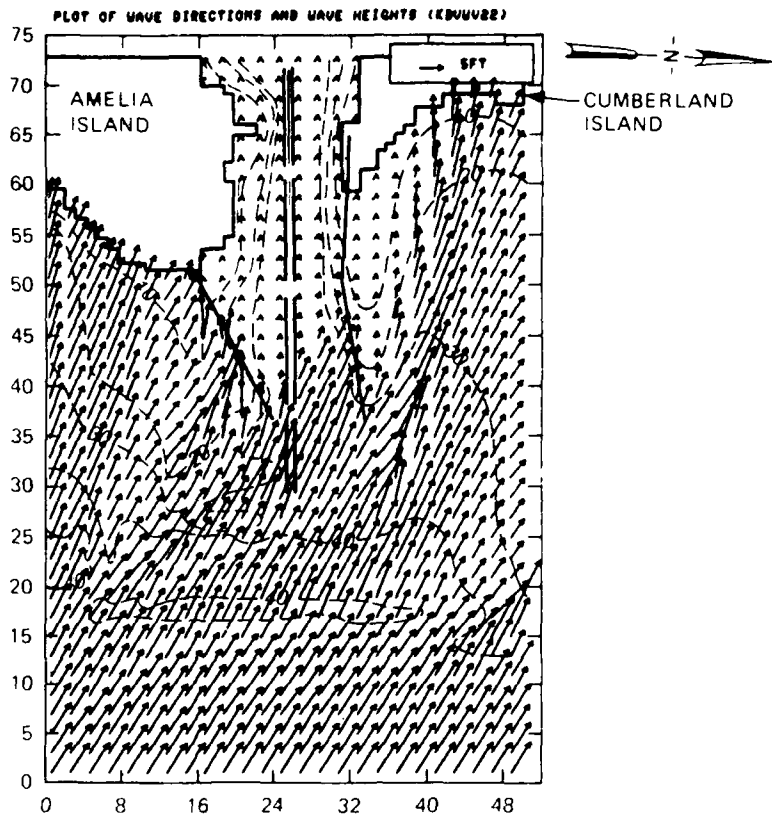


Figure 14. Wave-induced currents for Case A

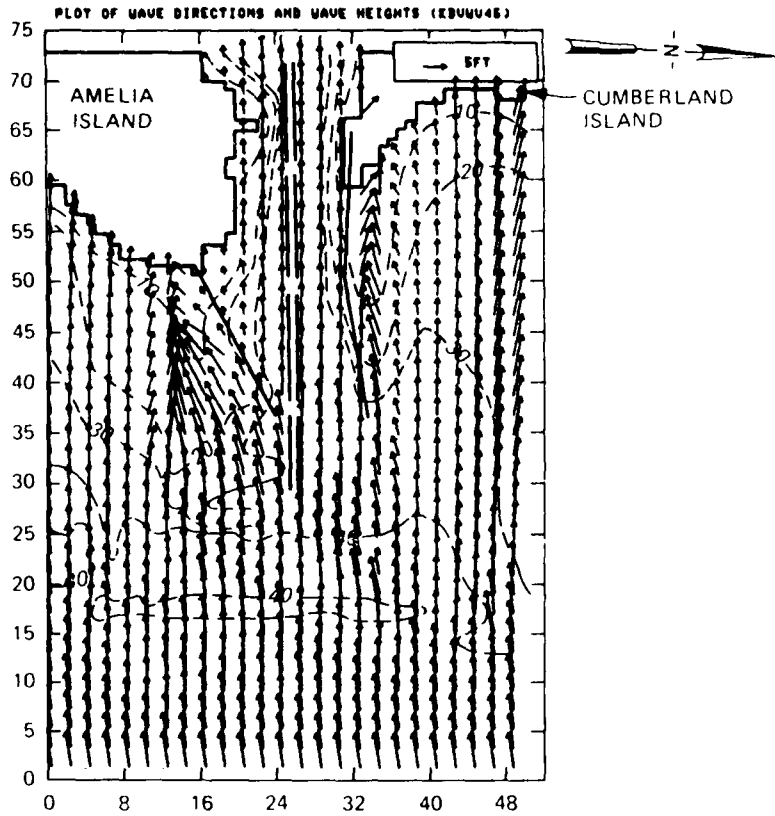


Figure 15. Wave heights and directions for Case B,  
 $H = 7.4$  ft,  $T = 7.8$  sec,  
 Azimuth = 80 deg

Figure 16. Wave-induced currents for Case B

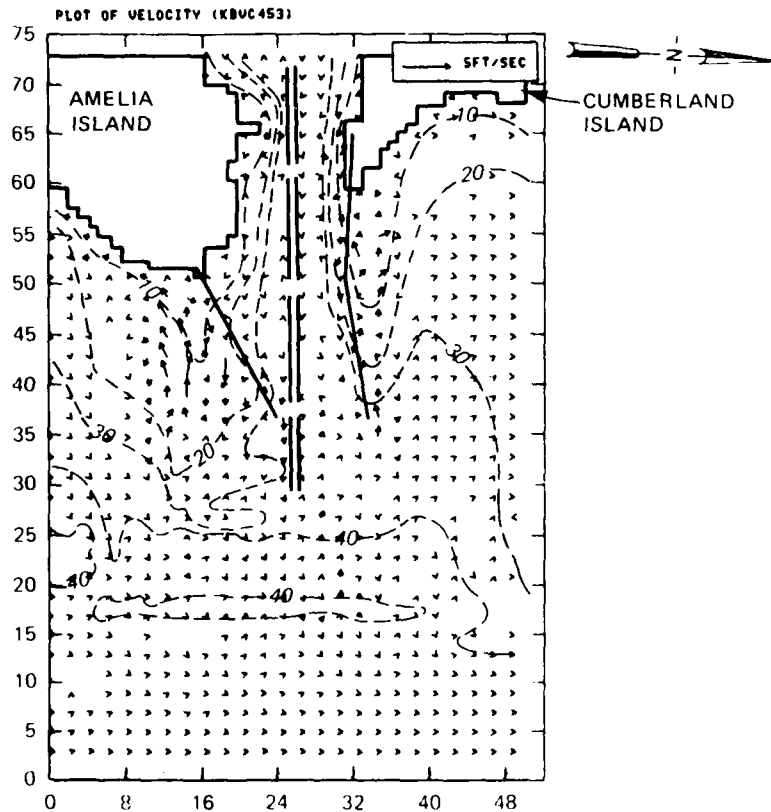


Figure 17. Wave heights and directions for Case C,  
 $H = 7.4$  ft,  $T = 6.9$  sec,  
 Azimuth = 60 deg

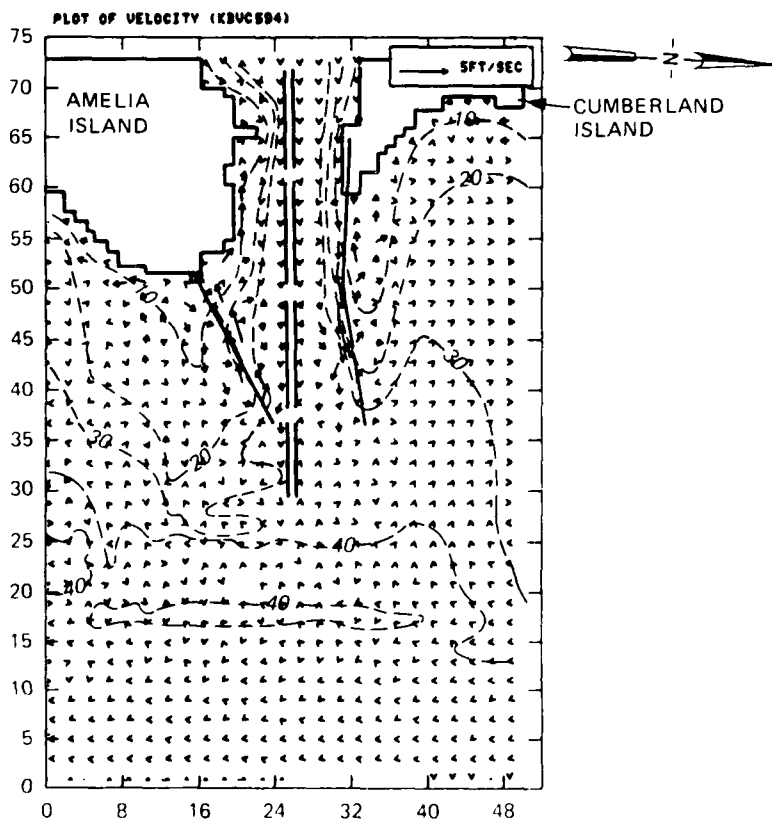
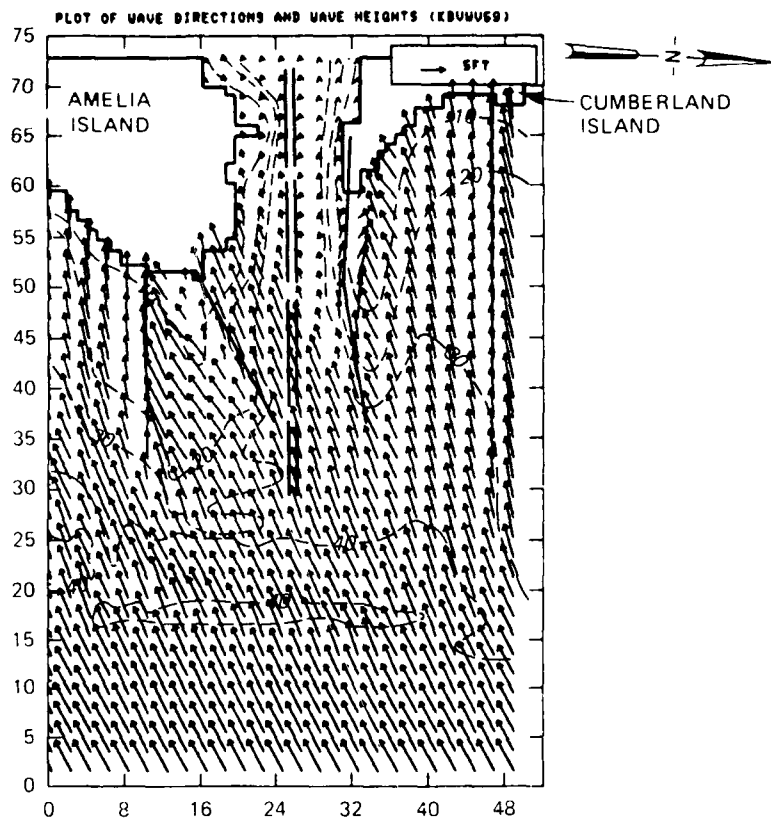


Figure 18. Wave-induced currents for Case C

region. Currents are strong on the inside of the north jetty because waves advance and break along the jetty. These currents have a westerly direction and advance into the inlet. Because of diffraction, currents are very weak behind the north jetty.

100. Figure 15 corresponds to a wave of period 7.8 sec coming from azimuth 80 deg in 63-ft depth of water msl (Case B). In this case, since the waves are approximately normal to the shoreline and the offshore contours, there is not much refraction of the waves offshore or even near the straight line portion of the shoreline. The waves converge on the south shoal, because of refraction, resulting in higher wave heights on the shoal. There is a similar convergence on the north shoal and a small divergence of wave energy near Cumberland Island. The incident wave direction is such that there is very little sheltering due to the two jetties. As a result the waves propagate straight and far into the inlet because the depth contours are approximately straight and parallel to the waves inside the jetties. The wave heights are large between the jetties.

101. Figure 16 displays the wave-induced currents for Case B. In this case, because the incident waves are approximately normal to the shoreline, there are no noticeable currents along the straight portions of the shoreline. Because of wave convergence and breaking, the currents are strong over the south shoal. A circulation pattern may be observed on the shoal. As the waves propagate straight and unchanged between the jetties without breaking or decaying, there are no noticeable wave-induced currents in this region. Currents may be observed on the north shoal because of wave convergence, breaking, and decay there. These currents are smaller than those observed on the south shoal.

102. Figure 17 corresponds to a wave of period 6.9 sec and azimuth 60 deg in 63-ft depth of water msl (Case C). The waves refract on the offshore shoal. They refract and converge strongly on the north and south shoals, resulting in higher wave heights on both shoals. Since the waves are aligned approximately parallel to the two jetties, there is very little sheltering due to the jetties so that the waves propagate deep into the area between the jetties. They break and decay near the straight portions of the shoreline.

103. Figure 18 represents the wave-induced currents for Case C. Near the straight reaches of the shoreline the currents are parallel to the shore

and in the southerly direction, as one would expect. The currents are strong over the north and south shoals because of wave breaking and decay. The pattern of the currents is complicated. Currents move in an easterly direction along the interior of the north jetty and westerly direction along the interior of the south jetty.

104. In summary, the overall results of the wave and wave-induced current models used for verification and base conditions are reasonable and behave in a manner one would expect, given the complicated bathymetry of St. Marys Inlet region and the two jetties on the inlet. The incident waves respond differently to the bathymetry, the shoals and the jetties, depending on their direction of incidence. The wave-induced currents depend on the bathymetry, the waves everywhere in the grid, and whether or not the waves break and decay in a given region of the grid.

### Sediment Transport

#### Verification tests

105. In order to make a strict verification of the sediment transport model, it is necessary to have either long-term (several years long) information on shoaling rates in the navigation channel and bathymetric changes in the general area or actual wave measurements made simultaneously with measurements on shoaling rates and bathymetric changes over a shorter time period (a few months). The latter type of data are not available for the project area. As for the former, examination surveys are available for the channel. As mentioned previously, the approach used by the sediment transport model does not account for extreme storms. So the prototype data selected should not include periods of such storms. As for dredging, it is possible to simulate dredging in the numerical model provided detailed information is available on the locations and durations of dredging and the amounts of material dredged at each location. Usually, such detailed information in terms of computational grid cells is not available from dredging records. Therefore the prototype data should not include periods of dredging. In the case of St. Marys Inlet, the navigation channel was deepened to the existing condition (40-ft project depth) in 1978 and 1979 so only 5 to 6 years of prototype data are available. The channel still has not stabilized after the deepening. Sediment transport and other processes continue to be in a state of transition. Out of the

available information on examination surveys for the navigation channel, we were able to locate only one set of examination surveys covering a period of approximately 1 year (1980 through 1981) which was free from the effects of dredging and severe storms. The duration of this data set is too short for the data set to be used for strict verification of Model B results which are based on 20-year hindcast wave data. Therefore, a strict verification of Model B results with the data set is not possible. Instead, the average yearly erosion/deposition rates along the channel obtained from the data set will be compared with Model B results to see if the numerical model results are reasonable and agree with the trends and shoaling magnitudes exhibited by the field data.

106. Prototype data. The field data set consisted of seven examination surveys conducted by CESAJ during 1980 and 1981 between sta -80+00 and sta 325+00 (Figure 19). For convenience, this pre-1985 CESAJ stationing will be used throughout this report. The locations and dates of the surveys are

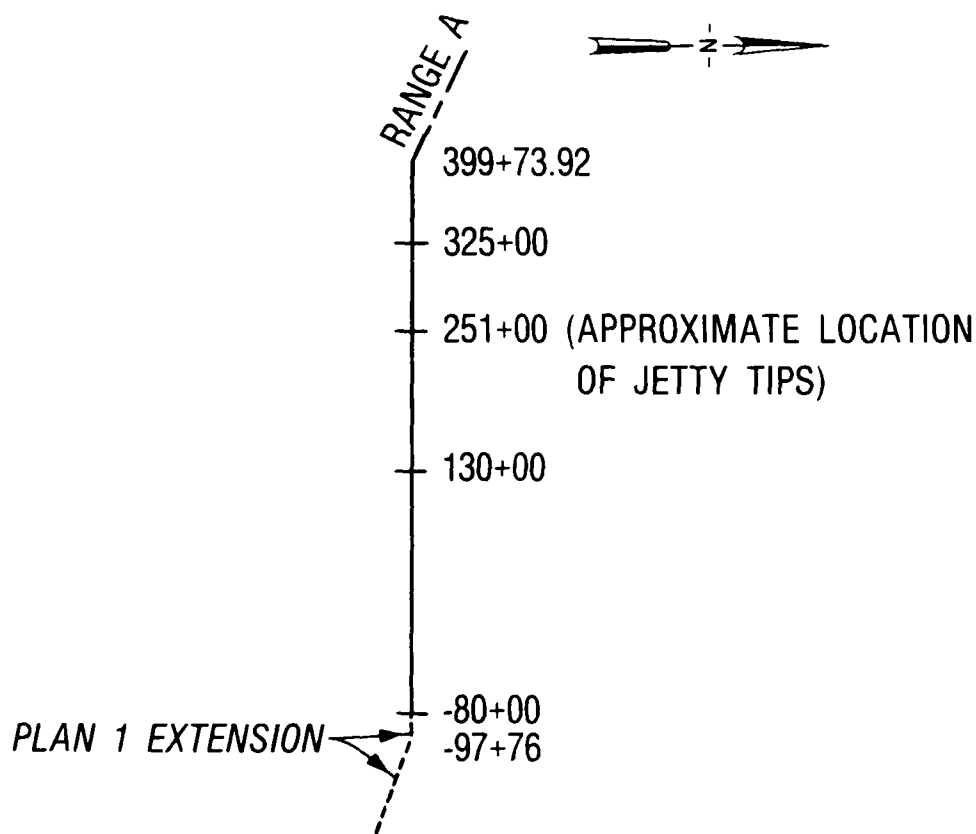


Figure 19. Pre-1985 CESAJ stationing

shown in Table 4. On the basis of several tests, it was determined the datum used in survey 2 was in error by 0.5 ft. This is not surprising since the reach of channel surveyed was far away from the tide gages used to locate the datum. The datum for this survey was adjusted accordingly.

107. The field data were examined in two ways. First, surveys 1, 2, and 7 were used to determine average yearly erosion/deposition rates. At each of the 35 locations along the channel corresponding to computational grid cell centers, depths across the width of the channel were averaged, and the erosion/deposition rates were computed and extrapolated to feet/year values. (Following a similar procedure, but computing the average depth for each cell from 16 spatially distributed points in the cell, yielded results that were close to the results obtained from averaging the cross-section depths). Next, the total period was broken down into three separate periods of approximately 4, 2, and 6 months, based on the survey dates. At each of the 35 locations, the erosion/deposition rates obtained for these periods were converted to feet/year values, and the extreme values at each location were determined. Figure 20 is a plot of the average and extreme values from the prototype data

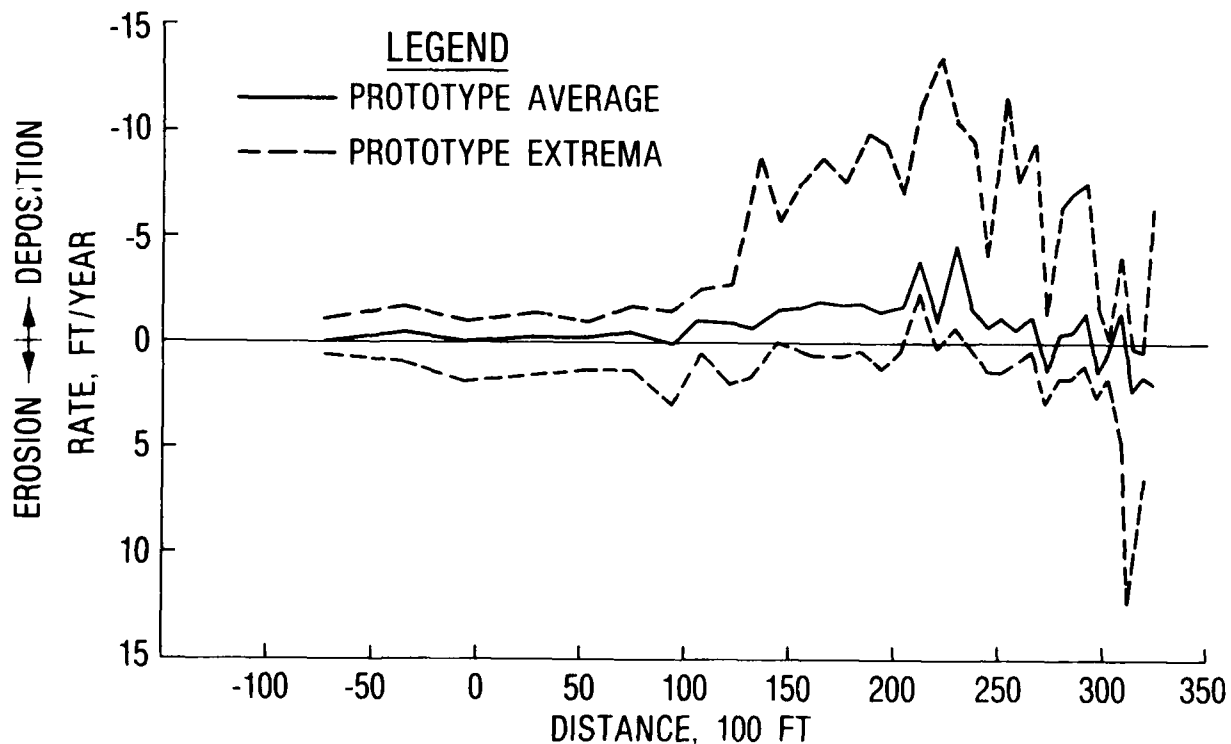


Figure 20. Prototype data on erosion/deposition rates

at different stations along the channel. The sign convention that erosion rates are positive and deposition rates are negative is used hereafter.

108. Testing procedure. At the start, the sediment model used the bathymetric information from field surveys 1 and 2 for the channel. Outside the channel, the bathymetry used was identical to that used by the tide, wave, and wave-induced current models for base condition since better detailed information was not available.

109. To generate a wave sequence for 1 year for the verification and base tests of the sediment model from the waves given in Table 3, the following procedure was used. Each wave event in the sequence was assumed to be steady with a duration of 4 hr. This is a reasonable assumption from field experience and measurements, provided extreme storms are ruled out as done here. Each wave condition (1 to 80) of Table 3 was identified with a frequency of occurrence. During the running of the sediment model, wave conditions were selected such that each of the 80 conditions occurred at the frequency shown in Table 2. Thus, the waves used by the sediment model reflected nature in terms of wave statistics provided by WESWIS. The same waves were used for base and Plan 1 tests.

110. The sediment model used a time-step of 1 hr. This value was considered optimum on the basis of testing and previous experience. The computational sequence employed by the sediment model consisted of the following steps:

- a. Read in the local bathymetry.
- b. Pick the first wave condition.
- c. Read in the corresponding wave information (wave height, angle, period, wave-induced velocities, and setups/setdowns).
- d. Read in the first hour of the tide data (tidal velocities and elevations).
- e. Combine the above quantities to obtain a total velocity field, wave field, and local depth.
- f. Compute sediment transport quantities and the associated erosion and deposition rates.
- g. Repeat steps d, e, and f at 1-hr intervals for a total of 4 hr.
- h. Pick the next wave condition and continue steps c through g, etc.

As indicated previously, the local still-water depth  $h$  for each cell was updated at each time-step based on the erosion or deposition in the cell. The

total local depth, which is the sum of  $h$ ,  $\eta$ , and  $\bar{\eta}$ , was also updated. The total velocity components  $u_T$  and  $v_T$  were adjusted on the basis of simple continuity to account for the change in bed elevation of the cell. It was observed from running the sediment transport model that model results in terms of erosion/deposition rates (ft/year) along the channel became approximately constant after the model was run for 150 to 180 prototype days. There were minor variations from run to run as the total time was increased, but the trends and magnitudes stabilized. Therefore, the above sequence was performed for 180 instead of 365 prototype days to compare with field data for verification.

111. Results. Based on the trends exhibited by the prototype data, the reach of the channel between sta -80+00 and sta 325+00 was divided into seven zones for verification (Figure 21). A similar approach was used for Model A verification. Four to six computational grid cells were in each zone. The value assigned to a zone is the average of the values for the cells in the zone. A comparison of the prototype average erosion/deposition rates with results of Model B is shown by zones in Figure 22. Also shown in the figure are prototype extrema based on 1 year of prototype data. Model B results show the same trends as the prototype average results and are in approximate quantitative agreement in zones 1-4 (between sta -80+00 and sta 241+56). It is not surprising that they do not match quite as well between sta 241+56 and sta 325+00. This is a highly dynamic region, especially outside the jetty tips (sta 251+00) and is very much dependent on the actual (rather than average) wave climate that existed between surveys. This can be seen in the large spread between prototype extrema. There is movement of material from the off-shore bar and shoals into the channel. As was pointed out previously, prototype data of 1 year's duration are not necessarily representative of a 20-year average. On the whole, Model B results are reasonable and in agreement with field data.

#### Base tests

112. The only difference in the bathymetries used at the start of verification and base tests was in the navigation channel. The sediment model used the channel bathymetry from the CESAJ survey of June 1982 for the base tests because the same bathymetry was used in all the other models for base condition.

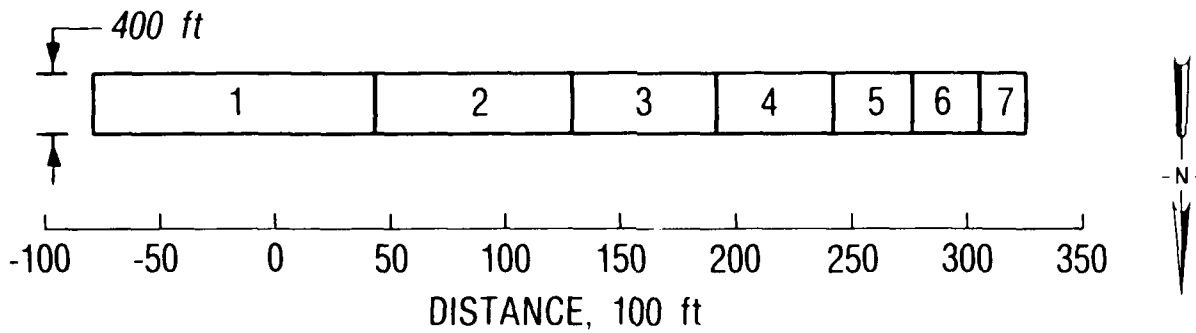


Figure 21. Zone numbers assigned to channel reaches for verification tests

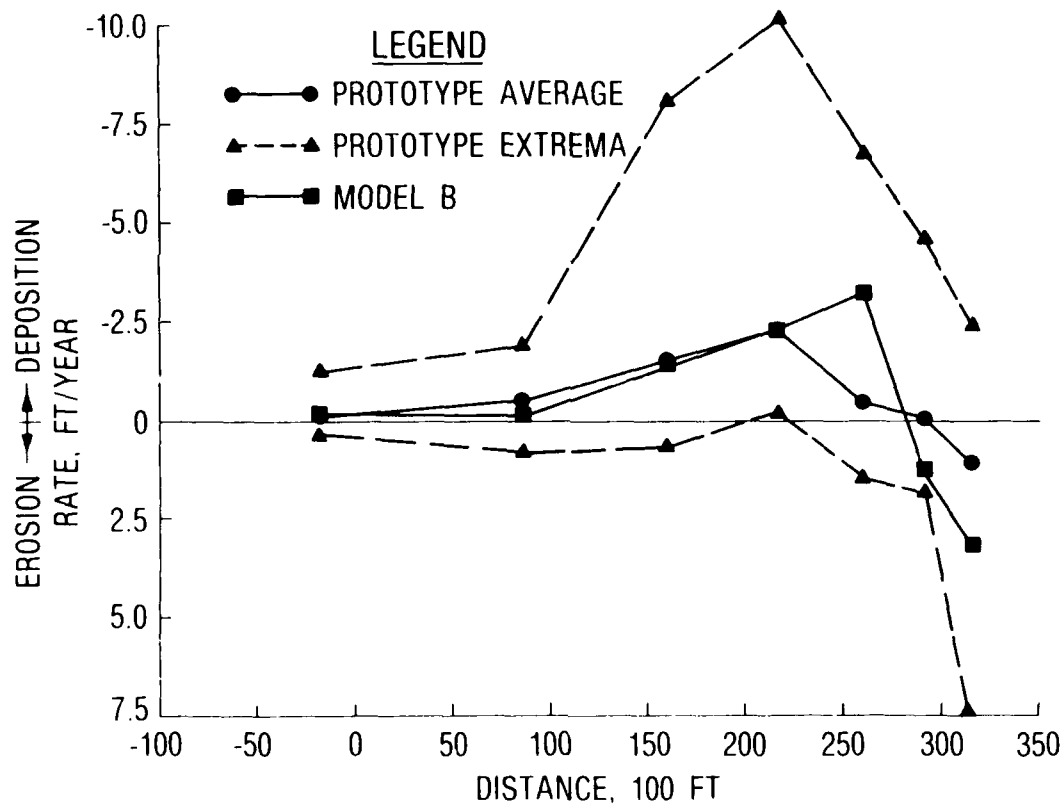


Figure 22. Comparison of prototype data with Model B results for verification

113. At the time Model B computations were made, up-to-date field survey information was not available on channel bathymetry between sta 325+00 and sta 399+74, nor was up-to-date bathymetric information available for areas on either side of the channel. Model B used the best available information, which usually was CESAJ construction dredging survey information and the bathymetric information from NOS charts. Unfortunately, this information does not seem to represent the current bathymetry for the reach of the channel between sta 325+00 and sta 399+74 and the areas of either side of the channel in this reach, according to the latest CESAJ surveys. These surveys seem to indicate that the depths may be greater (by 5 ft or more) in this reach. For this reach of the channel, the information available to us at the time of computations indicated the depths were greater than the existing project depth of 40 ft and that the channel seemed to be in a state of erosion; therefore it did not require maintenance dredging. There was no quantitative information available on erosion/deposition rates for this reach.

114. The sediment transport model followed the same testing procedure as it did for verification. The model was run for 200 prototype days, and its results were converted to channel erosion/deposition rates (ft/year). For base tests, the entire length of channel offshore of sta 399+74 was considered. The channel was divided into ten zones (zones 1 to 10 in Figure 23). Figure 24 shows the erosion/deposition rates by zone for base. When the results for verification and base are compared (Figures 22 and 25), it is observed that there is similarity in the trends and magnitudes. This is not surprising since the channel bathymetry in the two cases is not that much

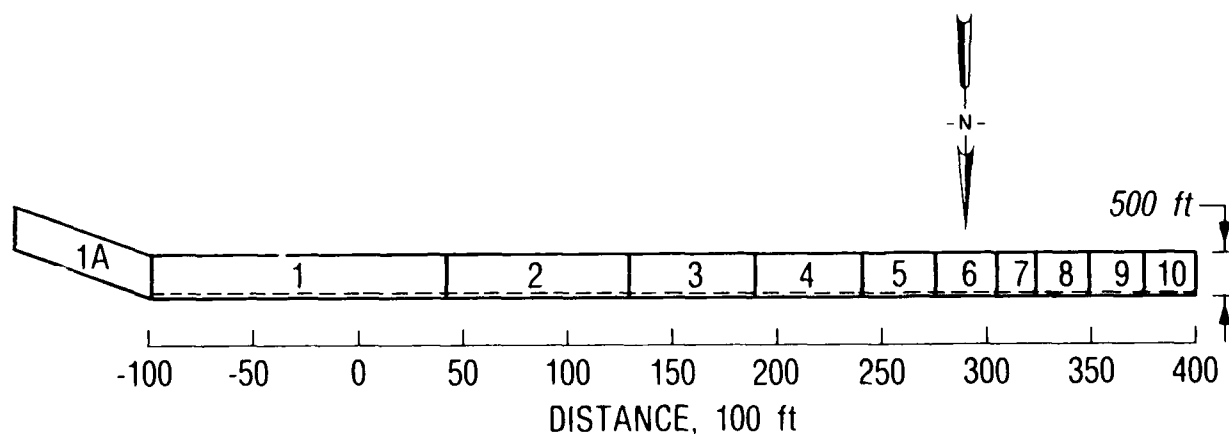


Figure 23. Zone numbers assigned to channel reaches for base and Plan 1 results

different inside the jetties and the forcing functions (tides, waves, and wave-induced currents) are the same for both cases. In both cases, there is deposition outside the jetty tips (sta 251+00). It changes to erosion interior to the jetty tips because of circulation due to wave-induced currents. The heaviest deposition rates are observed near the jetty tips. This is the area where the channel cuts through the offshore bar and material from the bar tends to move into the channel and deposit there.

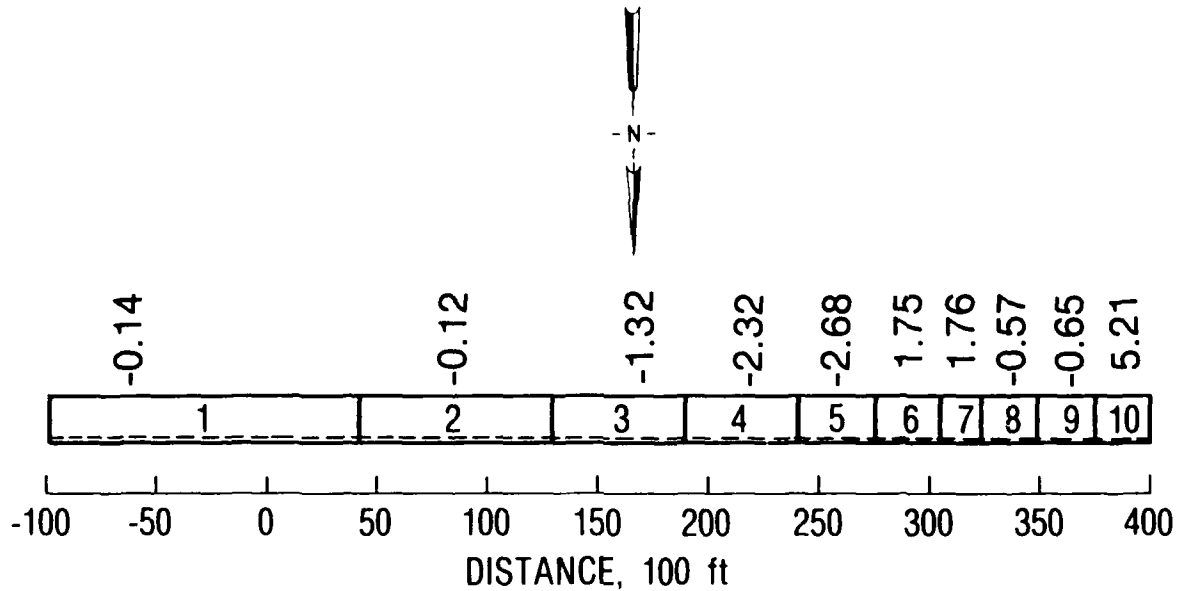


Figure 24. Erosion/deposition rates (ft/year) for base condition from Model B (+ = erosion, - = deposition)

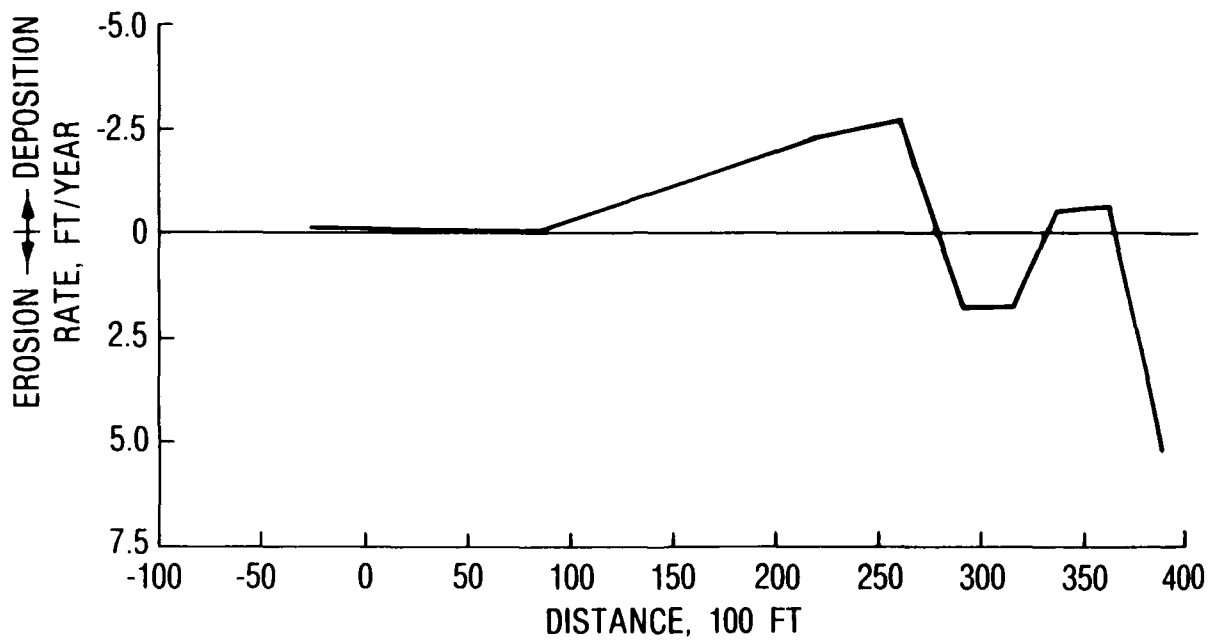


Figure 25. Erosion/deposition rates for base

## PART IV: PLAN CONDITION TESTS

### Plan 1

115. Model B tested only one plan condition which will be referred to hereafter as "Plan 1." The plan is to (a) widen the navigation channel to 500 ft, with the widening taking place on the north side of the present entrance and offshore channels; (b) extend the channel on the ocean side, with the extension being at an angle 20 deg south of the present channel center line at sta -97+76 approximately; and (c) deepen the channel to -49 ft mlw (46-ft project depth plus 3-ft advance maintenance). The channel is to have a trapezoidal cross section with side slopes of 3H:1V. Figure 26 shows details of the planned channel layout and cross section. As requested by the Officer In Charge of Construction (OICC), TRIDENT, the plan tested assumes also that the landward 1,000 ft of the south jetty will be made sand-tight simultaneously.

116. In view of the urgent need expressed by OICC for Plan 1 results from Model B for design of the entrance and offshore channels, the wave and wave-induced current models were not rerun for the Plan 1 condition as originally planned. Running the models again would have delayed the results considerably. Moreover, since the changes from base to Plan 1 condition of the navigation channel were reflected mainly in the cell size and bathymetry for one row of cells in the computational grid, it was felt the effect of channel modification on waves and wave-induced currents would be minor compared to its effect on tides and sediment transport.

### Computational Grid

117. As indicated previously in Part II, the computational grid for Plan 1 (Grid 2) retained the major features (overall dimensions, orientation, number of cells, etc.) of the grid for base (Grid 1). The only difference between the two grids lies in the mapping of the row of cells corresponding to the navigation channel. These cells were made 500 ft wide by minor adjustments of the cells on either side. In view of the rectilinear nature of the grid, the navigation channel was represented in a stair-step fashion where it turned south. It was assumed that dredging for the navigation channel

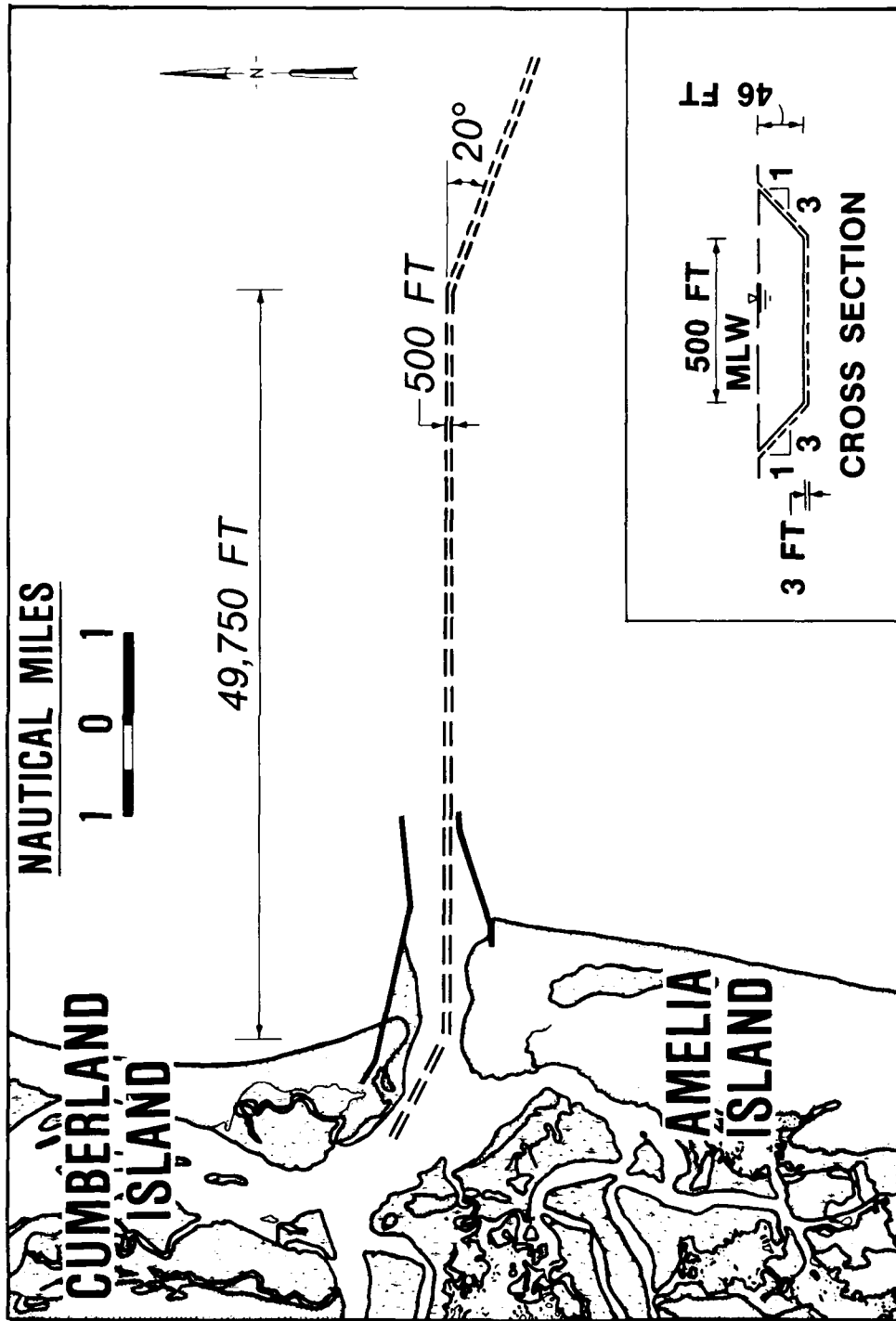


Figure 26. Details of Plan 1 channel

extension stopped wherever the natural ocean depth became equal to or greater than 49 ft mlw. (This location of the oceanward entrance of the navigation channel would be determined in the field from the latest bathymetric surveys for the final channel design.) In the navigation channel itself, the planned channel depths were used. The bathymetry used outside the channel was the same as that for base condition.

### Tides

118. To properly model the sand-tightened section of the south jetty in the numerical model, the crests of the barriers simulating this jetty section were raised to the prototype jetty elevation of +3 ft msl; and the Manning's  $n$  values governing flows over the barriers were changed appropriately.

119. Plates 16-19 compare the computed base and Plan 1 velocities (magnitudes and phases) at seven sites in the inlet (refer to Table 1 and Plate 7 for locations of these sites). All of the changes in tidal currents are due to sand-tightening of the south jetty. The peak velocity at tide Gage 1 (Plate 16) has increased by approximately 10 percent between base and Plan 1 due to sealing of a section of the south jetty. The gages at the throat of the inlet (Endeco velocity Gage 2, range survey Gages 1-A, 1-B, and 1-C, and Fort Clinch) (Plates 16-19) show negligible change in velocity. The velocity at the ocean end of jetties (Plate 18) increases by about 10 percent in both ebb and flood for Plan 1 and shows a slight phase shift.

120. Plates 20-21 show the tidal current patterns near the inlet for maximum ebb and flood for Plan 1. For clarity, the plotting of velocities below 0.1 fps is suppressed in these figures. These two plates can be compared to the base condition patterns of Plates 14-15, but few differences are apparent in a visual examination. For convenience the vector differences between Plan 1 and base condition velocities are shown in Plates 22-23 for the same region near the inlet, for maximum ebb and flood, respectively. Note the change in velocity scale. The plotting of velocity differences below 0.05 fps is suppressed in these figures. Both figures indicate that sealing the south jetty exerts local changes on tidal currents. The large difference vectors at the landward end of the south jetty represent a decrease in velocities between base and Plan 1 since flows in this area are stopped by sealing the jetty. No other significant changes in the current patterns were noted within the study

area for Plan 1. The extension of the navigation channel at the seaward end produced almost no effect upon the current patterns.

### Sediment Transport

#### Testing procedure

121. The testing procedure used was similar to that for base conditions except the computations were performed with Grid 2, and the bathymetry at the start of computations corresponded to Plan 1 conditions. The sediment transport model used the results of the tide model for Plan 1 and the results of the wave and wave-induced current models for base conditions. As for the base test, computations were performed for 200 days of prototype time, and the results were used to estimate yearly erosion/deposition rates along the channel.

#### Results

122. The channel was divided into 11 zones for Plan 1 (Figure 23). The exact offshore limit of zone 1A was yet to be determined from field surveys. Figure 27 shows the erosion/deposition rates by zone for Plan 1. A comparison of base and Plan 1 results is plotted in Figure 28. The model predicts an increase in both deposition rates and erosion rates between sta -97+76 and sta 325+00 from base to Plan 1. Zone 1A is not shown in the figure. This zone indicates on the average a slight erosional tendency with rates of the order of 0.1 ft/ year or less. The model predicts deposition in zones 8 and 9 (sta 323+02 to sta 374+94) for both base and Plan 1. For Plan 1, the deposition rates are of the order of 1.0 to 1.4 ft/year. Model B predicts large erosion rates in zone 10 (sta 374+94 to sta 399+74). Since there is no quantitative field information on sedimentation rates in zones 8-10, it is difficult to comment on Model B predictions for this reach. It is suspected that since the bathymetric information used for this channel reach and adjacent areas was not up-to-date, it might have caused deviation of Model B results from field experience. Another contributory factor might be the grain sizes found in this reach, which are much larger than elsewhere in the study area. The model assumes the same grain size distribution throughout the study area. The local deviation of grain sizes might have resulted in the prediction of larger erosion and deposition rates locally. There is reason to believe the effect of these factors is restricted to Model B predictions for zones 8-10

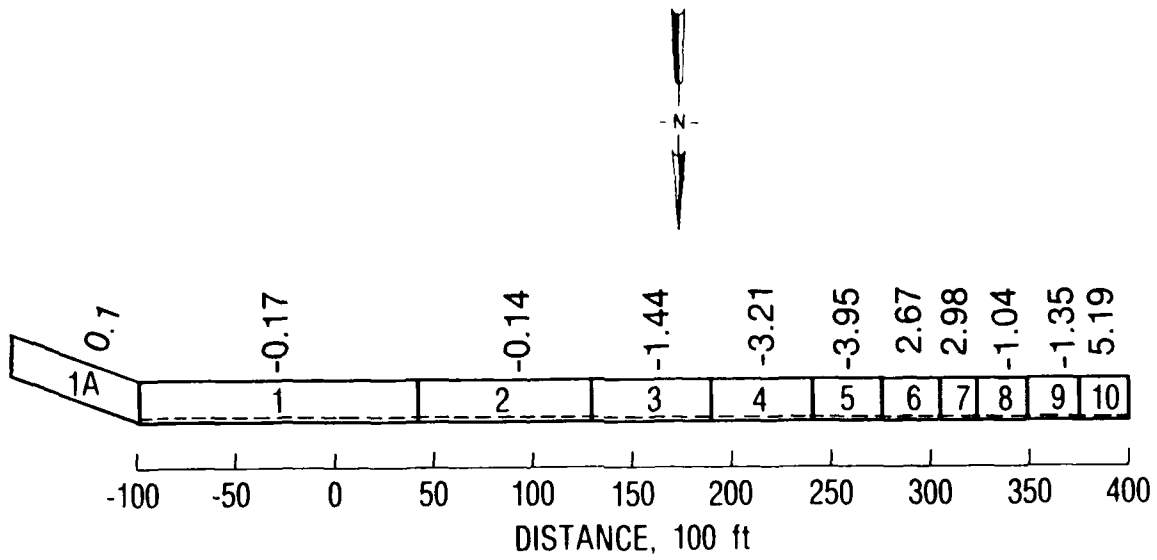


Figure 27. Erosion/deposition rates (ft/year) for Plan 1 condition from Model B (+ = erosion, - = deposition)

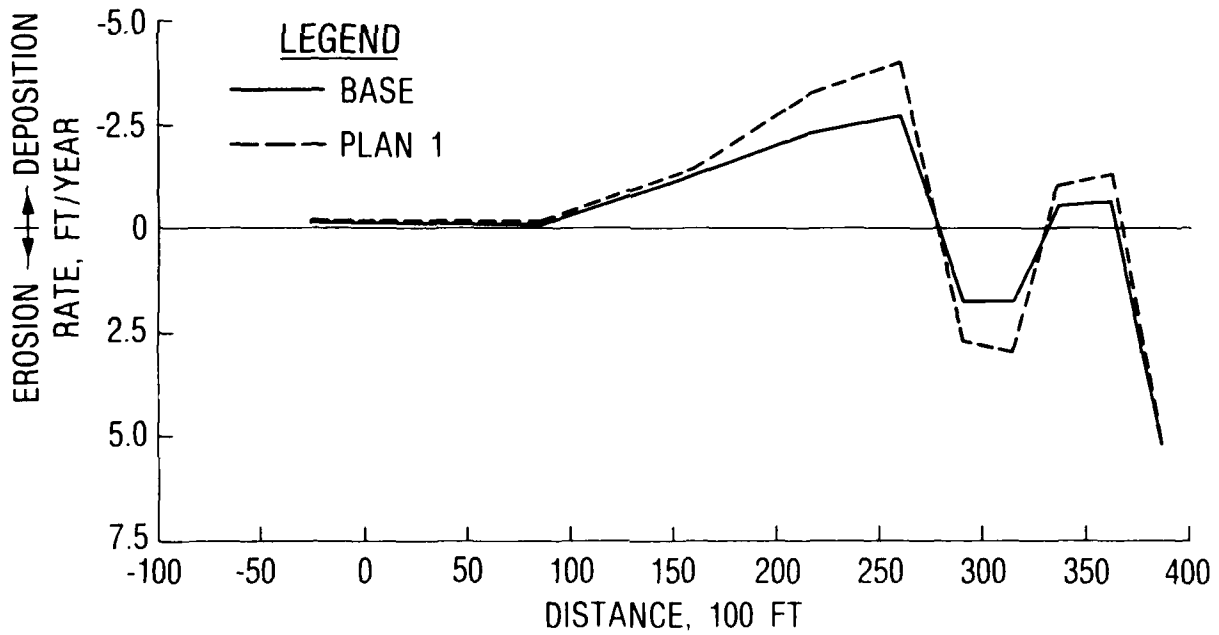


Figure 28. Comparison by zones of erosion/deposition rates for base and Plan 1

and does not extend to the model results for the rest of the study area.

123. In terms of yearly shoaling volumes, if the reach of channel from sta -80+00 to sta 325+00 is considered, the results translate to approximately 475,000 cu yd/year for base and 788,000 cu yd/year for Plan 1 allowing for the wider Plan 1 channel, or an increase of approximately 66 percent from base to Plan 1. The base volume is of the same order as the maintenance dredging volumes recorded in CESAJ dredging logs.

## PART V: MODELING LIMITATIONS

124. The numerical models used in this study were the most advanced models available at the time the study was undertaken. However, they do have certain limitations which must be kept in mind in order to view the results obtained from this study in proper perspective. As previously indicated, numerical models represent an approximation to the physical processes. The degree of approximation depends on the physics in the formulation of the individual models, the resolution of the computational grid, and the time-step used in computation. The assumptions made in the models and the limitations of the models have been given previously along with the description of the models in Part II. In this study, the computational grid resolution and the computational time-steps used have been chosen, on the basis of experience and testing, such that the results obtained would be reasonably accurate for engineering purposes and, yet, the computational costs would not be prohibitive.

125. Generally, the hydrodynamic models are more exact than the sediment transport model because more insight into the hydrodynamics is available and more experience has been gained in modeling the hydrodynamics numerically. With proper calibration and verification, tidal hydrodynamic models such as WIFM can predict tidal elevations very accurately and tidal currents fairly accurately. Monochromatic wave models such as RCPWAVE are fairly accurate in open coast areas. Their results near structures and inlets are more approximate because of the difficulties and expense in modeling diffraction near structures and wave/current interaction near inlets. As for wave-induced current models such as CURRENT, people have less experience with them than with tidal and wave models. Wave-induced current models are reasonably validated for open-coast situations. Their results are more approximate near inlets and jetties because the hydrodynamic processes are more complicated and less understood, the wave fields are less accurately known, and there is a lack of field data to validate the models.

126. Sediment transport is the most important aspect of the project for project design; yet the sediment transport model is the least exact of all the models, and the uncertainty is the greatest with this model. The uncertainty exists because sediment transport in general involves complex interactions between the bed and the flow which are not well understood. Of all types of sediment transport, sediment transport near inlets under the combined action

of waves and currents, as typified by this study, is one of the most complicated and least understood processes. The sediment transport model employed in this study uses fairly simple empirical formulas which are based on laboratory and field data. It reflects the inaccuracies inherent in the formulas as well as the inaccuracies in the results of the three numerical hydrodynamic models.

127. In this study, a mean tide, and an average year's wave climate based on 20-year averaging of wave statistics were used in running the sediment transport model to estimate the yearly shoaling rates in the navigation channel. In reality, the tidal cycle is more complex, involving spring and neap tides; and the wave climate varies from day to day, season to season, and year to year. Severe storms such as hurricanes, which have a dramatic impact on sediment transport and channel shoaling, have been excluded from this study. As a result, sediment transport and channel shoaling rates in any given year may deviate significantly from the values predicted in this study. Moreover, short-term rates such as averages over a month or a season may differ markedly from average rates over a year. Even the nature of sedimentation at a particular location may change from erosion to deposition and vice versa. This change is exemplified by the field data on shoaling rates shown in Figure 20. Therefore, the results of this study will provide reasonable estimates of the long-term yearly average values of sediment transport and channel shoaling rates, provided severe storms are excluded and the uncertainty in the results for the reach of channel between sta 325+00 and sta 399+74 is noted.

128. In general, the uncertainty in the predictions of the sediment transport model is reduced by verifying the model with field data from the project site. For St. Marys Inlet, field data from navigation channel surveys were available for about a year (November 1980 to December 1981) and are free from the effects of extreme storms. The model verification, as shown in Figure 22, is good. In a sense, the verification shown is an indirect verification of the modeling system approach as a whole. The yearly shoaling volumes predicted by the model for existing conditions are comparable to yearly maintenance dredging volumes recorded by CESAJ. In general, with proper verification numerical sediment transport models are better at predicting the effect of a change from one condition to another, such as from base to plan, than at predicting an absolute condition such as base or plan alone. In view of these facts, it is estimated that Model B results on sediment transport are accurate

to within  $\pm 25$  percent for base and Plan 1 conditions.

129. To keep things in perspective, it should be pointed out that at present the only possible alternative to a numerical sediment transport model is a physical movable-bed hydraulic model. Movable-bed coastal models are fairly complicated and expensive to construct and operate. Such models require more time than a numerical modeling effort. At present, there is no universal agreement on the scaling relations to be used. Movable-bed coastal models involving the combined action of waves and currents near inlets (the type required by the present study) are the most complicated of all coastal models and the least understood. Their results are approximate because there has to be a compromise between scaling relations necessary for waves only and scaling relations required for currents only. According to established experts, the accuracy of a coastal movable bed model of this type in the hands of an expert will be of the order of  $\pm 50-100$  percent. Thus, the results of the numerical modeling system employed in this study are definitely better than the alternative.

PART VI: RECOMMENDATIONS

Advance Maintenance Dredging

130. The following recommendations on advance maintenance dredging are based not only on Plan 1 results from Model B but also on all other available information such as field surveys and field experience. It must be emphasized that these recommendations are for an average year including normal storms and do not allow for the effects of abnormal storms such as hurricanes and tropical storms. Since the Navy wants a minimum clear depth of 46 ft mlw always and since it plans to dredge the channel only once a year, the deposition rates by zones as well as the deposition rates predicted by Model B for individual cells (Figure 29) have been taken into account in making these recommendations.

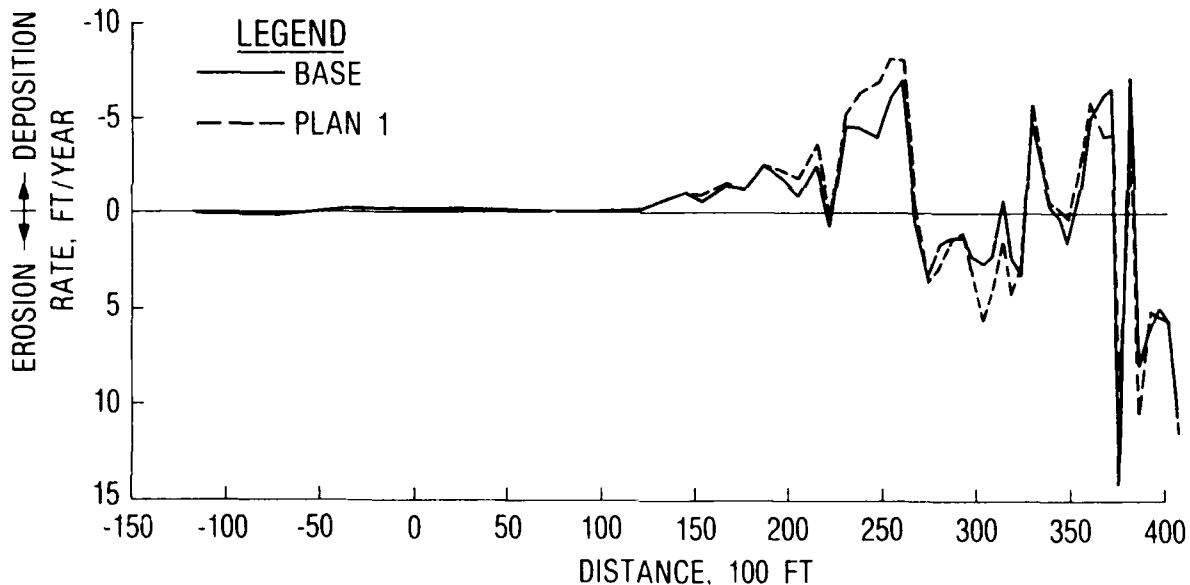


Figure 29. Comparison of computed erosion/deposition rates by cells for base and Plan 1

131. For reasons previously mentioned, the high local deposition rates predicted by Model B for base and Plan 1 in some reaches of the channel between sta 325+00 and sta 399+74 are suspect because up-to-date bathymetric data were not available for model calculations and there are no corroborating field data for such high rates. On the other hand, field surveys taken in April 1984 and December 1984 which covered the channel between these stations

and which became available after Model B was run, seem to indicate erosion rates of the order of 0.8 ft/year or less between sta 325+57 and sta 361+74 and deposition rates of the order of 1.4 ft/year or less between sta 361+74 and sta 399+74. In view of the uncertainty on sedimentation rates in the length of channel between sta 325+00 and sta 399+74, and because the existing depths in this reach are generally higher than 49 ft mlw, an advance maintenance depth of 3 ft is recommended in this reach.

132. For convenience in dredging, the channel was divided into reaches of at least 2,000-ft lengths at the suggestion of CESAJ. Table 5 lists the various reaches of Plan 1 entrance and offshore channels where shoaling is expected, estimates of deposition rates (rounded to 0.1 ft/year), and recommendations for advance maintenance depths (rounded generally to whole feet). If the length of channel between sta -97+76 and sta 325+00 is considered and only the rectangular portion of the planned channel cross section is taken, the total dredging volume for advance maintenance in accordance with the recommendations shown in Table 5 represents a savings of approximately 630,000 cu yd, or nearly 27 percent, compared to the dredging volume for a channel with 3-ft advance maintenance throughout this reach.

133. The recommendations given in Table 5 do not take into account the long-term economic advantages of providing greater advance maintenance depths and dredging less frequently than once a year, especially in the offshore areas, in view of the high cost of mobilization of dredging plant. This issue should be explored before a final decision is made on advance maintenance depths.

134. From the geologic sections provided by CESAJ, rock seems to be present at depths of 40 to 54 ft mlw between sta 234+00 and 260+00. Two of the reaches where large advance maintenance depths of the order of 7 to 9 ft have been recommended are in this general area. This is the area just outside of the jetty tips and just interior to the jetties. Severe deposition problems have been experienced in this general area at present because of material moving from the shoals on either side of the channel into the channel. Generally, the highest deposition rates have been observed in the northernmost quadrant of the channel. In view of the difficulty and expense of dredging in rock and problems that may be experienced with large overdepth dredging, it is suggested that overwidth dredging be explored as an alternative to overdepth dredging in this area. For instance, in addition to providing a reasonable

advance maintenance depth, the channel may be widened by 100 to 125 ft (total width of channel equals 600 to 625 ft) in this reach. Overwidth dredging may be considered also as an alternative in other reaches where rock may be present.

#### Future Testing

135. Model B results for Plan 1 provided in this report have been obtained by testing a 500-ft-wide channel with a project depth of 46 ft mlw and advance maintenance depth of 3 ft throughout. Once the channel design is finalized, it is recommended that the final design be tested in Model B with the latest available bathymetry in and around the channel so that maintenance dredging requirements can be determined more accurately corresponding to the final channel design.

136. Model B has been used in this study to estimate average yearly erosion/deposition rates in the entrance and offshore channels under average wave conditions, excluding abnormal storms. These estimates are good for predicting long-term average maintenance dredging requirements. However, the effect of severe storms such as hurricanes and tropical storms on shoaling can be quite dramatic. So it is recommended that shoaling of the planned navigation channel under severe storm conditions be investigated since estimates of shoaling volumes can be used in channel design as well as in advance planning for emergency mobilization of the necessary dredging plant to keep the channel open. This task can be performed using Model B and the storm surge modeling capability of WIFM.

## PART VII: SUMMARY AND CONCLUSIONS

137. To study the effects of proposed modification of the exterior channels of St. Marys Inlet (the ocean entrance to Kings Bay Naval Submarine Base) on coastal processes, the CIP system of numerical models of CEWES was employed. The system included models for tides, waves, wave-induced currents, and sediment transport. The system together with two computational grids developed for the study was called Model B.

138. Model B was used to study existing (base) conditions as well as planned conditions. Plan 1 is to (a) widen the navigation channel by 100 ft on the north side so the total width becomes 500 ft, (b) deepen the channel to -49 ft mhw (46-ft project depth plus 3-ft advance maintenance) with side slopes of 3H:1V, and (c) extend the channel on the ocean side with a 20-deg bend to the south at sta -97+76. It is assumed also that the landward 1,000 ft of the south jetty is made sand-tight for Plan 1.

139. The tidal model was verified using the field data of 10 November 1982. This was achieved by forcing the model with measured tidal elevations and matching observed velocities at ranges in the inlet, Cumberland Sound, and St. Marys River. There was good agreement.

140. The average year's wave climate for the study area was obtained from WESWIS, on the basis of 20-year hindcast data. The data set included normal storms but not hurricanes and tropical storms. This was used in running the wave and wave-induced current models.

141. The sediment transport model determined noncohesive sediment (sand) transport in the study area, under the combined action of tides, waves and wave-induced currents. It considered a mean tide and the average year's wave climate.

142. The sediment transport model was verified by comparing computed erosion/deposition rates in the navigation channel with those obtained from field surveys taken by CFSAJ during 1980-81. There was good agreement with respect to both trends and magnitudes.

143. While all four models were run for base conditions, only the tide model and the sediment transport model were run for plan conditions (Plan 1) to meet the urgent need for model results. (Plan conditions were expected to influence the tide and sediment transport much more than the waves and wave-induced currents.)

144. The effects of Plan 1 on tidal currents were mainly local and caused by sand-tightening of the south jetty. Velocities at the end of the jetties and at tide Gage 1 increased by approximately 10 percent. There were no significant changes in velocities at the throat of the inlet, including Range 1 and the Fort Clinch area.

145. Model B predicts an increase in deposition and erosion rates between sta -97+76 and sta 325+00 from base to Plan 1. For the reach of channel between sta -80+00 and sta 325+00, the predicted yearly shoaling volumes are 475,000 and 788,000 cu yd/year for base and Plan 1, respectively, or an increase of 66 percent for Plan 1.

146. On the basis of Model B results and all other available information, recommendations on advance maintenance dredging were made for different reaches of the navigation channel (Table 5).

147. For the length of channel between sta -97+76 and sta 325+00, if only the rectangular portion of the planned channel cross section is considered, the total dredging volume for advance maintenance in accordance with Model B recommendations represents a savings of approximately 630,000 cu yd or nearly 27 percent compared to the dredging volume for a channel with 3-ft advance maintenance throughout according to Plan 1.

148. In summary, the study successfully accomplished all the study objectives, as set forth in paragraph 3, "Purpose," except for the determination of waves and wave-induced currents under plan conditions. The numerical models for these processes were not rerun, as originally planned, in order to meet the urgent needs of the sponsor.

## REFERENCES

- Ackers, P., and White, W. R. 1973. "Sediment Transport: New Approach and Analysis," Journal of the Hydraulics Division, American Society of Civil Engineers, Vol 99, No. HY11, pp 2041-2060.
- Bagnold, R. A. 1963. "Mechanics of Marine Sedimentation," The Sea, M. N. Hill, ed., Interscience Publishers, Wiley, New York, Vol 3, pp 507-528.
- Berkhoff, J. C. W. 1972. "Computation of Combined Refraction-Diffraction," Proceedings of the 13th International Conference on Coastal Engineering, American Society of Civil Engineers, Vol 1, pp 471-490.
- \_\_\_\_\_. 1976. "Mathematical Models for Simple Harmonic Linear Water Waves, Wave Diffraction and Refraction," Publication No. 1963, Delft Hydraulics Laboratory, Delft, The Netherlands.
- Bijker, E. W. 1967. "Some Considerations About Scales for Coastal Models with Movable Bed," Delft Hydraulics Laboratory, Publication 50, Delft, The Netherlands.
- Butler, H. Lee. In preparation. "WIFM--WES Implicit Flooding Model: Theory and Program Documentation," Technical Report, US Army Engineer Waterways Experiment Station, Vicksburg, Miss.
- Chow, Ven Te. 1959. Open-Channel Hydraulics, McGraw-Hill Book Company, Inc., New York.
- Dally, W. R., Dean, R. G., and Dalrymple, R. A. 1984. "Modeling Wave Transformation in the Surf Zone," Miscellaneous Paper CERC-84-8, US Army Engineer Waterways Experiment Station, Vicksburg, Miss.
- Ebersole, B. A. 1980. "A Numerical Model for Nearshore Circulation Including Convective Accelerations and Lateral Mixing," Master's thesis, University of Delaware, Newark, Delaware.
- Ebersole, B. A., Cialone, M. A., and Prater, M. D. 1986. "Regional Coastal Processes Numerical Modeling System; Report 1, RCPWAVE--A Linear Wave Propagation Model for Engineering Use," Technical Report CERC-86-4, US Army Engineer Waterways Experiment Station, Vicksburg, Miss.
- Granat, M. A., et al. In preparation. "Hydrodynamic and Sediment Transport Hybrid Modeling of Cumberland Sound and Kings Bay Navigation Channel, Georgia: Verification and Basic Plan Testing," Technical Report HL-88- , US Army Engineer Waterways Experiment Station, Vicksburg, Miss.
- Hales, L. Z. 1980. "Erosion Control of Scour During Construction; Report 3, Experimental Measurements of Refraction, Diffraction, and Current Patterns Near Jetties," Technical Report HL-80-3, US Army Engineer Waterways Experiment Station, Vicksburg, Miss.
- Hirakawa, H., and Fuo, C. T. 1966. "A Study of Wave Transformation Inside Surf Zone," Proceedings of the 10th International Conference on Coastal Engineering, American Society of Civil Engineers, pp 217-233.
- Sanjivan, S. K. 1981. "Combined Refraction and Diffraction of Short Waves Using the Finite Element Method," Applied Ocean Research, Vol 3, No. 3, pp 163-170.

Jonsson, I. G. 1966. "Wave Boundary Layers and Friction Factors," Proceedings, Tenth Coastal Engineering Conference, American Society of Civil Engineers, Tokyo, Japan, pp 127-148.

Jonsson, I. G., Skovgaard, O., and Jacobsen, T. S. 1974. "Computation of Longshore Currents," Proceedings, Fourteenth Coastal Engineering Conference, American Society of Civil Engineers, Copenhagen, Denmark, pp 699-714.

Komar, P. D. 1977. "Beach Sand Transport: Distribution and Total Drift," Journal of the Waterway, Port, Coastal and Ocean Division, American Society of Civil Engineers, Vol 103, No. WW2, pp 225-239.

\_\_\_\_\_. 1978. "Relative Quantities of Suspension Versus Bedload Transport on Beaches," Journal of Sedimentary Petrology, Vol 48, No. 3, pp 921-932.

Leendertse, J. J. 1970. "A Water-Quality Simulation Model for Well-Mixed Estuaries and Coastal Seas; Principles of Computation," RM-6230-rc, Vol 1, Rand Corporation.

Leenknecht, D. A., Earickson, J. A., and Butler, H. L. 1984. "Numerical Simulation of Oregon Inlet Control Structures' Effects on Storm and Tide Elevations in Pamlico Sound," Technical Report CERC-84-2, US Army Engineer Waterways Experiment Station, Vicksburg, Miss.

Longuet-Higgins, M. S. 1970. "Longshore Currents Generated by Obliquely Incident Sea Waves, 1 and 2," Journal of Geophysical Research, Vol 75, No. 33, pp 6778-6789 and pp 6790-6801.

Longuet-Higgins, M. S., and Stewart, R. W. 1964. "Radiation Stresses in Water Waves; A Physical Discussion, with Applications," Deep-Sea Research, Vol 11, pp 529-562.

Parchure, T. M. 1982. "St. Marys Entrance Glossary of Inlets Report #11," Report No. 44, Department of Coastal and Oceanographic Engineering, University of Florida, Gainesville, Fla.

Penney, W. G., and Price, A. T. 1952. "The Diffraction Theory of Sea Waves and the Shelter Afforded by Breakwaters," Philosophical Transactions of the Royal Society of London, Vol A244, pp 236-253.

Perlin, M., and Dean, R. G. 1983. "A Numerical Model to Simulate Sediment Transport in the Vicinity of Coastal Structures," CERC Miscellaneous Report 83-10, US Army Engineer Waterways Experiment Station, Vicksburg, Miss.

Phillips, O. M. 1969. The Dynamics of the Upper Ocean, Cambridge University Press, Cambridge, Mass.

Reid, R. O., and Bodine, B. R. 1968. "Numerical Model for Storm Surges in Galveston Bay," Journal, Waterways and Harbors Division, American Society of Civil Engineers, Vol 94, No. WW1, Proceedings Paper 5805, pp 33-57.

Sheng, Y. P., Segur, H., and Lewellen, W. S. 1978. "Application of a Spatial Smoothing Scheme to Control Short-Wave Numerical Oscillation-," Technical Memorandum No. 78-8, Aeronautical Research Associates of Princeton, Princeton, N. J.

Shore Protection Manual, 1984. 4th ed., 2 Vols, US Army Engineer Waterways Experiment Station, Coastal Engineering Research Center, US Government Printing Office, Washington, DC.

Smith, R., and Sprinks, T. 1975. "Scattering of Surface Waves by a Conical Island," Journal of Fluid Mechanics, Vol 72, Part 2, pp 373-384.

Swart, D. H. 1974. "Offshore Sediment Transport and Equilibrium Beach Profiles," Delft Hydraulics Laboratory, Publication No. 131, Delft, The Netherlands.

Thornton, E. B. 1970. "Variation of Longshore Current Across the Surf Zone," Proceedings, Twelfth Coastal Engineering Conference, American Society of Civil Engineers, Washington, DC, pp 291-308.

\_\_\_\_\_. 1972. "Distribution of Sediment Transport Across the Surf Zone," Proceedings, Thirteenth Coastal Engineering Conference, American Society of Civil Engineers, Vancouver, Canada, pp 1049-1068.

Thornton, E. B., and Guza, R. T. 1982. "Energy Saturation and Phase Speeds Measured on a Natural Beach," Journal of Geophysical Research, Vol 87, No. C12, pp 9499-9508.

Vemulakonda, S. R. 1984. "Erosion Control of Scour During Construction; Report 7, CURRENT--A Wave-Induced Current Model," Technical Report HL-80-3, US Army Engineer Waterways Experiment Station, Vicksburg, Miss.

Vemulakonda, S. R., et al. 1985. "Coastal and Inlet Processes Numerical Modeling System for Oregon Inlet, North Carolina," Technical Report CERC-85-6, US Army Engineer Waterways Experiment Station, Vicksburg, Miss.

Vreugdenhil, C. B. 1973. "Secondary-Flow Computations," Publication No. 144, Delft Hydraulics Laboratory, The Netherlands.

Wanstrath, J. J. 1977. "Nearshore Numerical Storm Surge and Tidal Simulation," Technical Report H-77-17, US Army Engineer Waterways Experiment Station, Vicksburg, Miss.

Weare, J. T. 1976. "Instability in Tidal Flow Computational Schemes," Journal, Hydraulics Division, American Society of Civil Engineers, Vol 102, pp 569-580.

Weggel, J. R. 1972. "Maximum Breaker Height," Journal of the Waterways, Harbors, and Coastal Engineering Division, Vol 78, No. WW4, pp 529-548.

Williams, R. G., Darbyshire, J., and Holmes, P. 1980. "Wave Refraction and Diffraction in a Caustic Region: A Numerical Solution and Experimental Validation," Proceedings of the Institution of Civil Engineering, Vol 69, Part 2, pp 635-649.

## BIBLIOGRAPHY

Florida Coastal Engineers. 1976. "Beach Erosion Control Study, Nassau County, Florida. Appendix 2." Report prepared under Contract No. DACW17-75C-0039 for US Army Engineer District, Jacksonville, Florida.

Jensen, R. E. 1983. "Atlantic Coast Hindcast, Shallow-Water, Significant Wave Information," WIS Report 9, US Army Engineer Waterways Experiment Station, Vicksburg, Miss.

Olsen, E. J. 1977. "A Study of the Effects of Inlet Stabilization at St. Marys Entrance, Florida," Proceedings of the Coastal Sediments '77 Conference, American Society of Civil Engineers, pp 311-329.

US Army Engineer District, Jacksonville. 1984 (revised March 1985). "Feasibility Report with EIS for Beach Erosion Control, Nassau County, Florida (Amelia Island)," Jacksonville, Fla.

\_\_\_\_\_. 1984. "Fort Clinch, Nassau County, Florida," Section 103 Detailed Project Report and Environmental Assessment, Jacksonville, Fla.

Vemulakonda, S. R., and Scheffner, N. W. 1987. "Application of CIP Modeling System to St. Marys Inlet, Florida," Proceedings of the Coastal Sediments '87 Conference, American Society of Civil Engineers, Vol I, pp 616-631.

Table 1  
Numerical Gages Used in WIFM

<u>Numerical Gage No.</u>	<u>Gage Name</u>
1	Prototype tide Gage 1 (south spit)
5	Endeco velocity Gage 2 (main channel)
10	Range survey Gage 1-A
11	Range survey Gage 1-B
12	Range survey Gage 1-C
25	Ocean end of jetties-channel
27	Fort Clinch
28	South channel (Amelia Island)
29	Channel to Cumberland

Table 2

Sample of WESWIS Data for St. Marys Inlet

STATION 232 20 YEARS WAVE APPROACH ANGLE(DEGREES)= 60.0 - 69.9  
 SHORELINE ANGLE = 355.0 DEGREES AZIMUTH  
 WATER DEPTH = 18.29 METRES  
 PERCENT OCCURRENCE(X1000) OF HEIGHT AND PERIOD BY DIRECTION

HEIGHT(METRES)	PERIOD(SECONDS)										TOTAL
	0.0- 2.9	3.0- 3.9	4.0- 4.9	5.0- 5.9	6.0- 6.9	7.0- 7.9	8.0- 8.9	9.0- 9.9	10.0- 10.9	11.0- LONGER	
0.0 - 0.49	482	448	609	.	294	46	3	25	118	.	1416
0.50 - 0.99	3	355	94	.	13	82	3	5	78	.	1148
1.00 - 1.49	.	.	.	237	1	34	1	10	.	.	377
1.50 - 1.99	.	.	.	46	58	8	13	3	1	.	129
2.00 - 2.49	.	.	.	.	27	34	8	1	.	.	70
2.50 - 2.99	.	.	.	.	1	11	1	.	.	.	38
3.00 - 3.49	.	.	.	.	.	.	.	.	.	.	13
3.50 - 3.99	.	.	.	.	.	.	.	.	.	.	0
4.00 - 4.49	.	.	.	.	.	.	.	.	.	.	0
4.50 - 4.99	.	.	.	.	.	.	.	.	.	.	0
5.00 - GREATER	.	.	.	.	.	.	.	.	.	.	0
TOTAL	485	803	703	283	400	247	29	34	207	0	

AVERAGE HS(M) = 0.69    LARGEST HS(M) = 3.45    ANGLE CLASS % = 3.2

STATION 232 20 YEARS WAVE APPROACH ANGLE(DEGREES)= 70.0 - 79.9  
 SHORELINE ANGLE = 355.0 DEGREES AZIMUTH  
 WATER DEPTH = 18.29 METRES  
 PERCENT OCCURRENCE(X1000) OF HEIGHT AND PERIOD BY DIRECTION

HEIGHT(METRES)	PERIOD(SECONDS)										TOTAL
	0.0- 2.9	3.0- 3.9	4.0- 4.9	5.0- 5.9	6.0- 6.9	7.0- 7.9	8.0- 8.9	9.0- 9.9	10.0- 10.9	11.0- LONGER	
0.0 - 0.49	492	450	581	.	119	123	870	395	213	853	3515
0.50 - 0.99	.	381	100	.	22	111	747	347	174	11	2374
1.00 - 1.49	.	.	.	266	1	136	94	53	6	.	656
1.50 - 1.99	.	.	.	78	66	39	65	11	.	.	259
2.00 - 2.49	.	.	.	3	49	37	39	6	.	.	134
2.50 - 2.99	.	.	.	.	13	75	6	.	.	.	94
3.00 - 3.49	.	.	.	.	.	5	.	.	.	.	5
3.50 - 3.99	.	.	.	.	.	.	.	.	.	.	0
4.00 - 4.49	.	.	.	.	.	.	.	.	.	.	0
4.50 - 4.99	.	.	.	.	.	.	.	.	.	.	0
5.00 - GREATER	.	.	.	.	.	.	.	.	.	.	0
TOTAL	492	831	681	347	270	526	1821	812	393	864	

AVERAGE HS(M) = 0.62    LARGEST HS(M) = 3.28    ANGLE CLASS % = 7.1

STATION 232 20 YEARS WAVE APPROACH ANGLE(DEGREES)= 80.0 - 89.9  
 SHORELINE ANGLE = 355.0 DEGREES AZIMUTH  
 WATER DEPTH = 18.29 METRES  
 PERCENT OCCURRENCE(X1000) OF HEIGHT AND PERIOD BY DIRECTION

HEIGHT(METRES)	PERIOD(SECONDS)										TOTAL
	0.0- 2.9	3.0- 3.9	4.0- 4.9	5.0- 5.9	6.0- 6.9	7.0- 7.9	8.0- 8.9	9.0- 9.9	10.0- 10.9	11.0- LONGER	
0.0 - 0.49	482	451	715	.	552	651	520	58	1401	1134	5249
0.50 - 0.99	.	402	118	.	10	691	533	85	1411	1062	4909
1.00 - 1.49	.	.	.	328	.	143	203	73	361	123	1349
1.50 - 1.99	.	.	.	94	112	65	130	54	71	20	546
2.00 - 2.49	.	.	.	3	53	59	75	32	25	41	288
2.50 - 2.99	.	.	.	.	20	100	29	11	22	11	193
3.00 - 3.49	.	.	.	.	.	37	.	.	18	3	58
3.50 - 3.99	.	.	.	.	.	.	1	.	1	.	2
4.00 - 4.49	.	.	.	.	.	.	.	.	.	1	1
4.50 - 4.99	.	.	.	.	.	.	.	.	.	.	0
5.00 - GREATER	.	.	.	.	.	.	.	.	.	.	0
TOTAL	482	853	833	425	747	1746	1491	313	3310	2395	

AVERAGE HS(M) = 0.72    LARGEST HS(M) = 4.32    ANGLE CLASS % = 12.6

Table 3

## Incident Wave Conditions for St. Marys Inlet

	DIRECTION (DEGS)	HEIGHT (FT)	PERIOD (SECS)	PERCENT	COM. FREQ. OCCUR.
1	-72.50	.82	3.20	4.211	.94811
2	-72.50	2.46	5.30	1.917	.96823
3	-72.50	4.10	6.30	1.255	.96463
4	-72.50	.82	3.50	2.182	.95565
5	-72.50	2.46	4.50	1.838	.97793
6	-72.50	4.10	6.50	1.550	.96378
7	-72.50	5.74	7.30	1.220	.95538
8	-72.50	.82	3.40	1.563	.92461
9	-72.50	2.46	4.70	1.215	.93776
10	-72.50	4.10	5.70	.964	.94180
11	-72.50	5.74	6.30	.932	.94312
12	-72.50	7.38	7.40	.932	.94404
13	-72.50	.82	5.20	2.733	.91202
14	-72.50	2.46	5.50	1.635	.96897
15	-72.50	4.10	5.70	.444	.93241
16	-72.50	5.74	6.30	.116	.93457
17	-72.50	7.38	7.20	.115	.93572
18	-72.50	.82	7.20	9.409	.85381
19	-72.50	2.46	5.30	1.335	.90376
20	-72.50	4.10	6.00	.456	.93922
21	-72.50	5.74	6.60	.155	.93957
22	-72.50	7.38	7.20	.027	.91077
23	-72.50	.82	4.30	1.456	.92493
24	-72.50	2.46	4.90	1.143	.93541
25	-72.50	4.10	5.60	.577	.94013
26	-72.50	5.74	6.50	.129	.94147
27	-72.50	7.38	7.30	.121	.94267
28	-72.50	.82	9.00	3.515	.97753
29	-72.50	2.46	7.00	2.574	.94157
30	-72.50	4.10	6.60	.656	.94813
31	-72.50	5.74	7.00	.259	.94172
32	-72.50	7.38	7.50	.134	.94296
33	-72.50	3.02	7.40	.099	.941305
34	-2.50	.82	8.50	5.249	.46554
35	-2.50	2.46	8.60	4.903	.51463
36	-2.50	4.10	9.30	1.349	.52912
37	-2.50	5.74	8.00	.546	.53353
38	-2.50	7.38	8.90	.288	.53646
39	-2.50	9.02	8.30	.133	.53839
40	-2.50	10.66	3.70	.061	.53900
41	7.50	.82	7.10	4.137	.53097
42	7.50	2.46	6.70	2.532	.60629
43	7.50	4.10	6.90	1.075	.61704
44	7.50	5.74	7.40	.439	.62193
45	7.50	7.38	7.50	.327	.62520
46	7.50	9.02	7.60	.173	.62638
47	7.50	10.66	7.50	.065	.62763
48	17.50	.82	6.00	2.732	.65553
49	17.50	2.46	5.40	1.502	.67057
50	17.50	4.10	6.00	.761	.67819
51	17.50	5.74	6.60	.327	.69145
52	17.50	7.38	7.00	.218	.69363
53	17.50	9.02	7.50	.158	.69521
54	17.50	10.66	7.50	.119	.69639
55	27.50	.82	4.10	1.177	.69316
56	27.50	2.46	4.20	1.164	.70980
57	27.50	4.10	5.30	.816	.71596
58	27.50	5.74	6.20	.370	.71966
59	27.50	7.38	6.90	.254	.72220
60	27.50	9.02	7.40	.208	.72428
61	27.50	10.66	7.50	.165	.72533
62	37.50	.82	2.60	.728	.73021
63	37.50	2.46	4.20	1.244	.74365
64	37.50	4.10	5.30	.306	.75471
65	37.50	5.74	6.20	.439	.75969
66	37.50	7.38	6.90	.306	.76275
67	37.50	9.02	7.50	.149	.76424
68	37.50	10.66	7.50	.068	.76432
69	47.50	.82	2.70	.937	.77393
70	47.50	2.46	4.40	1.225	.78614
71	47.50	4.10	5.40	1.338	.79762
72	47.50	5.74	6.00	.434	.80136
73	47.50	7.38	6.70	.091	.80227
74	57.50	.82	4.10	1.706	.81933
75	57.50	2.46	5.20	2.106	.84033
76	57.50	4.10	5.70	.829	.84878
77	57.50	5.74	6.10	.070	.84949
78	67.50	.82	4.90	4.051	.83333
79	67.50	2.46	5.70	1.834	.83693
80	.00	.00	.00	10.317	1.00000

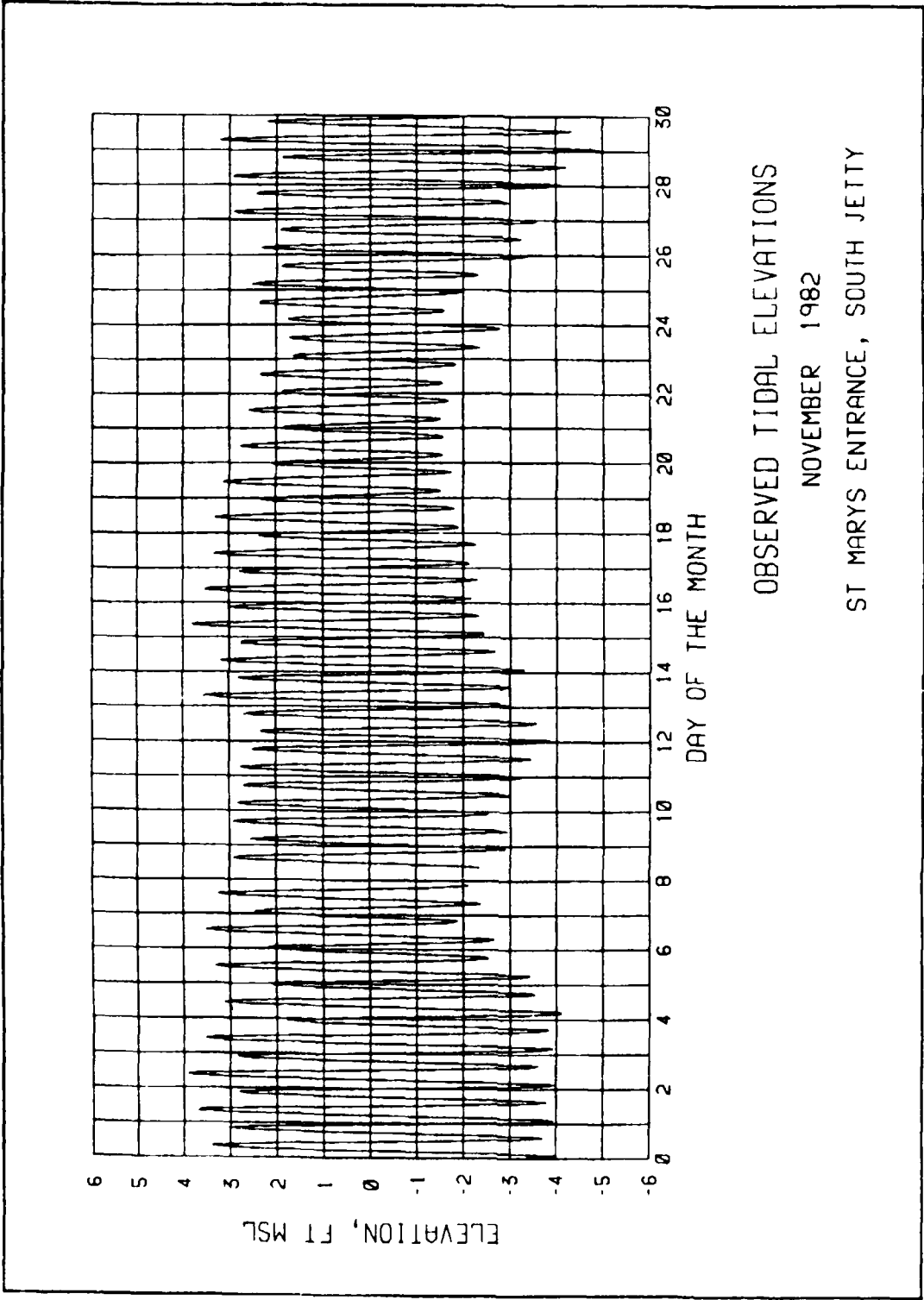
Table 4

Details of CESAJ Examination Surveys

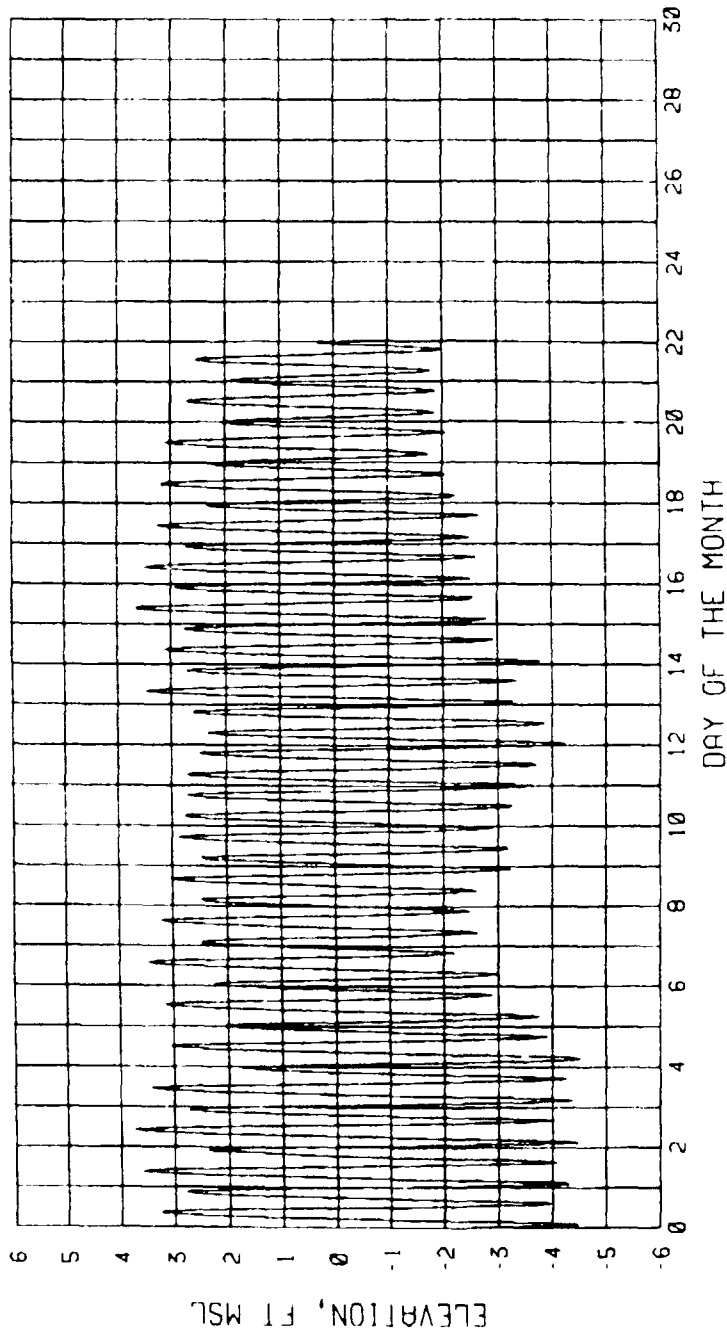
<u>Survey</u>	<u>Inclusive Dates</u>	<u>Surveyed Stations</u>
1	21-25 Nov 80	130+00 to 325+00
2	8-9 Dec 80	-80+00 to 130+00
3	31 Mar-13 Apr 81	130+00 to 325+00
4	13 Mar-13 Apr 81	-80+00 to 130+00
5	8 Jun 81	130+00 to 325+00
6	8-10 Jun 81	-80+00 to 130+00
7	14-18 Dec 81	-80+00 to 325+00

Table 5  
Recommendations for Advance Maintenance Depths

<u>Reach of Channel (CESAJ sta)</u>	<u>Estimated Maximum Local Deposition Rate ft/year</u>	<u>Recommended Advance Maintenance Depth ft</u>
-97+76 to 42+38	0.3	1.0
42+38 to 128+72	0.3	1.0
128+72 to 181+20	1.8	2.0
181+20 to 225+79	3.7	4.0
225+79 to 249+03	6.9	7.0
249+03 to 269+85	8.2	8.5
276+31 to 310+38	1.5	2.0
325+00 to 399+74	--	3.0



OBSERVED TIDAL ELEVATIONS  
NOVEMBER 1982  
ST MARYS ENTRANCE, SOUTH JETTY

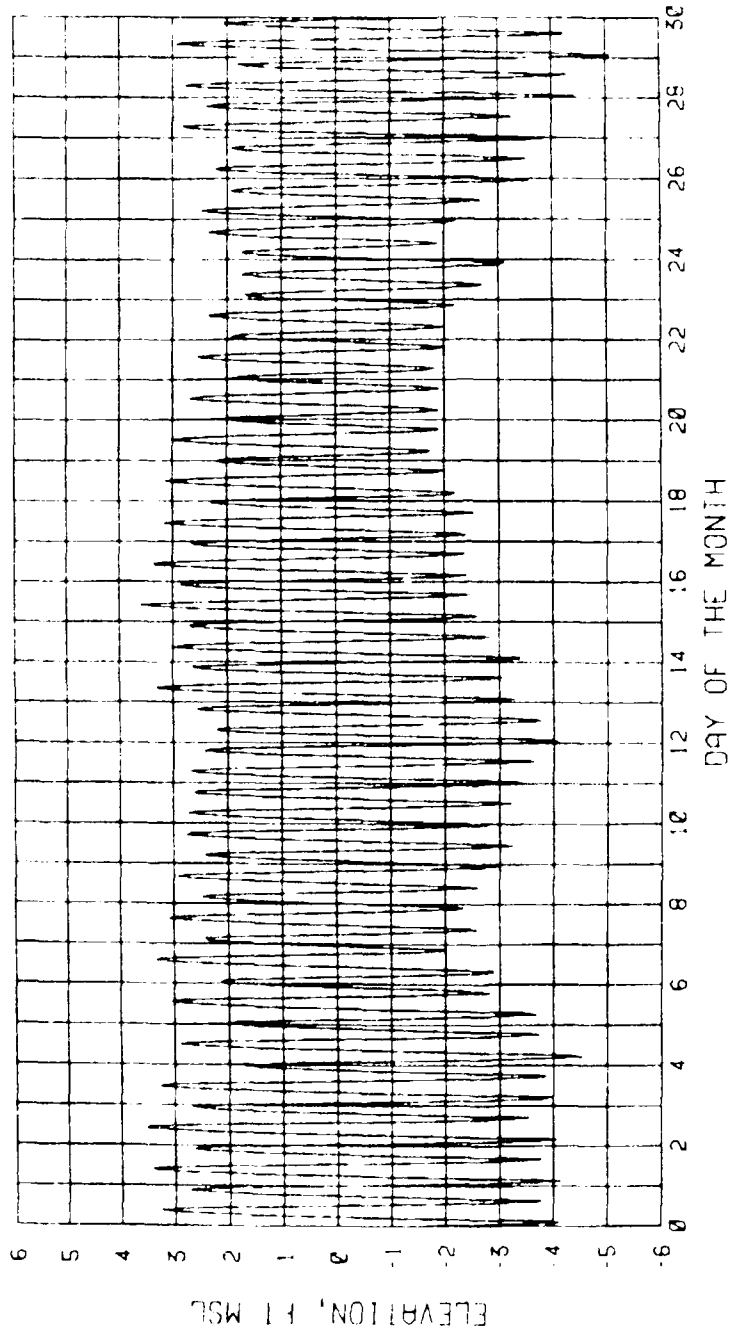


OBSERVED TIDAL ELEVATIONS

NOVEMBER 1982

FERNANDINA BEACH, AMELIA RIVER

PLATE 2



OBSERVED TIDAL ELEVATIONS

NOVEMBER 1982

ST. MARYS RIVER, NATIONAL PARK SERVICE DOCK

AD-A194 389

KINGS BAY COASTAL PROCESSES NUMERICAL MODEL(U) COASTAL  
ENGINEERING RESEARCH CENTER VICKSBURG MS  
S R VENULAKONDA ET AL. APR 89 CERC-TR-88-3

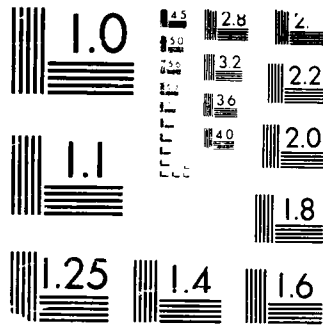
2/2

UNCLASSIFIED

F/G 13/2

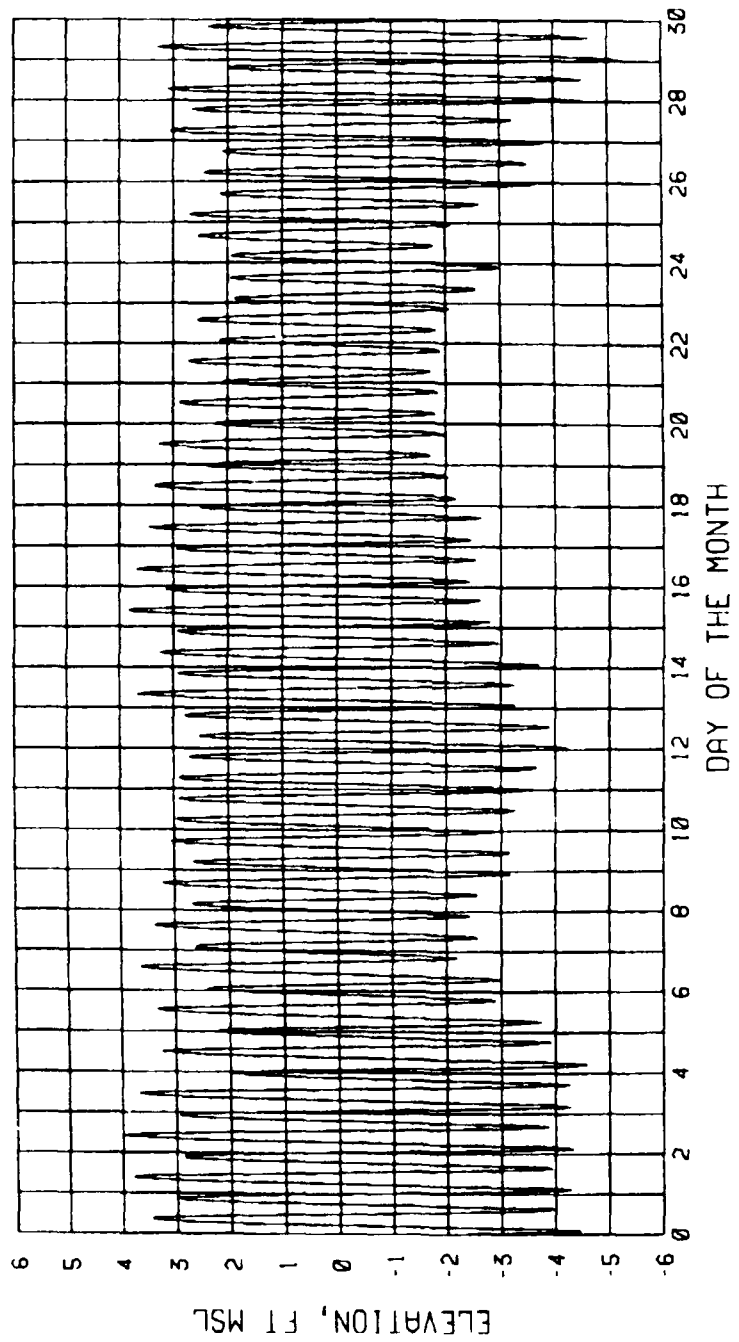
NL



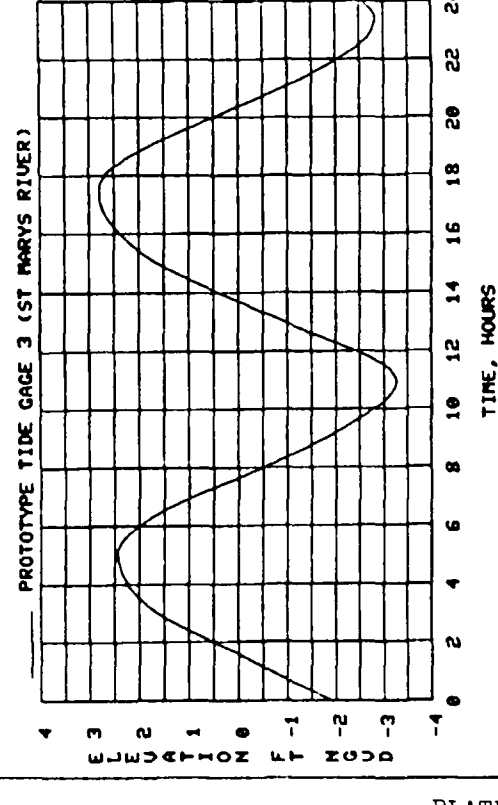
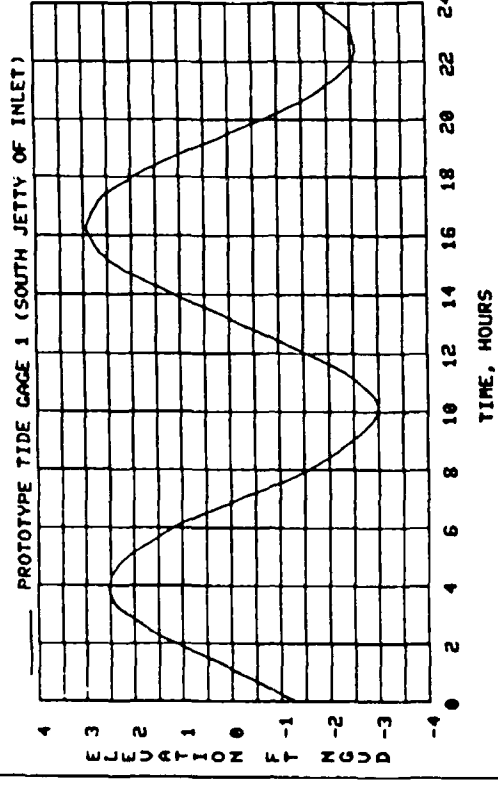
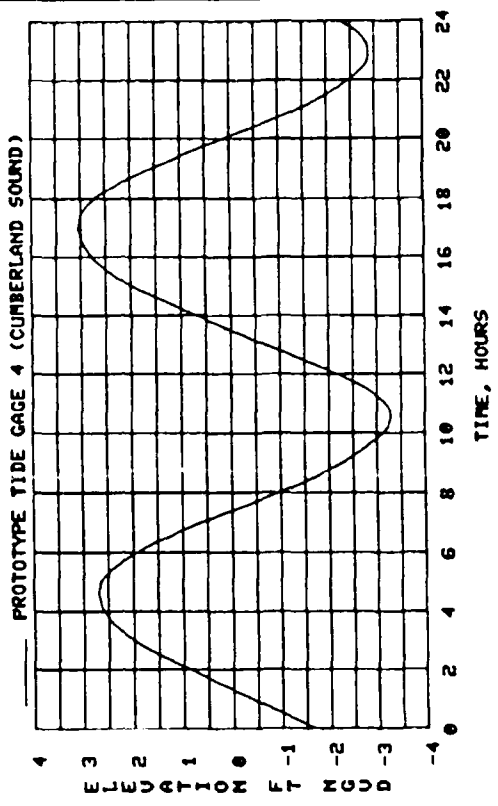
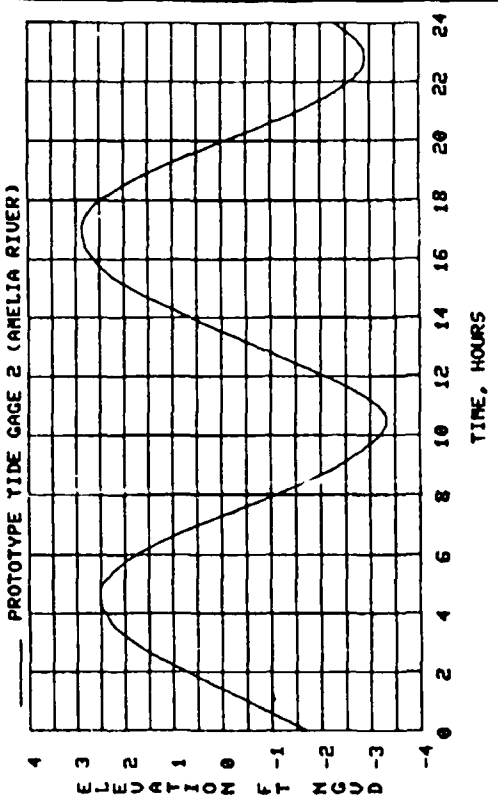


MICROCOPY RESOLUTION TEST CHART

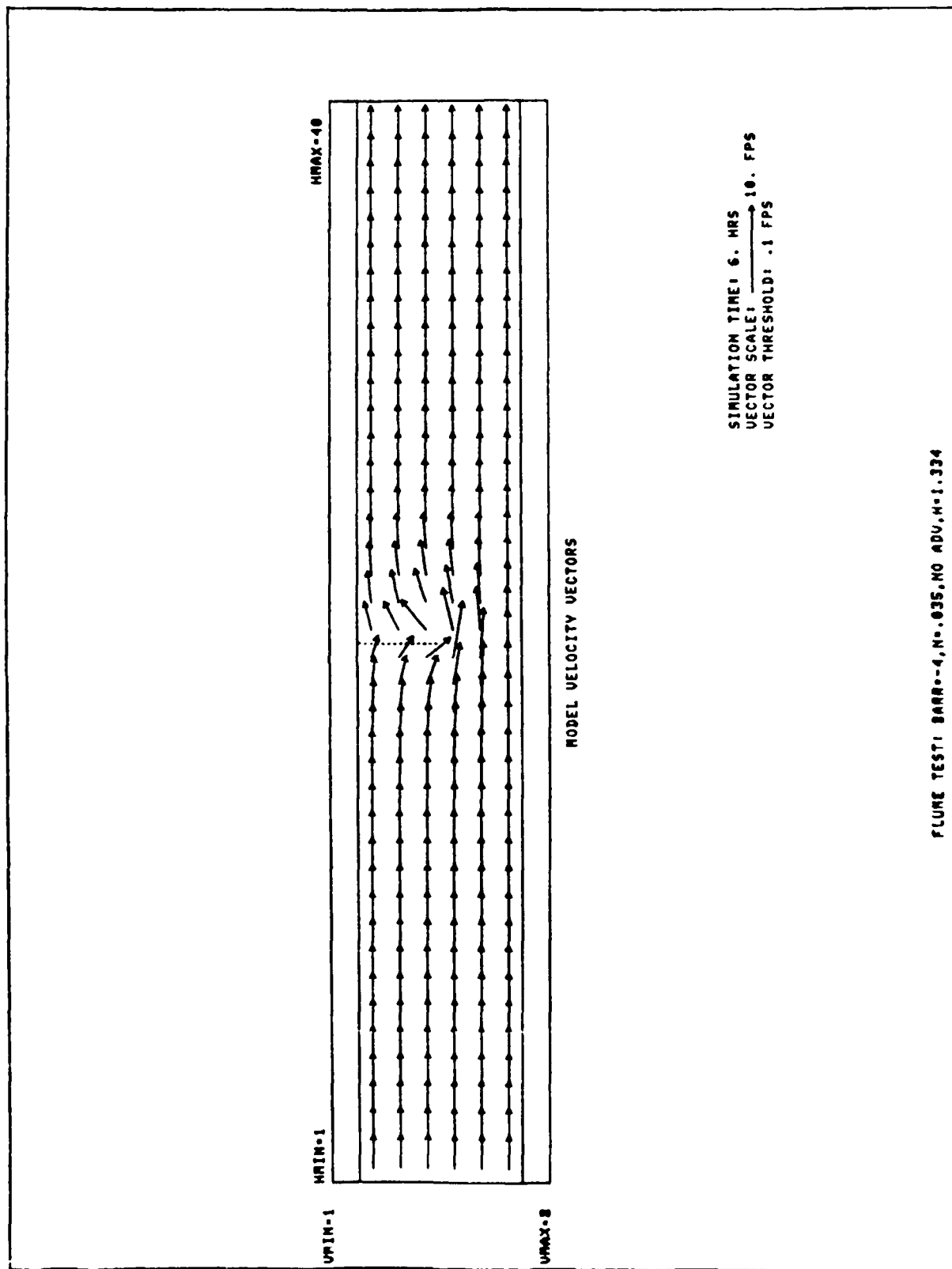
U.S. GOVERNMENT PRINTING OFFICE: 1963-O



OBSERVED TIDAL ELEVATIONS  
NOVEMBER 1982  
CUMBERLAND SCUND



PROTOTYPE TIDES (11/10/82): ELEVATIONS RELATIVE TO GAGE MEANS



FLUME TEST: BARR=4, N=0.035, NO ADV, H=1.334

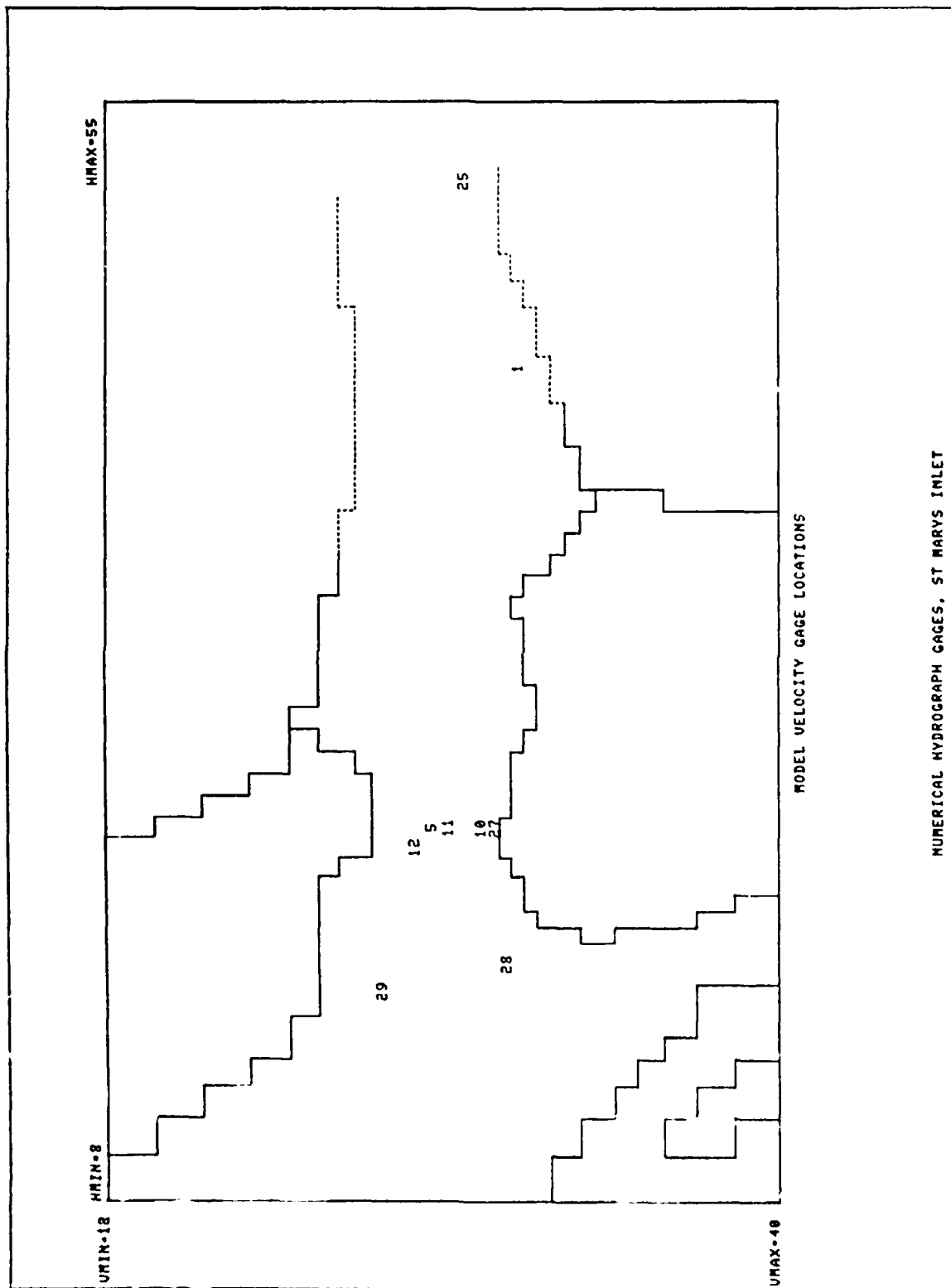
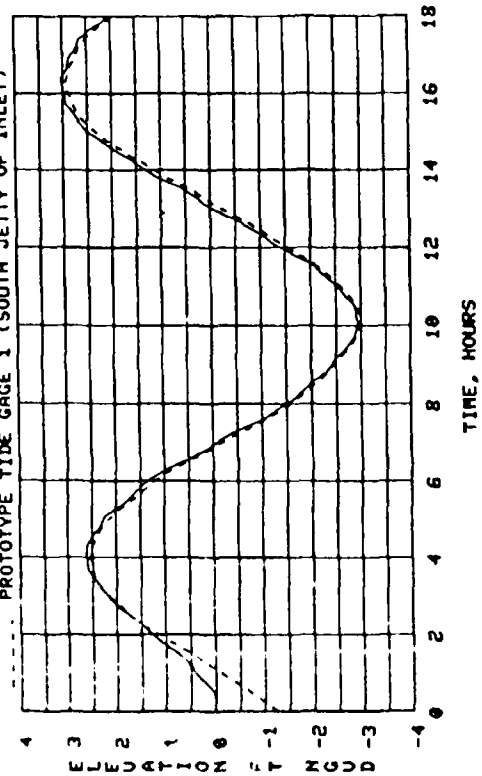
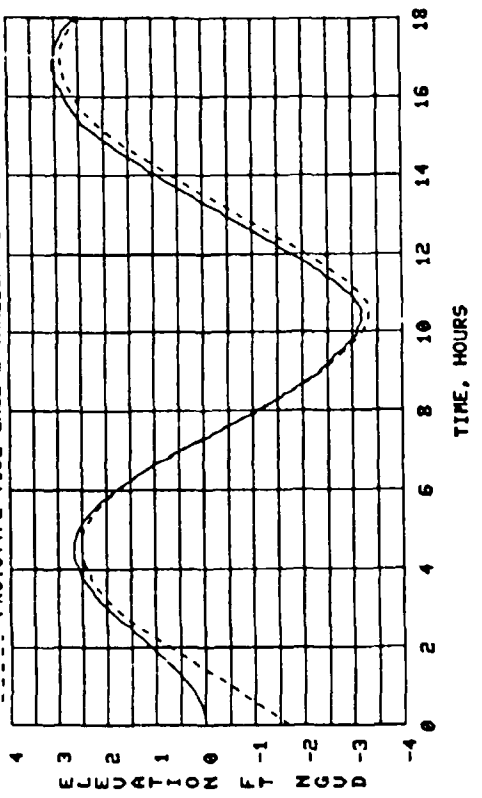


PLATE 7

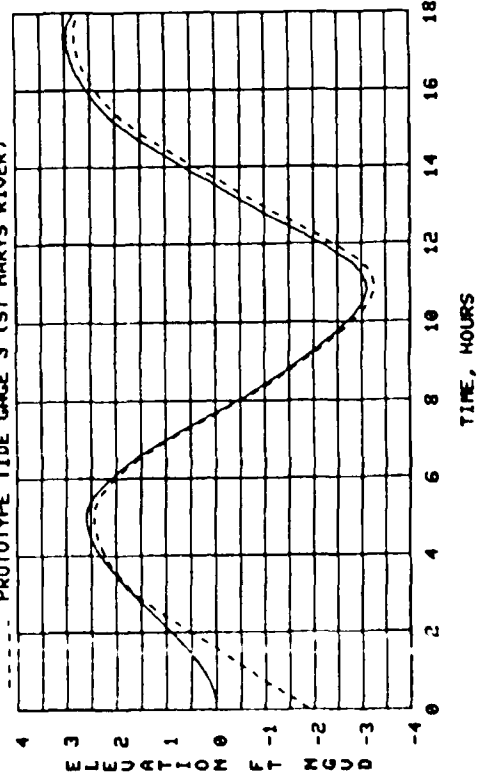
TIDE GAGE 1 (SOUTH JETTY OF INLET)  
PROTOTYPE TIDE GAGE 1 (SOUTH JETTY OF INLET)



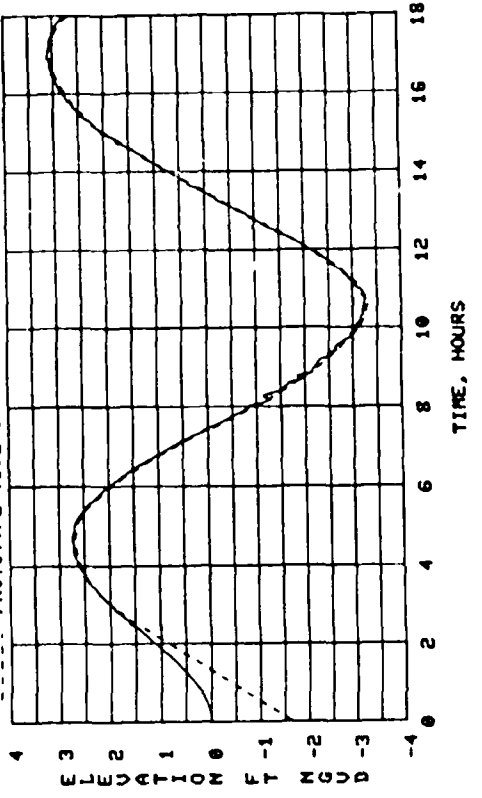
TIDE GAGE 2 (AMELIA RIVER)  
PROTOTYPE TIDE GAGE 2 (AMELIA RIVER)



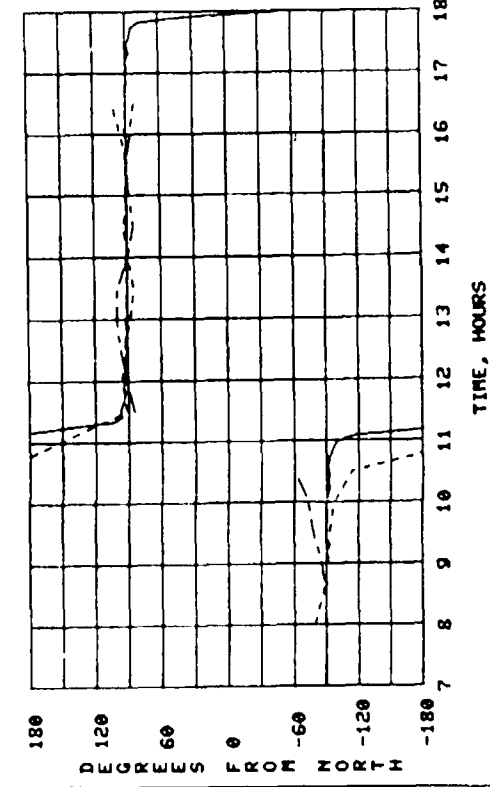
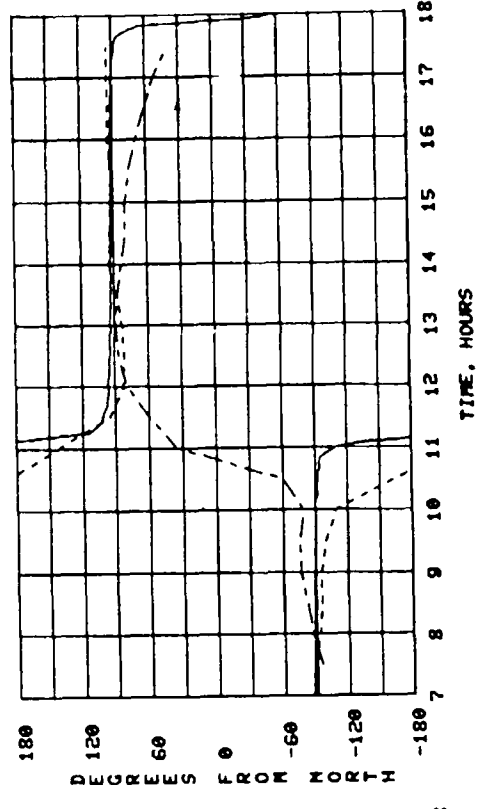
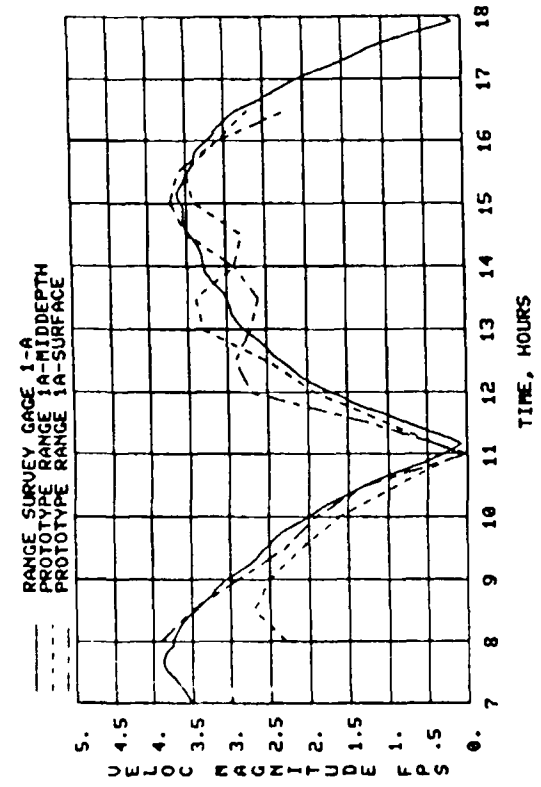
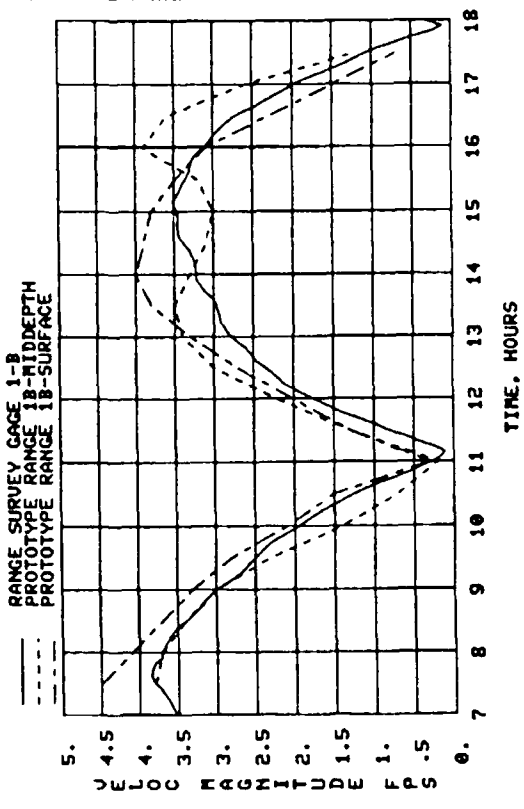
TIDE GAGE 3 (ST MARYS RIVER)  
PROTOTYPE TIDE GAGE 3 (ST MARYS RIVER)



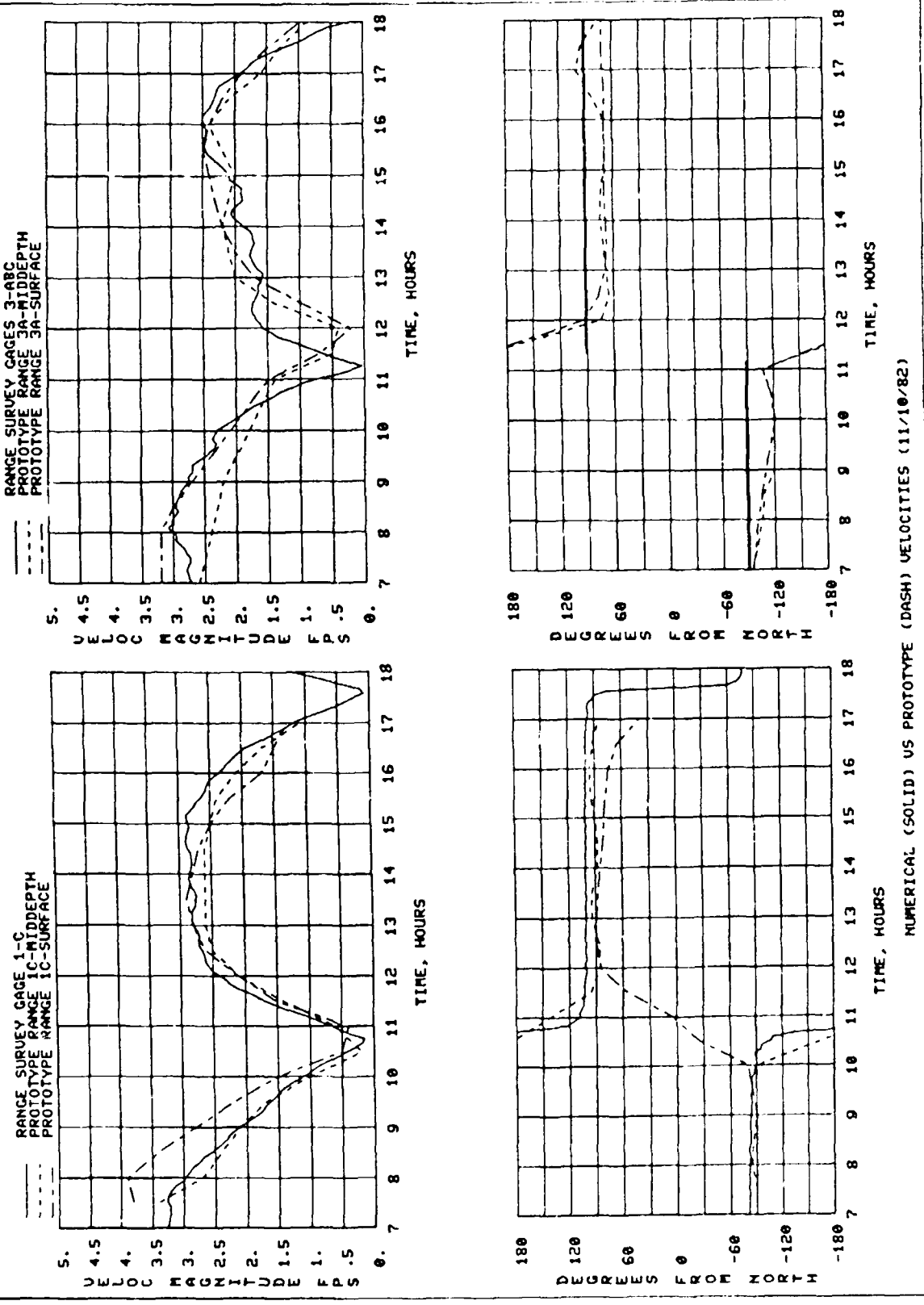
TIDE GAGE 4 (CUMBERLAND SOUND)  
PROTOTYPE TIDE GAGE 4 (CUMBERLAND SOUND)



NUMERICAL (SOLID) VS PROTOTYPE MEAN (DASH) TIDES - 11/10/82



NUMERICAL (SOLID) VS PROTOTYPE (DASH) VELOCITIES (11/10/82)



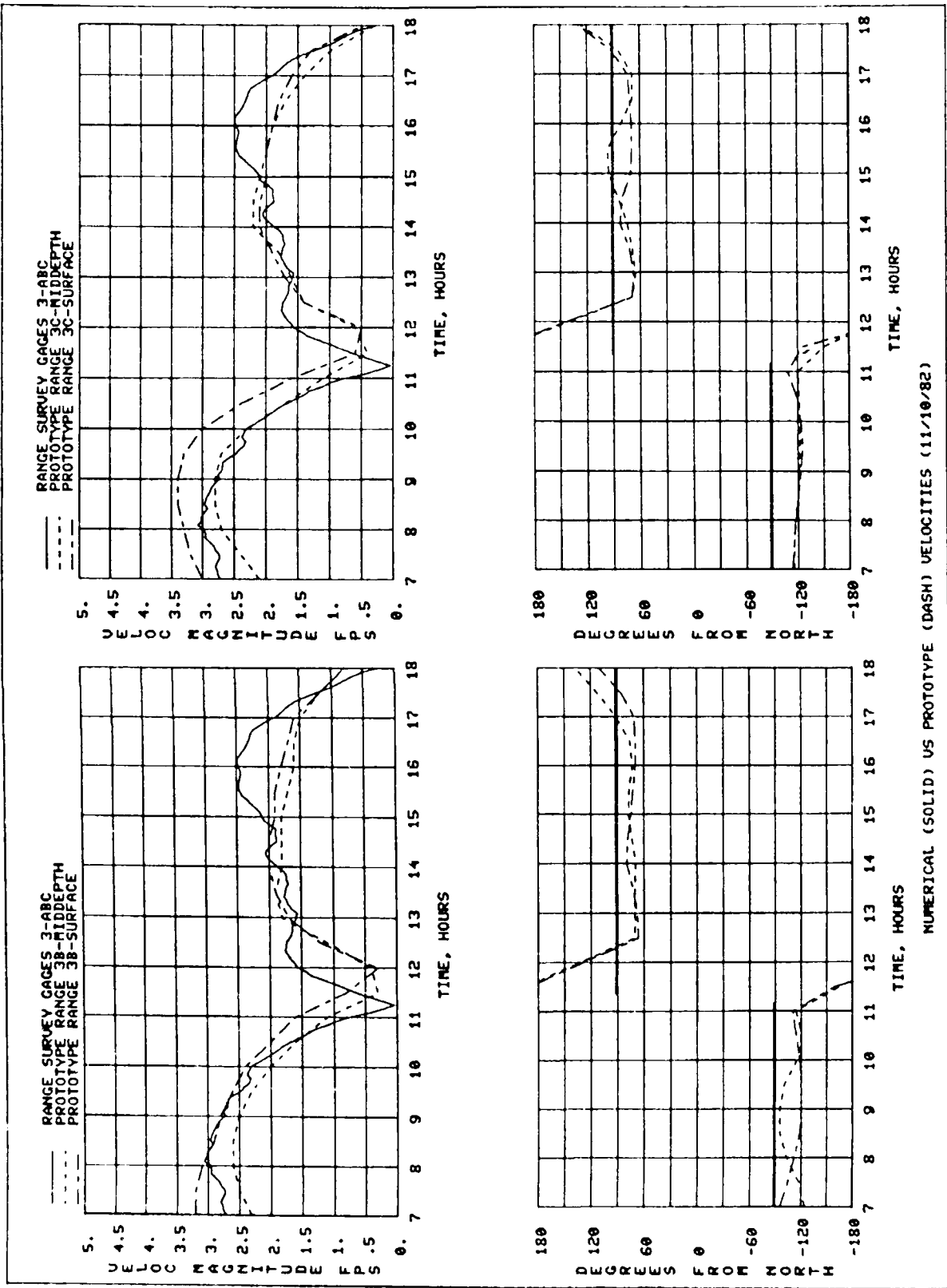


PLATE 11

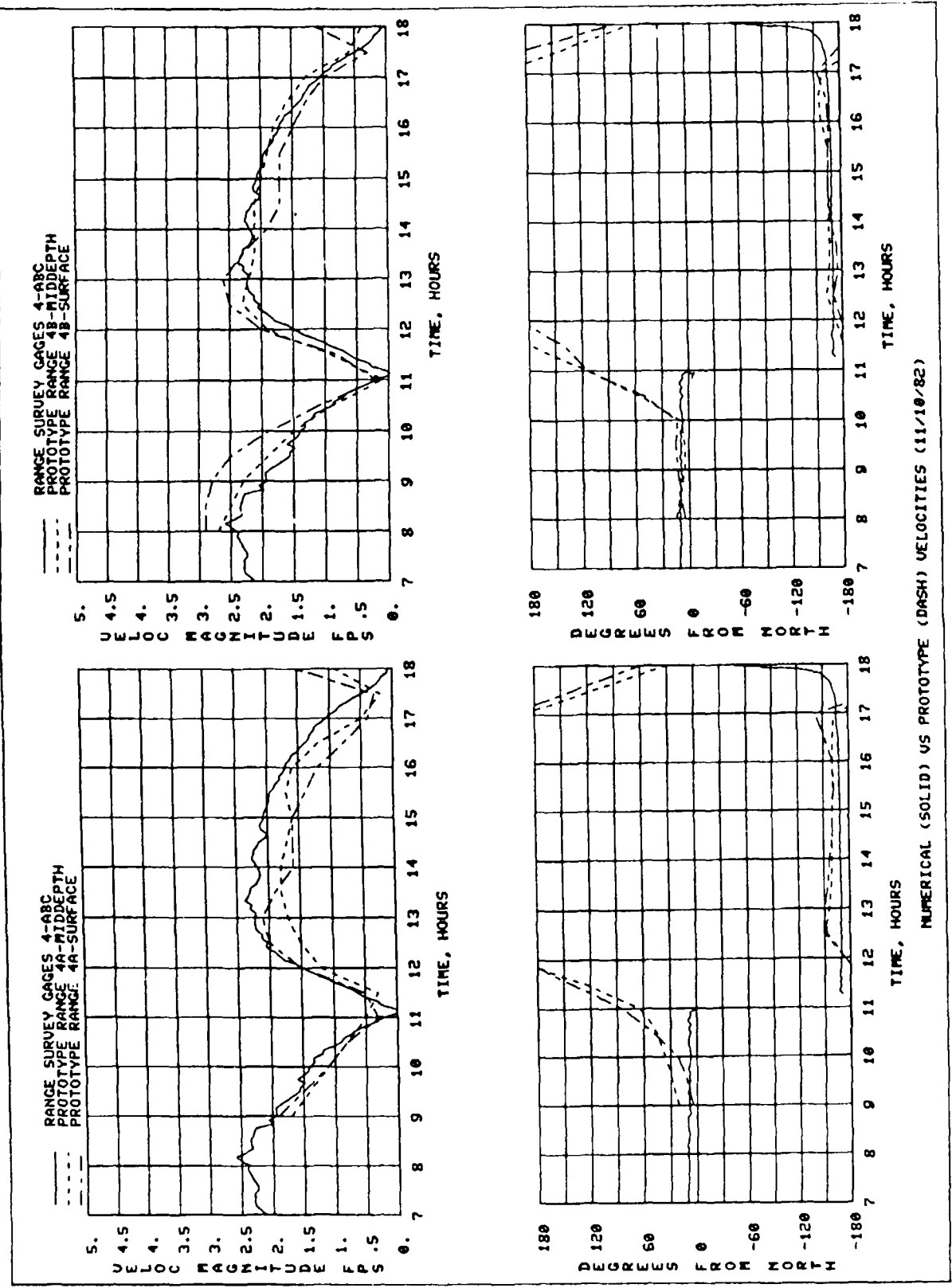
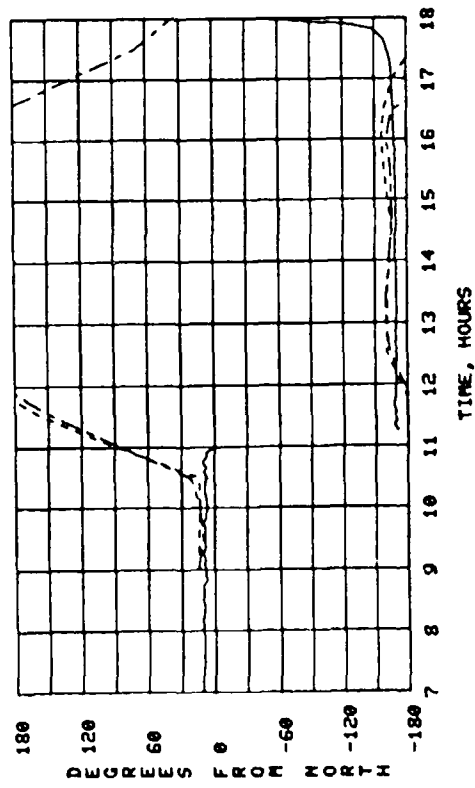
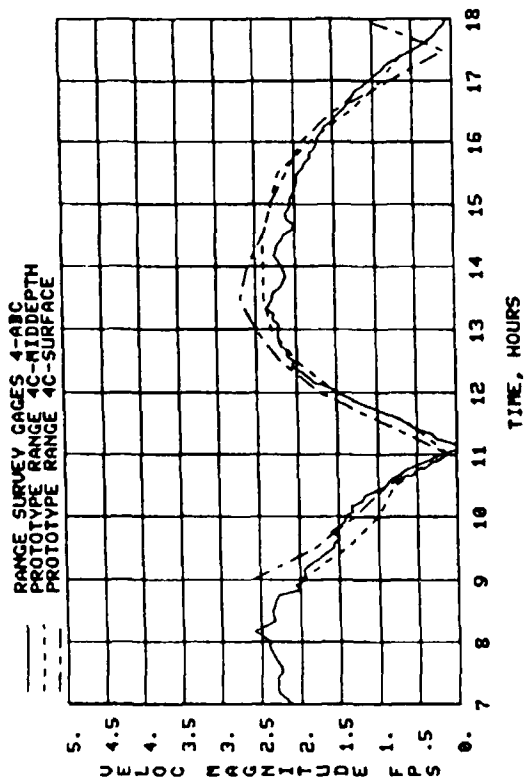
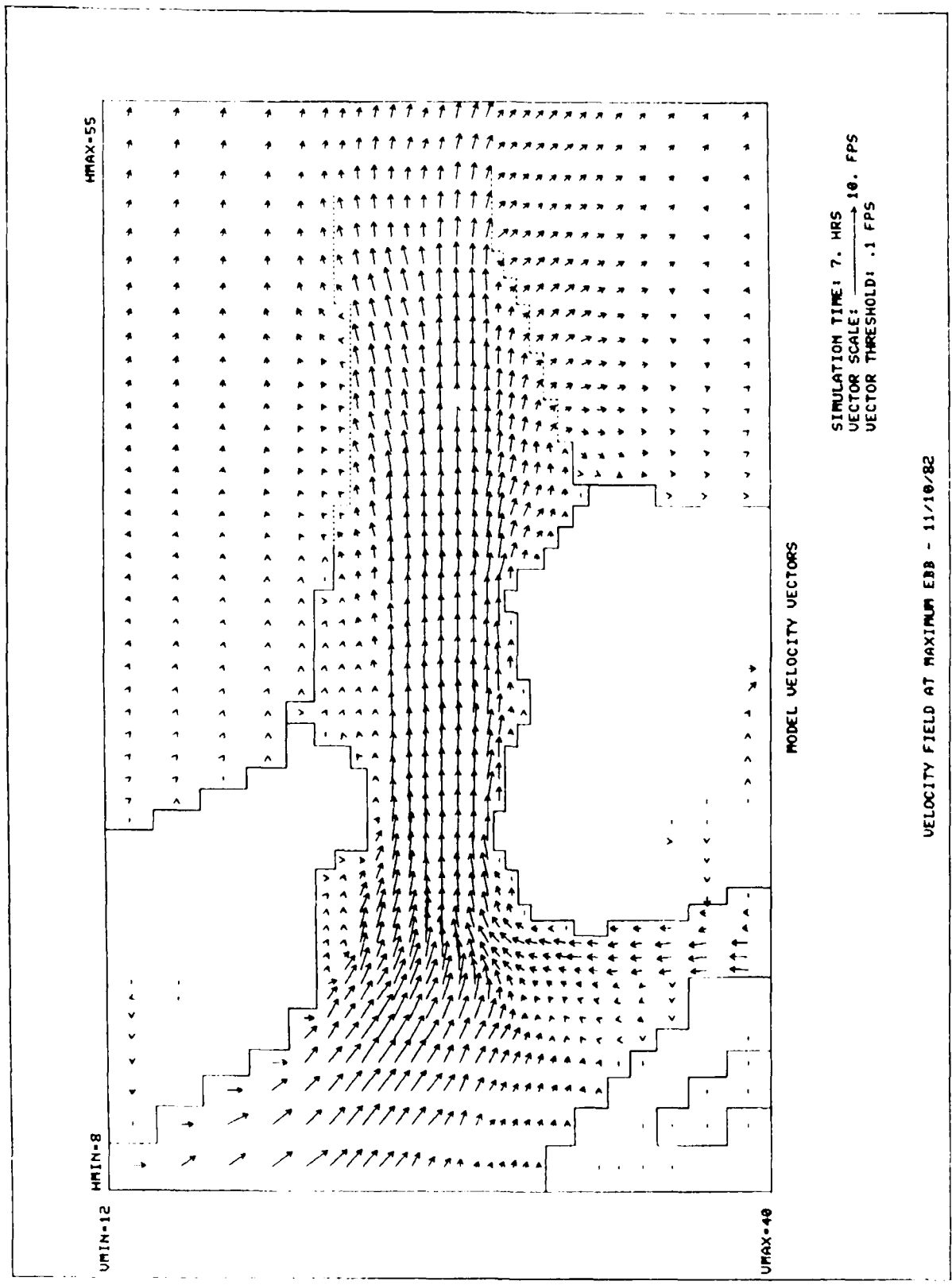
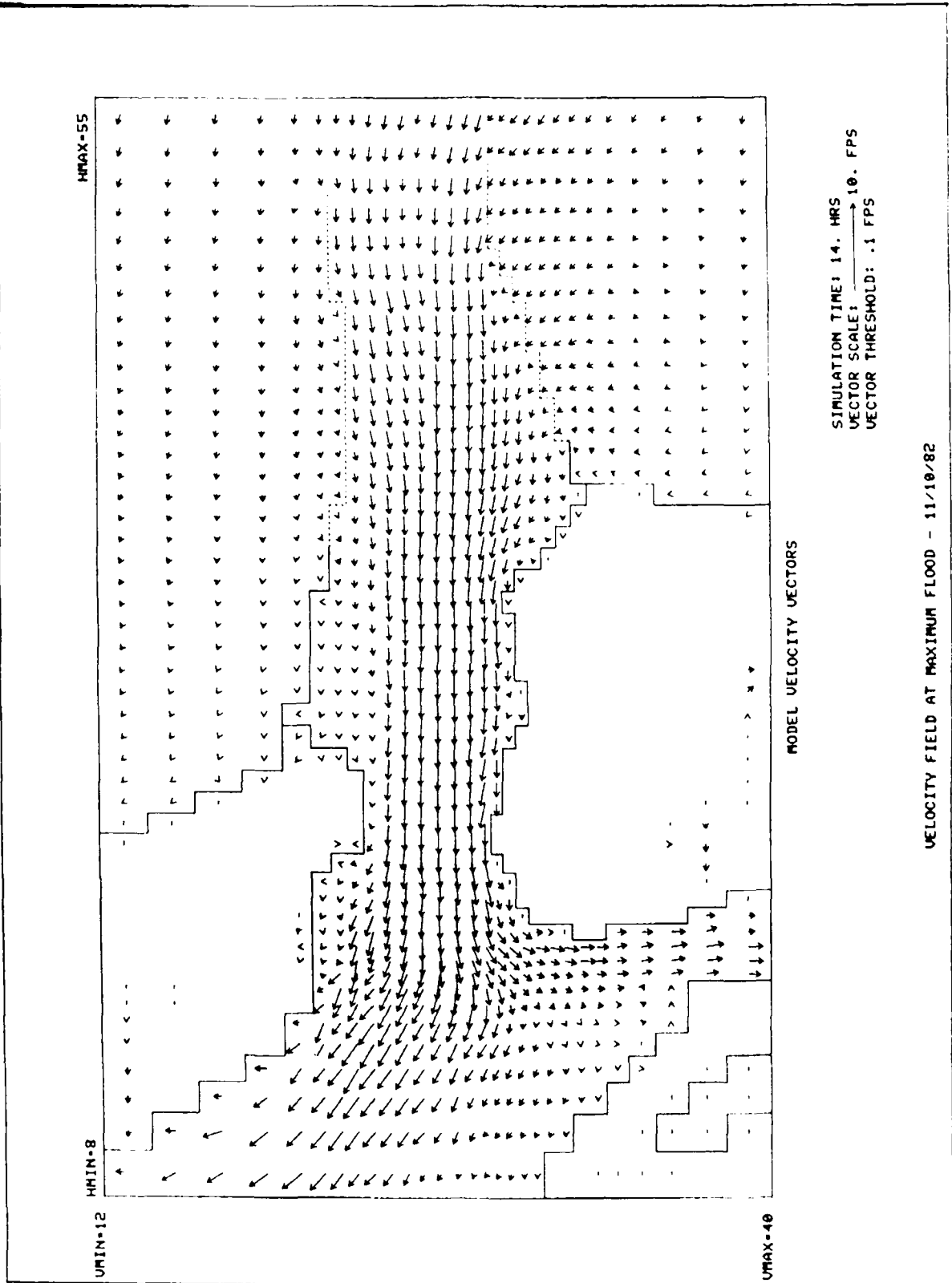


PLATE 12



NUMERICAL (SOLID) VS PROTOTYPE (DASH) VELOCITIES (11/10/82)





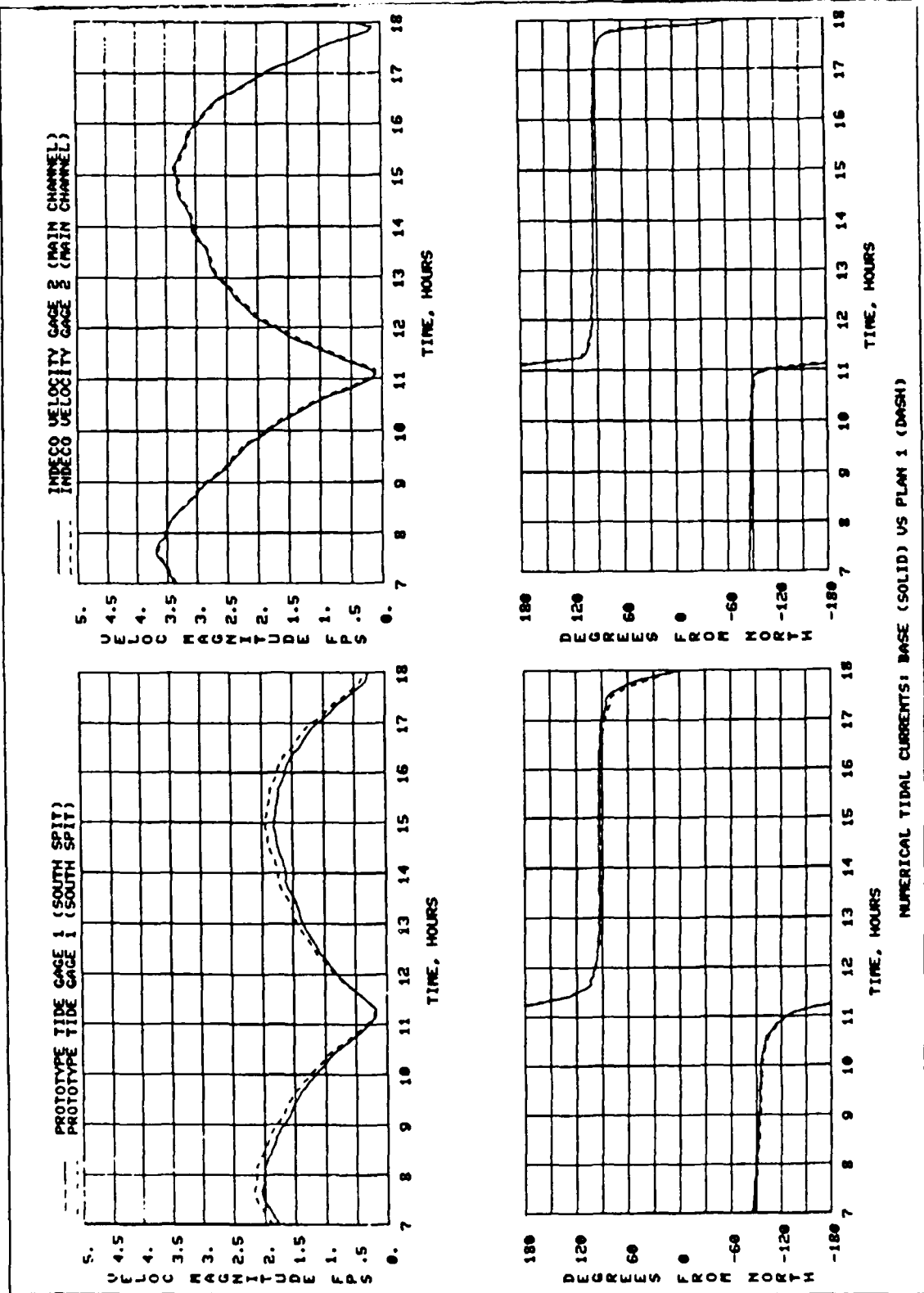
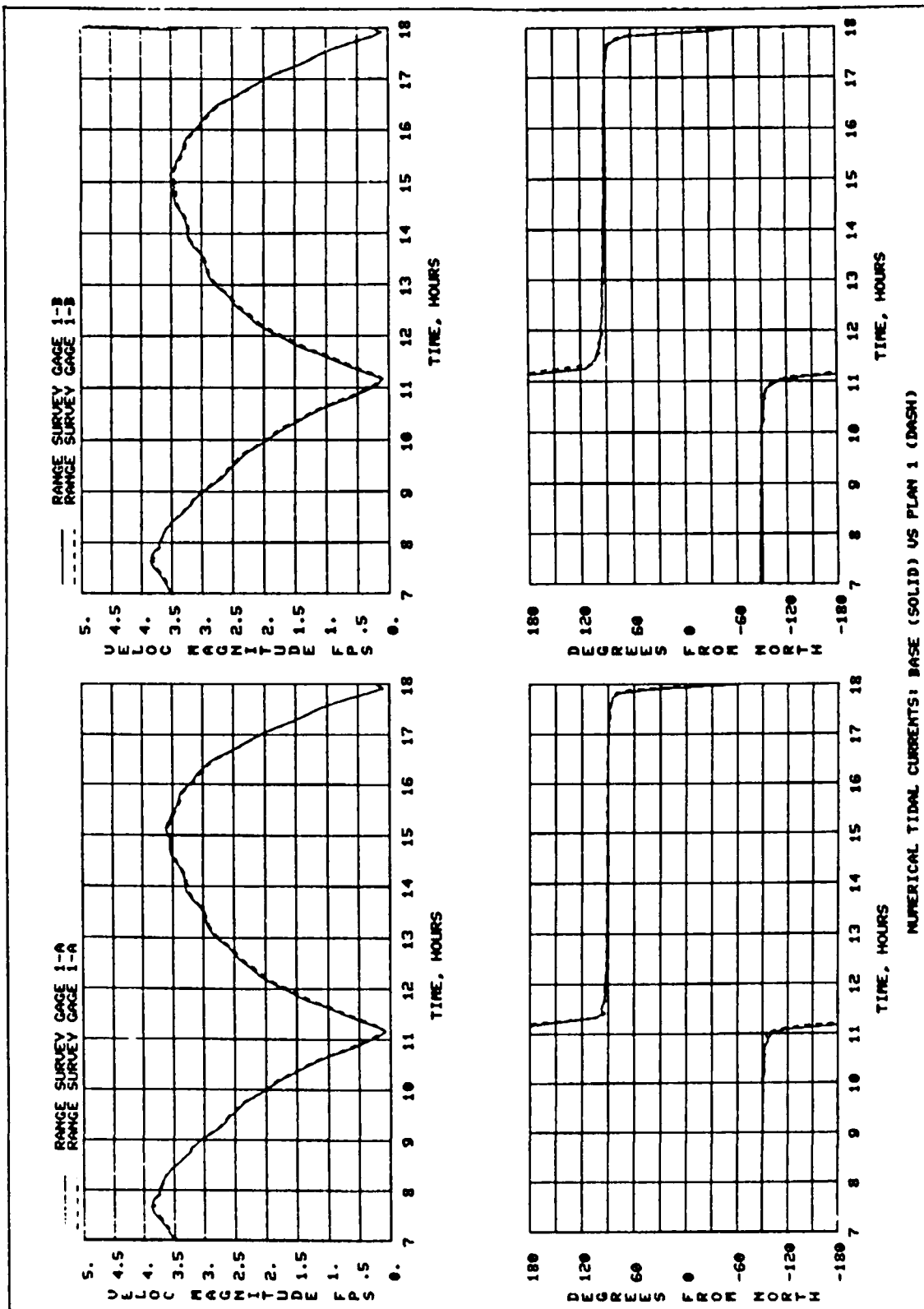
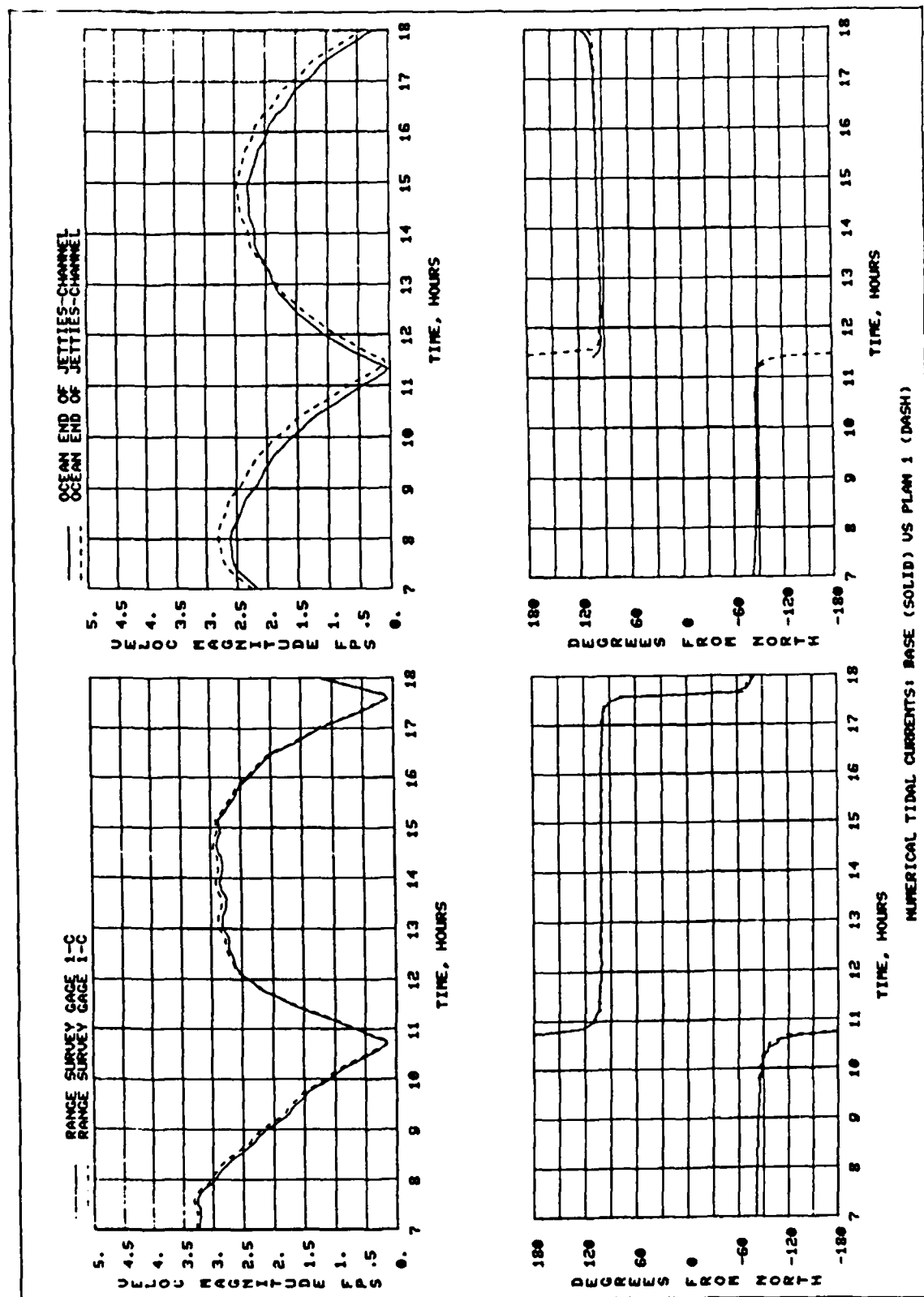
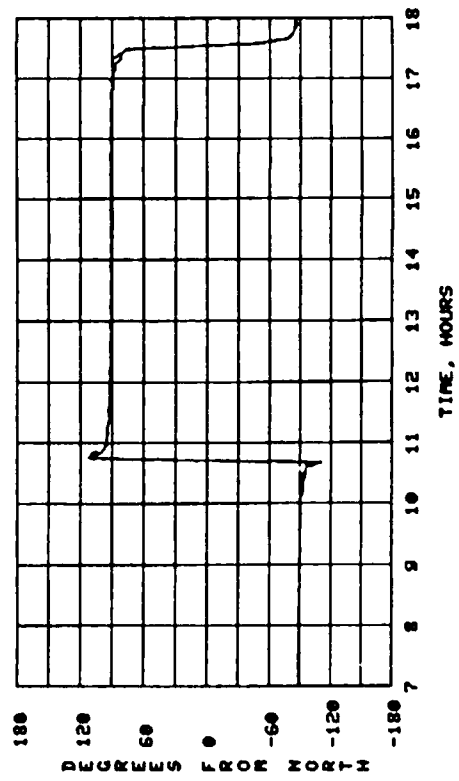
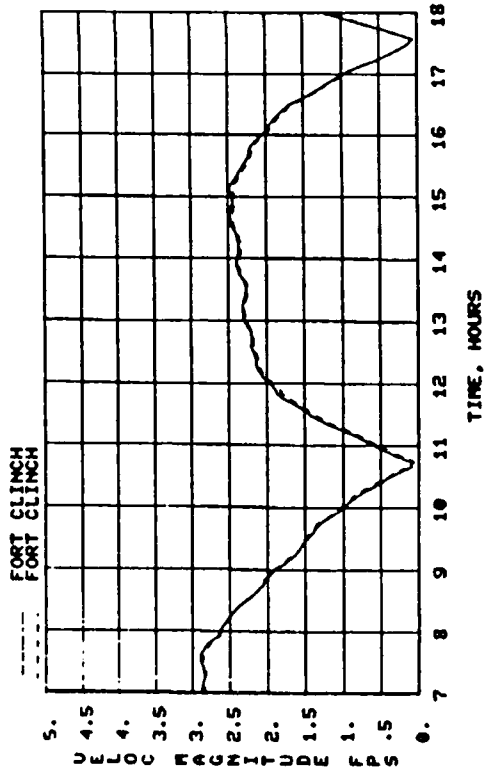


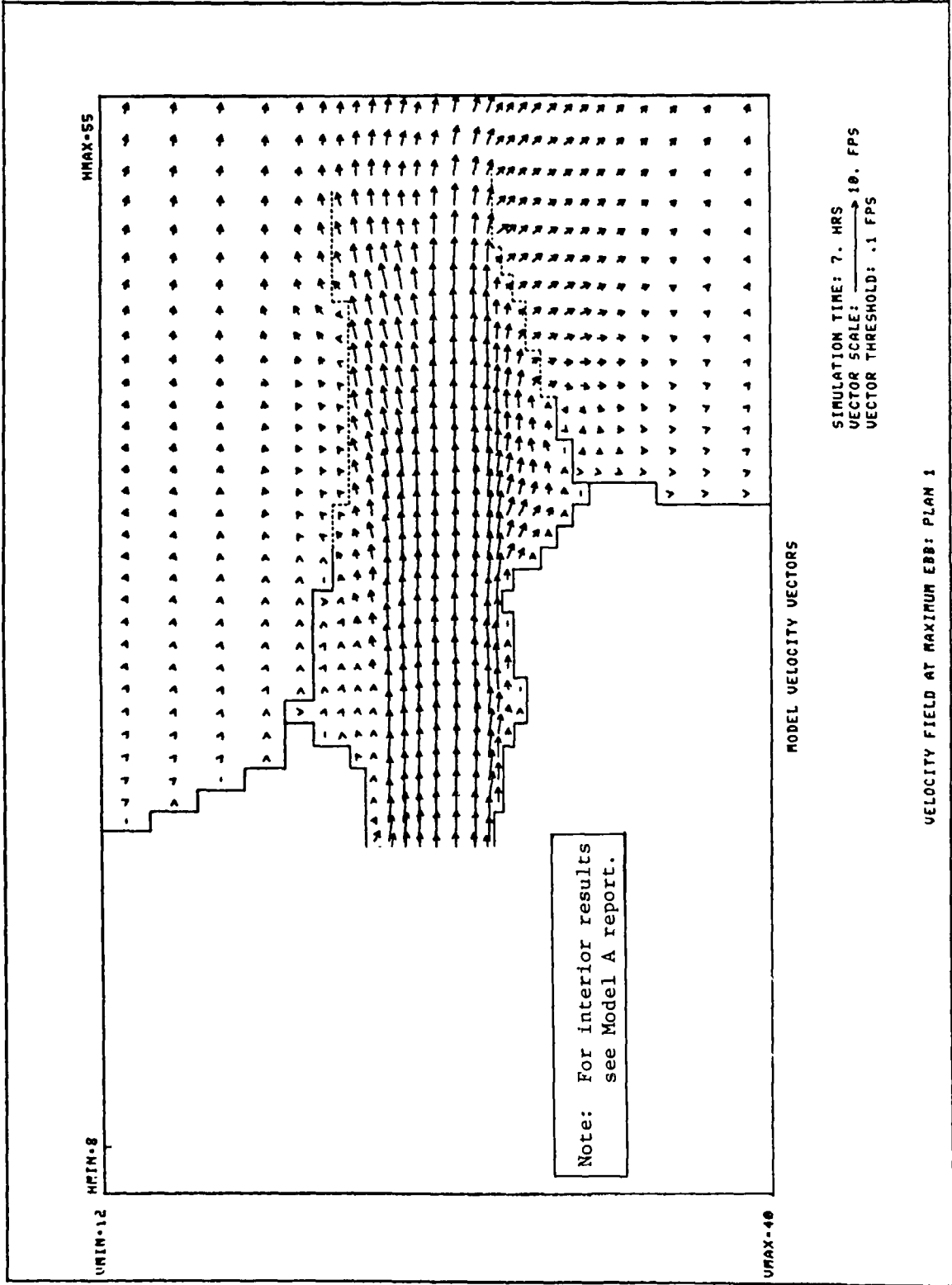
PLATE 16

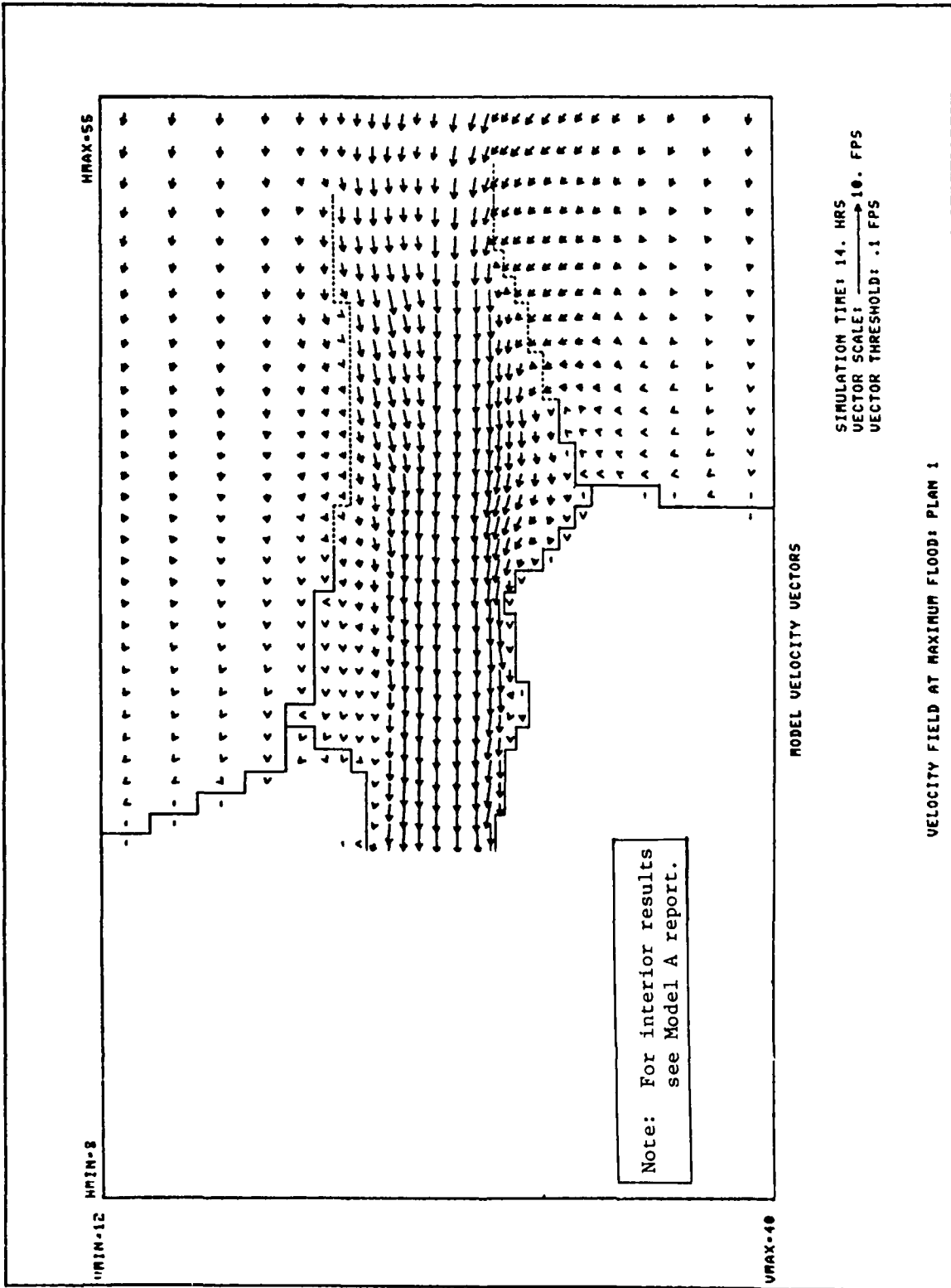






NUMERICAL TIDAL CURRENTS: BASE (SOLID) VS PLAN 1 (DASH)





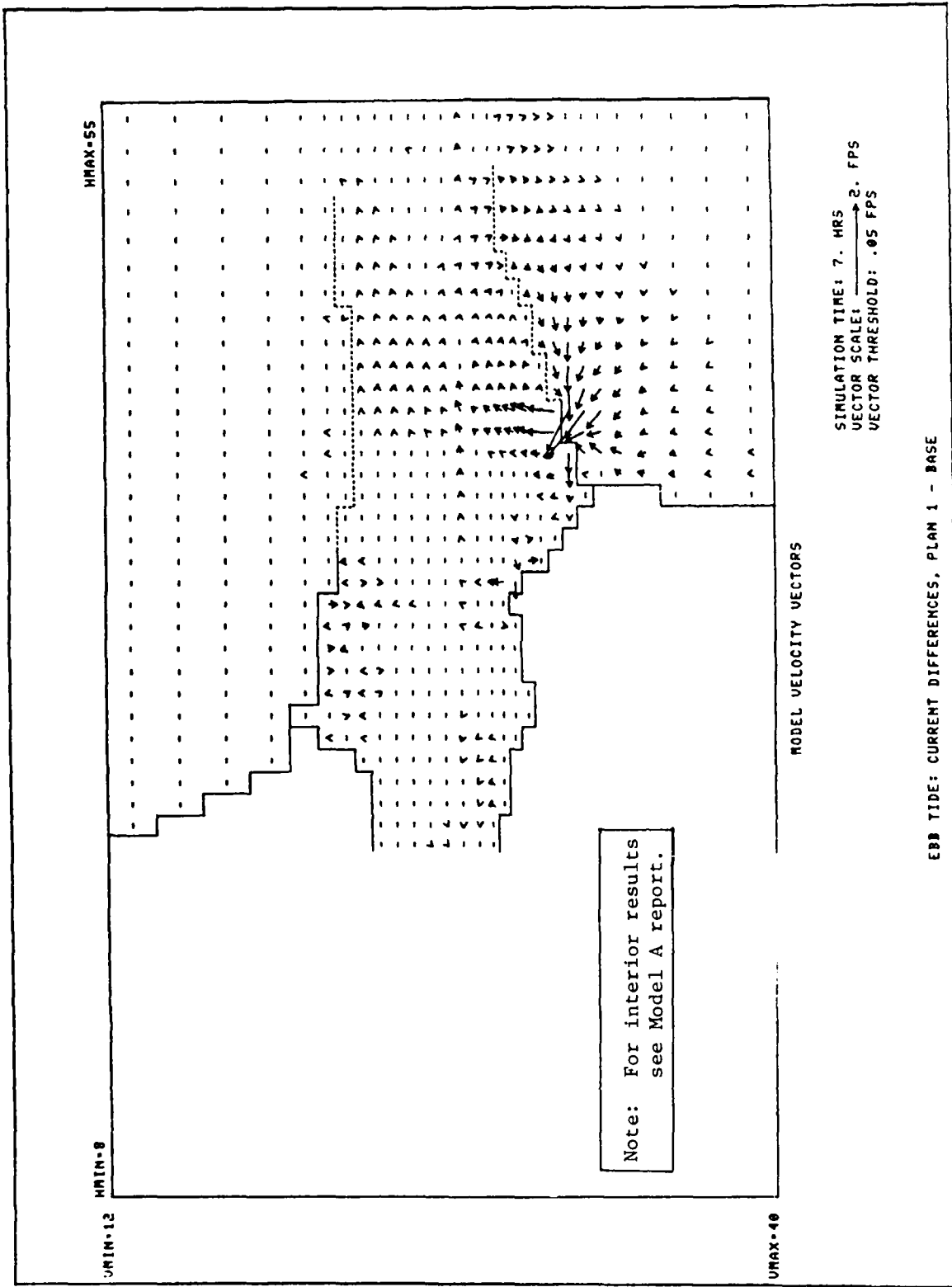
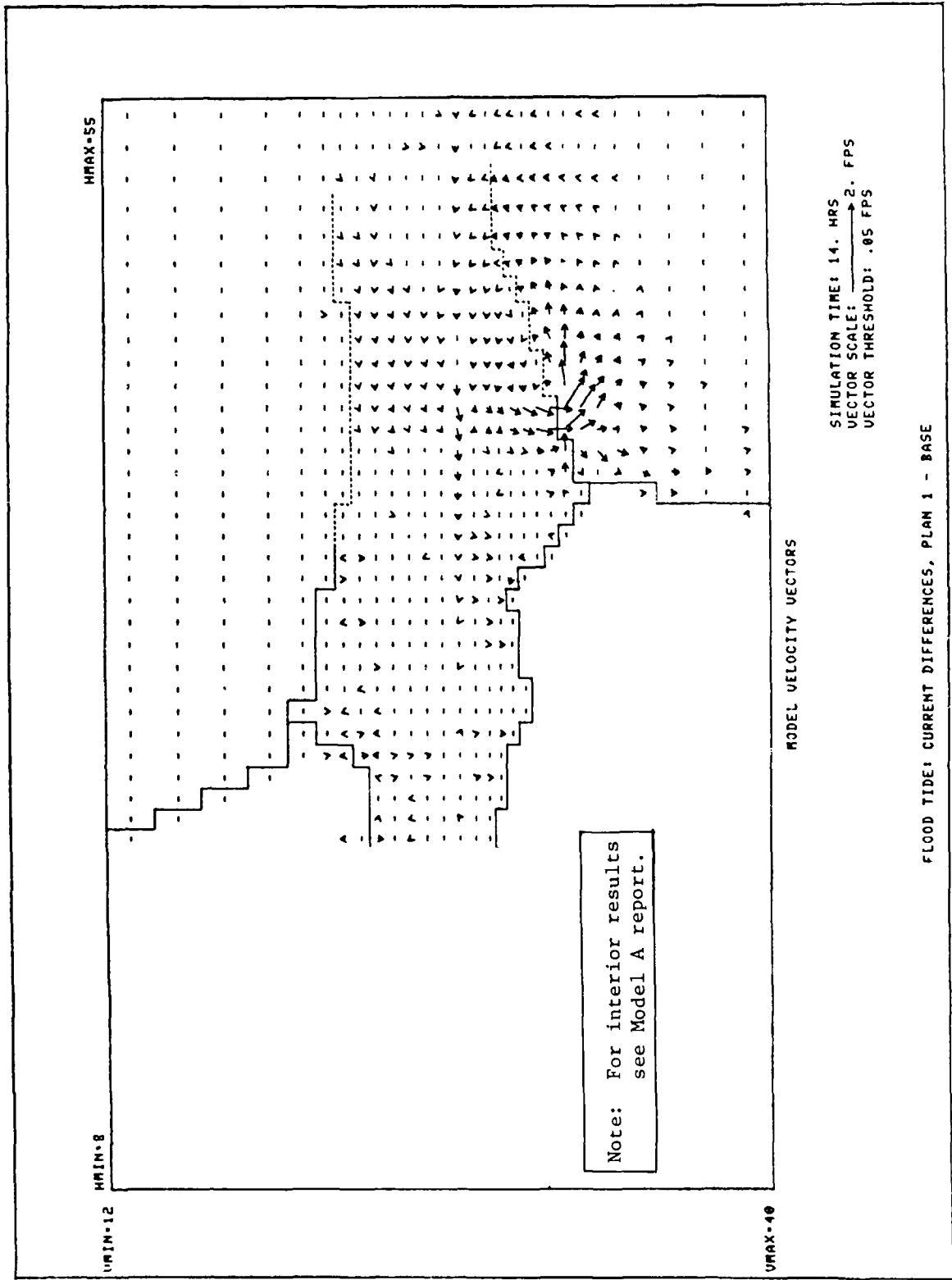


PLATE 22



APPENDIX A: NOTATION

a	Wave amplitude function
a'	Ratio of volume of solids to total volume of sediment = $1 - p$
$a_p, b_p, c_p$	Mapping constants for region p in x-direction
$a_q, b_q, c_q$	Mapping constants for region q in y-direction
$A_c$	Area of cell
c	Drag coefficient, wave celerity
C	Coefficient
$c_g$	Wave group velocity
$C_z$	Chezy coefficient
d	Local total water depth
D	Sediment diameter exceeded in size by 65 percent (by weight) of sediment sample, energy dissipation term
E	Wave energy density = $\rho g H^2 / 8$
f	Coriolis parameter, drag coefficient
$F_x, F_y$	Terms representing external forces
$f_w$	Wave friction factor with D as bed roughness
g	Acceleration due to gravity
h	Local still-water depth
H	Wave height
$H_o$	Wave height in deep water
$\vec{i}, \vec{j}$	Unit vectors in the x- and y-directions
$i_\ell$	Local immersed weight longshore transport rate
$I_\ell$	Total immersed weight longshore transport rate
IMAX	Number of water cells within the surf zone
k	Wave number
K	Empirical coefficient
$k_i$	Empirical coefficient
m	Bottom slope
M, N	Maximum values of cell indices for RCPWAVE
n	Ratio of group velocity to wave celerity = $c_g / c$ , Manning's roughness
p	Porosity of sediment
q	Local volumetric sediment transport rate due to currents

$q_\ell$	Local volumetric sediment transport rate
$q_x, q_y$	Local volumetric sediment transport rates in x- and y-directions
R	Rate of water volume change due to rainfall or evaporation
s	Arbitrary variable, mass density of sediment relative to that of fluid (specific gravity of sediment), wave phase function
$S_{xx}, S_{xy}, S_{yy}$	Radiation stresses
t	Time
T	Wave period
$u_o$	Wave orbital velocity at the bottom
$\langle  u_{orb}  \rangle$	Time average of the absolute value of the wave orbital velocity at bottom
u, v	Tidal velocity components
U, V	Velocity components due to wave-induced currents
$u_T$	Total velocity component = u + U
$v_*$	Shear (friction) velocity
$v_\ell$	Longshore velocity
$v_T$	Total velocity component = v + V
x, y	Coordinates in real space
$x_b$	Width of surf zone
Y	Dimensionless grain diameter
$\alpha_1, \alpha_2$	Coordinates in computational space
$\gamma$	Breaking index = H/h
$\Gamma$	Proportionality coefficient
$\delta_x, \delta_y$	Centered difference operators
$\Delta t$	Time-step
$\Delta x, \Delta y$	Cell dimensions in real space
$\Delta\alpha_1, \Delta\alpha_2$	Cell dimensions in computational space
$\epsilon$	Eddy viscosity for tidal model
$\epsilon_x, \epsilon_y$	Eddy viscosities in x- and y-directions
$\zeta$	Bed elevation
$\eta$	Tidal elevation above datum
$\bar{\eta}$	Mean free surface displacement (setup)
$\eta_a$	Hydrostatic water elevation due to atmospheric pressure differences
$\theta$	Angle of wave propagation
$\theta_o$	Wave direction in deep water

$\theta_c$	Contour angle
$\kappa$	Rate of energy dissipation coefficient
$\kappa_r$	Refraction coefficient
$\kappa_s$	Shoaling coefficient
$\mu_x, \mu_y$	Grid expansion coefficients
$\nu$	Kinematic viscosity of fluid
$\pi$	3.14159...
$\rho$	Mass density of sea water
$\rho_s$	Mass density of solids
$\sigma$	Wave angular frequency = $2\pi/T$
$\tau_o$	Bed shear stress
$\tau_{bx}, \tau_{by}$	Bottom friction stresses in x- and y-directions
$\tau_{xy}$	Lateral shear stress due to turbulent mixing
$\phi$	Complex velocity potential for wave

Superscripts

k-1	Previous time level
k	Present time level
k+1	Next time level
*	Intermediate time level

Subscripts

b	At breaking
s	Stable level of a variable
t	Partial derivative with respect to time

APPENDIX B: ABBREVIATIONS AND ACRONYMS

ADI	alternating-direction-implicit
CERC	Coastal Engineering Research Center
CESAJ	US Army Engineer District, Jacksonville
CEWES	US Army Engineer Waterways Experiment Station
CIP	Coastal and Inlet Processes
HL	Hydraulics Laboratory
mlw	mean low water
msl	mean sea level
mw1	mean water level
NGVD	National Geodetic Vertical Datum
NOS	National Ocean Service
OICC	Officer In Charge of Construction
RCPWAVE	Regional Coastal Processes Wave Propagation Model
SC	stabilizing-correction
sw1	still-water level
USGS	United States Geological Survey
WESWIS	WES Wave Information Study
WIFM	WES Implicit Flooding Model

END

DATE

FILMED

8-88

DTIC